UNIVERSITY OF OKLAHOMA

GRADUATE COLLEGE

EXAMINING THE SENSITIVITY OF TORNADIC SUPERCELL BEHAVIOR ON 27 APRIL 2011 TO THE BACKGROUND ENVIRONMENT USING OBSERVATION-DRIVEN SIMULATIONS AND MYRORSS AZIMUTHAL SHEAR ANALYSES

A THESIS

SUBMITTED TO THE GRADUATE FACULTY

in partial fulfillment of the requirements for the

Degree of

MASTER OF SCIENCE

By

ISABELLE JERNIGAN
Norman, Oklahoma
2025

Downloaded from SHAREOK. Persistent Handle URL: https://hdl.handle.net/11244/341586

EXAMINING THE SENSITIVITY OF TORNADIC SUPERCELL BEHAVIOR ON 27 APRIL 2011 TO THE BACKGROUND ENVIRONMENT USING OBSERVATION-DRIVEN SIMULATIONS AND MYRORSS AZIMUTHAL SHEAR ANALYSES

A THESIS APPROVED FOR THE
SCHOOL OF METEOROLOGY

BY THE COMMITTEE CONSISTING OF

Dr. Matthew Flournoy, Chair

Dr. Anthony Lyza

Dr. Stacey Hitchcock

Dr. David Bodine

© Copyright by ISABELLE JERNIGAN 2025
All Rights Reserved.

Acknowledgments

Many thanks to Casey Davenport for supplying the multiple base-state substitution code. This project was supported through NOAA/Office of Oceanic and Atmospheric Research under NOAA-University of Oklahoma Cooperative Agreement NA21OAR4320204, U.S. Department of Commerce. The statements, findings, conclusions, and recommendations are those of the authors and do not necessarily reflect the views of NOAA or the U.S. Department of Commerce.

Table of Contents

Acknowledgments **iv**

List Of Tables **vii**

List Of Figures **viii**

Abstract **xii**

1 Introduction **1**
1.1 Significance of 27 April 2011 Super Outbreak 1
1.2 Southeastern U.S. Tornado Climatology and Outbreaks 2
1.3 External Influences on Tornadic Supercells 3
1.3.1 Topography 3
1.3.2 Thermal Boundaries 4
1.3.3 Cell Mergers 5
1.4 Overview of 25-27 April 2011 5
1.4.1 Upper-level Features 7
1.4.2 Surface/Low-level Features 8

2 Data & Methods **17**
2.1 Storm Selection 17
2.2 Model Setup 18
2.2.1 Tendency Nudging 21
2.2.2 Base-State Substitution 22
2.3 Multi-Year Reanalysis of Remotely Sensed Storms (MYRORSS) Azimuthal Shear Analyses 25
2.4 Analysis: Early Evolution Focus 26

3 Simulation Outcomes **30**
3.1 CI timescales 30
3.2 Mesocyclone Evolution 32
3.2.1 Time-Height Evolution of Successful-Suite Mesocyclones 35
3.3 Simulated Environmental Characteristics 38

3.4 Storm Attributes and Environmental Predictors 44

4 Simulated vs. Observed Evolution **51**

5 Observed Evolution **59**
5.1 Supercell L 59
5.2 Supercells W and X 62
5.3 Supercell J 64
5.4 Supercells M and N 65

6 Discussion **68**
6.1 Regional Comparisons 74
6.1.1 Boundary Zone: M and N 74
6.1.2 Louisiana Delta: A and L 76
6.1.3 Warm Sector Zone 1: R and JU 77
6.1.4 Warm Sector Zone 2: W and X 77

7 Conclusions **80**

Reference List **85**

Appendix **92**
1 Appendix A 92
1.1 Approximation of Tornado Potential in Successful Suites 92
2 Appendix B 95

List Of Tables

2.1 Relevant information for each of the selected supercells. CI and storm end times are in UTC. 18

2.2 Important CM1 namelist parameters.
**The horizontal domain for JU ensemble members is either 148 km^2 or 192 km^2 in an effort to keep the storms in the domain and away from the boundaries.* 21

A.1 Time (minutes) of the full implementation of replace files for each supercell, adjusted by the CI time of each suite's 13th ensemble member. 108

List Of Figures

1.1 Progression of upper-level shortwave troughs and surface convection from 26-27 April 2011, from CK22b. 7
1.2 Relevant environmental parameters for the afternoon supercell outbreak, from K14. 12
1.3 Tracks of the 29 tornadic supercells from 27 April 2011, from L22. . . . 14

2.1 Initial base-state soundings for all 8 selected supercells. Ranges of relevant environmental parameters are included. 20
2.2 Time series of the heating tendencies for each ensemble members. These heating tendencies are identical for all eight ensemble suites. 22
2.3 Base-state substitution framework for supercell M. 24
2.4 Reflectivity at 1 km AGL for Supercell M, ensemble member 4, at 290 min, 310 min, and 330 min into the simulation. 28

3.1 Bar plot showing the median time for various thresholds to be met. Bars are color-coded by storm. The thresholds are CI (first 40 dBZ-echo), a 10-ms^{-1} updraft at 3 km AGL, a 20-ms^{-1} updraft at 3 km AGL, and 750 m^2 s^{-2} of 2–5-km AGL updraft helicity (UH). 0–3-km AGL UH is not included as it is the same as 2–5-km AGL UH. 31
3.2 Time series for 25th percentile (green line), 75th percentile (purple line), and IQR (gray shading) for maximum 2–5-km-AGL UH after CI for each storm's ensemble suite. Each storm has a panel, and the panels are arranged by latitude of observed CI, so the northern-most initiating supercell is at the top and the southern-most at the bottom. The orange dashed line represents the number of ensemble members that have not experienced an unphysical reflectivity band merging with the main supercell at each time. 34
3.3 Simulated reflectivity fields of at 1 km AGL, 250 min into the simulations, for all 25 CI regimes of storm A. 35
3.4 Time-height plots of 25th percentile, 75th percentile, median, and maximum UH. UH is calculated in 500-m layers, as that is the vertical resolution of our simulations for the ensemble suites of supercells M, N, and W. Only the early evolution period (first 4 h after CI) is shown for M and N. The entire life span of storm W is shown because it lost supercell characteristics less than 4 h after CI. 37
3.5 SFCOA soundings and hodographs of supercell R's 3rd (olive) and 4th (blue) base-state environments. Solid lines indicate temperature profiles; dashed, moisture profiles. 38

3.6 Timeseries of select thermodynamic (here, MLCAPE) and kinematic (here, 0-6 km Bulk Shear) parameters in our simulated (solid line) and BSS (dashed line) environments. The simulated timeseries depict ensemble-median values for each storm suite. 40
3.7 Vertical profiles of the difference in relative humidity for each supercell's initial (blue) and second (purple) base-state environments. The storms are grouped by region, and the relative humidity of the less-successfully simulated storm outcome is subtracted from the more successful storm. 41
3.8 Moisture profiles for each storm's initial base-state. 42
3.9 Vertical profiles of relative humidity (green) and shear segments (blue) 100 min into the control simulations (no storms initiated) for each supercell. Columns are arranged by the region of the observed storms, and the top row is generally the more successful storm in each region. . . . 43
3.10 Scatter plots of 2–5-km AGL UH vs. 0–1-km AGL SRH during the early evolution period. Each panel is a different CI regime, with increasing magnitude of tendency nudging from left to right and increasing duration from top to bottom. Each dot, color-coded by storm, represents a 20-min average of the simulated quantities that reduce the effects of persistence in consecutive time steps. The black lines denotes the line of best fit across all the storms in each CI regime. Association correlation coefficients are displayed in the same panels. The asterisks denote statistical significance (* $p < .05$, ** $p < .01$). 45
3.11 As in Figure 3.10, except for 2-5 km AGL UH and MLCAPE. 47
3.12 As in Figure 3.10, except lines of best fit are shown for each individual storm. Additionally, statistical significance ($p < .05$) is displayed with thicker lines of best fit and corresponding correlation coefficients at the top of each panel. 49
3.13 As in Figure 3.12, except for 2-5 km AGL UH and MLCAPE. 50

4.1 Time series of 25th percentile (green line), 75th percentile (purple line), and IQR (gray shading) for maximum vertical vorticity in the 10-m to 3-km AGL layer after CI for each storm's ensemble suite. The black dashed line is maximum observed low-level AzShear after CI. Each storm has a panel, and the panels are arranged by latitude of observed CI, so the northern-most initiating supercell is at the top and the southern-most at the bottom. The orange dashed line represents the number of ensemble members that have not experienced an unphysical reflectivity band merging with the main supercell. 53
4.2 As in Figure 4.1, but for maximum vertical vorticity in the 3-km to 6-km AGL layer and mid-level AzShear. 54
4.3 Differences between ensemble-median simulated vertical vorticity and observed AzShear values in the corresponding layers. Low-level (0–3-km AGL) ζ and AzShear are blue; mid-level (3–6-km AGL), olive. . . . 55

4.4 Observed maximum AzShear as a function of simulated maximum vertical vorticity in the low- (left) and mid-levels (right) for the ensemble suite of Supercell M. Large dots indicate ensemble median; small dots, ensemble minimum and maximum, connected by a horizontal line. The 25th and 75th percentiles are denoted by short vertical ticks. 56
4.5 As in Figure 4.4, but for supercell N. 57
4.6 Temporal derivatives of observed AzShear plotted as a function of the temporal derivatives of simulated, ensemble-median vertical vorticity in the corresponding layers for each storm. Lines of best fit are also included, as well as correlation coefficients between the parameters and indications of statistical significance ($p < .05$). The quantities were smoothed to reduce noise, and every other data point is used to reduce persistence biases. 58

5.1 Nexrad level 2 reflectivity field at the lowest tilt at 1915, 2005, 2028, and 2145 UTC on 27 April 2011. 60
5.2 Meteogram from the CYSM6 surface station in Copiah County, MS. The top panel contains air temperature (red, °C), dew point temperature (cyan, °C), and relative humidity (%, green dashed line). The bottom panel displays wind speed (m s^{-1}, dark blue), peak wind speed (m s^{-1}, light blue), and wind direction (white and black dots). The approximate time that the outflow boundary passed over the station (2030 UTC) is denoted by the vertical black line in both panels. 61
5.3 Nexrad level 2 reflectivity field at the lowest tilt at 2355, 0054, 0154, and 0330 UTC on 27-28 April 2011. 63
5.4 Nexrad level 2 reflectivity field at the lowest tilt at 1823, 1947, 2005, and 2046 UTC on 27 April 2011. 65
5.5 Nexrad level 2 reflectivity field at the lowest tilt at 1919, 1924, 2001, 2033, 2047, and 2106 UTC on 27 April 2011. 67

6.1 Velocity couplet in the pre-convective showers of supercell M, as seen at 1915 UTC by KDGX at the lowest tilt. 71

A.1 As in Figure 3.4, but for updraft speed. The black contour denotes vertical velocities of 20 m s^{-1}. 93
A.2 As in Figure 3.4, but for vertical vorticity. The black contours denote values of 0.01 s^{-1}, 0.015 s^{-1}, and 0.02 s^{-1}, where thickness increases with magnitude. 94
A.3 Base-state substitution framework for supercell A. 95
A.4 Base-state substitution framework for supercell R. 95
A.5 Base-state substitution framework for supercell L. 95
A.6 Base-state substitution framework for supercell JU. 96
A.7 Base-state substitution framework for supercell N. 96
A.8 Base-state substitution framework for supercell W. 96

A.9 Base-state substitution framework for supercell X. 97
A.10 Time series for 25th percentile (green line), 75th percentile (purple line), and IQR (gray shading) for maximum updraft speed at 3 km AGL after CI for each storm's ensemble suite. Each storm has a panel, and the panels are arranged by latitude of observed CI, so the northern-most initiating supercell is at the top and the southern-most at the bottom. The orange dashed line represents the number of ensemble members that have not experienced an unphysical reflectivity band merging with the main supercell. 98
A.11 As in Figure A.10, but for updraft speed at 1 km AGL. 99
A.12 As in Figure A.10, but for updraft speed at 6 km AGL. 100
A.13 As in Figure A.10, except for maximum 10-m to 3-km AGL updraft helicity. 101
A.14 As in Figure 3.10, except for 0–3-km AGL UH and 0–1-km AGL SRH. 102
A.15 As in Figure 3.10, except for 0–3-km AGL UH and MLCAPE. 103
A.16 As in Figure 3.10, except for 2–5-km AGL UH and 0–6-km bulk shear. 104
A.17 As in Figure 3.10, except for 0–3-km AGL UH and 0–6-km bulk shear. 105
A.18 As in Figure 3.10, except for 2–5-km AGL UH and STP. 106
A.19 As in Figure 3.10, except for 0–3-km AGL UH and STP. 107

Abstract

The prolific 27–28 April 2011 tornado outbreak produced multiple rounds of tornadic supercells in four spatiotemporal regions. All of these regions exhibited extremely favorable environments, with small differences in thermodynamic and kinematic profiles and varying proximities to boundaries. This study uses multiple radar-based and environmental observations to inform high-resolution, 25-member numerical ensembles of five select supercells that formed in these regions. Storm Prediction Center surface objective analysis (SFCOA) profiles, RUC profiles blended with surface observations, are used in a base-state substitution technique to continuously nudge the simulated environments towards observations. A more gradual tendency nudging convection initiation technique is used to attempt to capture the mesocyclone development noted in MRMS-based azimuthal shear (AzShear) analyses. Individual ensemble members vary in the magnitude and duration of tendency nudging. This study provides insight into the effects of small changes in tendency nudging on simulated storms across different, albeit all extreme, environments. The resulting simulations are compared to AzShear analyses from the MYRORSS dataset and observed reflectivity fields to judge the performance of our combined tendency nudging and base-state substitution approach, evaluate how much of the observed storm evolutions may have been dependent on the background mesoscale environment, and assess the resulting predictability of the observed storm evolutions. The ensemble suites exhibit a diversity in storm outcomes. The successful simulations mature comparatively quickly, and represent observed storms that initiated at higher latitudes where low-level and deep-layer shear were maximized. The degree to which they emulate their observed counterparts varies, with the most realistic simulated supercells corresponding to the northernmost-initiating storms in the highest-shear environments. The unsuccessful suites, in which ensembles could not sustain organized convection after the cessation of the heating tendencies, have less humid mid- and upper-tropospheres. Several external, mesoscale

features absent from the simulations are identified as playing a critical role in maintaining observed storms in environments that failed to sustain organized, simulated convection. These findings highlight a reliance of tornadic supercells on inhomogeneous influences (terrain, cell interactions, etc) during the 27 April 2011 super outbreak, and the limited predictability of similar high-impact events in the future.

Chapter 1

Introduction

1.1 Significance of 27 April 2011 Super Outbreak

The 27 April 2011 tornado super outbreak stands as one of the most devastating outbreaks on record in the United States (U.S.). In less than 24 hours, nearly 200 tornadoes swept across the southeastern U.S., resulting in 318 fatalities, thousands of injuries, and billions of dollars in damages (NOAA 2011; Simmons et al. 2012; Knupp et al. 2014, hereafter K14). The supercell component of this outbreak produced the most violent and longest-tracking tornadoes of the day (K14; Chasteen and Koch 2022a,b, hereafter CK22a,b; Lyza et al. 2022, hereafter L22). Around 90% of the supercells produced at least one tornado (K14). Of these tornadic supercells, 79.3% were responsible for at least one significant (EF2+) tornado and 55.2% produced a deadly tornado (L22). In total, the discrete convective episode accounted for over 100 tornadoes (L22), including 14 EF3, 11 EF4, and four EF5 tornadoes (K14). When considering both pathlength and intensity, many disaster metrics rank this outbreak alongside the 3–4 April 1974 Super Outbreak (K14). Despite the historic and catastrophic impacts of this event, supercell morphology and behavior remain relatively underexplored by current literature.

1.2 Southeastern U.S. Tornado Climatology and Outbreaks

Trapp (2014) noted that multi-day severe weather episodes are most common between April and July, and significant tornadoes and outbreaks are more likely to occur in the latter half of these periods due to the continued replenishment of the environment and an accumulation of CAPE. This was the case for the 27 April 2011 tornado super outbreak, which occurred at the end of several consecutive days of severe weather from 25-27 April 2011. In the days preceding this outbreak, a persistent longwave trough remained nearly stationary over the central United States. When examining the tornado outbreak sequence of May 2003, Hamill et al. (2005) noted that quasi-stationary weather patterns allow for the prolonged flow of warm, moist air from the Gulf northward and stronger west-southwest winds aloft, conducive for tornadoes.

Unlike the Central Plains, tornado environments in the southeastern U.S. are typically characterized by low MLCAPE (<1000 J kg^{-1}) and strong deep layer shear (Schneider et al. 2006; Grams et al. 2012; Anderson-Frey et al. 2019). Significant tornadoes (EF2+) in high-shear, low-CAPE (HSLC) environments are not only most common in the Southeast, but also make up the majority of significant tornadoes in the region (Guyer and Dean 2010; Dean and Schneider 2012; Sherburn and Parker 2014). Based on daily tornado probabilities, the Southeast faces its greatest tornado risk in April (Brooks et al. 2003). In an objective analysis of regional significant tornado risk, Coleman and Dixon (2014) found that much of the Southeast, specifically eastern Arkansas, central Mississippi, and northern Alabama, are most susceptible to these hazards, even after removing 27 April 2011 tornadoes from the analysis. This susceptibility is in a region where people are more vulnerable to tornadoes, given their nocturnal timing, low visibility due to forests, and a number of societal risk factors

including a high population percentage residing in mobile homes (Ashley 2007; Ashley et al. 2008; Coleman and Dixon 2014; Krocak and Brooks 2018; Anderson-Frey et al. 2019). As such, it is no surprise that double the percentage of tornadoes in the Southeast are deadly compared to the rest of the country (Anderson-Frey et al. 2019).

The timing of this outbreak, in terms of time or year and position within a multi-day severe threat, fit within our current tornado climatology. However, the magnitude of instability in the environment is highly anomalous for tornado days in the Southeast U.S. Another atypical feature of this event was the location of the dryline. Drylines rarely persist into the Mississippi River Valley region (Hoch and Markowski 2005). However, some of the most well-known events have featured a dryline in this region. This includes the Tri-State tornado and the 3–4 April 1974 Super Outbreak, as well as the outbreak discussed herein (Corfidi et al. 2010; Maddox et al. 2013; Duell and Van Den Broeke 2016).

1.3 External Influences on Tornadic Supercells

1.3.1 Topography

The ability of storms to initiate and the hazards associated with those storms can be sensitive to the topography of the land underneath it. Even small variations such as shifting model terrain northward or westward by less than 1° can alter CAPE, moisture, local convergence, and low-level SRH present environment in which convection initiates (Zhang et al. 2015). Compared to simulations with flat-terrain, orographic impacts on environmental thermodynamic characteristics also alter simulated storm intensity (Markowski and Dotzek 2011). Additionally, regions of complex terrain will have greater friction, which can promote backing and greater ageostrophic flow in the low levels, altering hodograph curvature (Banacos and Bluestein 2004; CK22b).

Several studies have investigated orographic effects on the apparent maximum in tornado activity in northeastern Alabama, many of which were motivated by the 27 April 2011 Super Outbreak. Gaffin (2012) found that the strong southeasterly low-level flow was accelerated and tornadogenesis was favored at the openings of southwest–northeast-oriented valleys in the southern Appalachian Mountains on 27 April, where terrain-induced kinematic perturbations contributed to greater vorticity, convergence, and 0–1-km AGL SRH (Lyza and Knupp 2018; Katona and Markowski 2021). Lower LCL heights over higher terrain in the region further create an environment conducive for tornadogenesis (Lyza and Knupp 2018; Lyza et al. 2020).

1.3.2 Thermal Boundaries

As will be discussed in a later section, the northern portion of the warm sector with residual outflow boundaries from the preceding QLCSs contained enhanced SRH, creating a locally more favorable environment for strong low-level mesocyclones and tornadoes. For individual supercells, the apparent link between thermal boundaries and tornado production has been observed on many tornado days, including this outbreak. The VORTEX field campaign in 1995 observed many tornadogenesis events around thermal boundaries. They hypothesized that the thermal boundaries were not required for tornadogenesis, but supplemented ambient horizontal vorticity (Markowski et al. 1998; Rasmussen et al. 2000). Another theory from Maddox et al. (1980) is that mesoscale intensification of moisture convergence and cyclonic vorticity in narrow mixing zone along the boundary can support intense tornadoes when the larger environment is less conducive.

1.3.3 Cell Mergers

Much literature on the topic of cell mergers seeks to find the best definition of a "merger" and the dynamic processes behind such phenomena. This brief section will focus on the result of a merger involving a supercell, which depends on the maturity of the merging cells and the relative location of the two updrafts (Hastings and Richardson 2016). Forward flank mergers outcomes can range from dissipation to stronger classic or high-precipitation supercells depending on the distance between the updrafts. Outflow from the secondary cell can muddle the inflow environment, potentially disrupting tornado production (Rogers and Weiss 2008; Rogers 2012). Meanwhile, rear-flank mergers almost always result in a stronger mesocyclone, at least in some numerical experiments (Hastings and Richardson 2016). The storm will have a stronger cold pool on its rear flank than before the merger, and there will be increased, baroclinically-produced vorticity following the merger (Hastings et al. 2014).

Cell mergers were prolific during the afternoon supercell outbreak on 27 April, with Lyza and Flournoy (2023) noting 300 such events. In this outbreak, mergers tended to alter the supercell's pre-merger behavior, whether it was tornadic or non-tornadic. Additionally, less frequent mergers prior to initial tornadogenesis resulted in a slower time to tornadogenesis, but were also a feature for supercells that produced long-tracked tornadoes.

1.4 Overview of 25-27 April 2011

Trapp (2014) noted that multi-day severe weather episodes are most common between April and July, with significant tornadoes and outbreaks more likely to occur in the latter half of these periods due to the continued environmental replenishment and an accumulation of convective available potential energy (CAPE). This was the case for

the 27 April 2011 tornado Super Outbreak, which concluded several days of severe weather from 25-27 April 2011.

In the days preceding this outbreak, a persistent longwave trough remained nearly stationary over the central United States (U.S.; CK22a,b). When examining the tornado outbreak of May 2003, Hamill et al. (2005) noted that quasi-stationary weather patterns support prolonged transport of warm, moist air from the Gulf and stronger west-southwest winds aloft, conditions favorable for tornadoes. Within this persistent trough at the end of April 2011, three prominent shortwave troughs and multiple jet streaks influenced surface-level features that contributed to the devastating tornado outbreak on the afternoon of 27 April (CK22a,b). The next two sections will describe the environmental evolution leading to the event as seen in Figure 1.1.

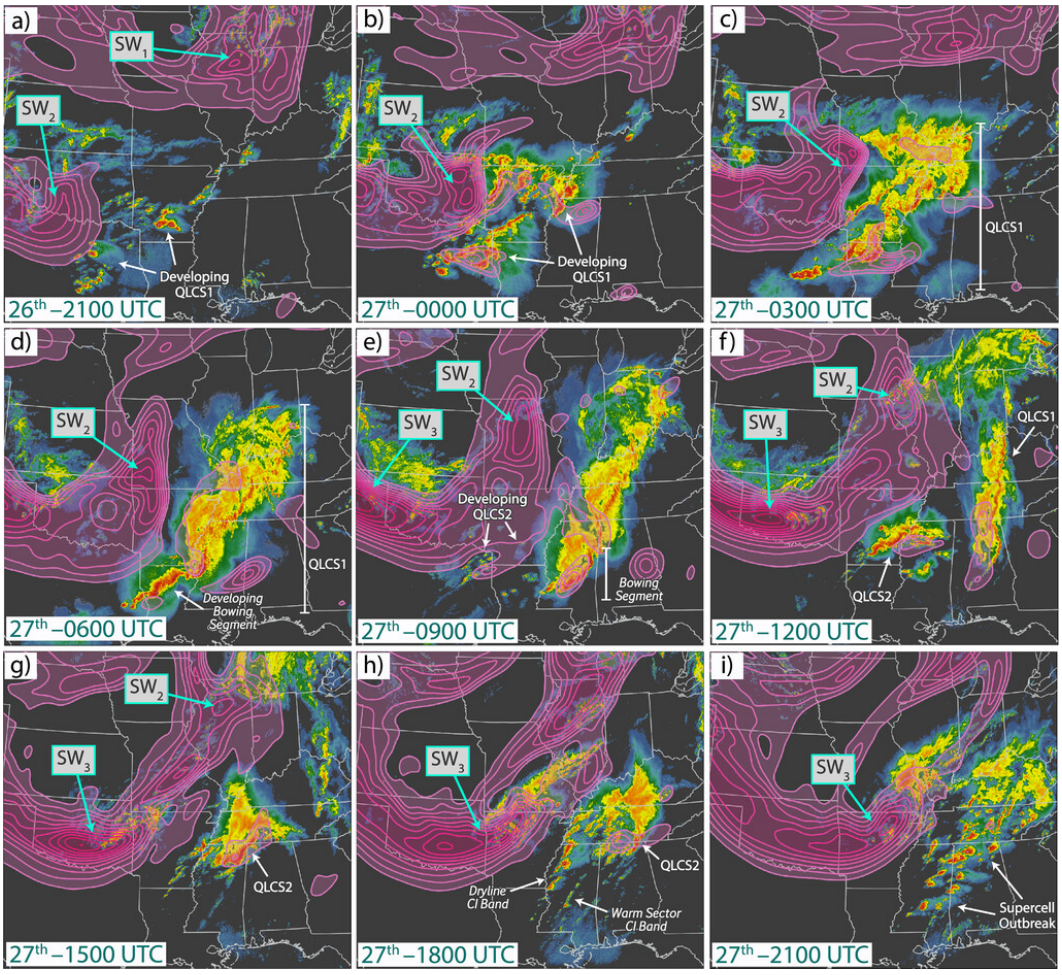

Figure 1.1: Progression of upper-level shortwave troughs and surface convection from 26-27 April 2011, from CK22b.

1.4.1 Upper-level Features

Early on 25 April, an anticyclonic Rossby-wave breaking event over the eastern Pacific led to the superposition of the polar and subtropical jets over the U.S. West Coast (CK22a,b). This resulted in an anomalously strong jet streak upstream of the long-wave trough, with wind speeds exceeding 80 m s^{-1} (CK22a). Shortwave troughs have a number of origins, but they commonly form on the lee side of mountain ranges and

along the axes of maximum wind speeds aloft (Sanders 1988). Given the strong baroclinity associated with this jet stream and its location relative to the Rocky Mountains, shortwave disturbances developed in the upper-level flow (CK22a).

The first of the three shortwave troughs ejected into the central U.S. on 25 April (CK22a,b). This trough did not directly impact the discrete tornadic convection but began the multi-day period of favorable environmental conditions for severe weather. Its evolution led to the creation of a "potential vorticity (PV) hook" structure on the tropopause and an associated Rossby-wave-breaking event mid-day on 26 April (Thorncroft et al. 1993; CK22a,b). This wave-breaking event resulted in the eastward expansion of the upper-level trough and downstream ridge amplification (CK22a,b).

The second shortwave trough followed its predecessor into the southern Great Plains later on 26 April. It was accompanied by multiple jet streaks, whose developments and evolutions will be discussed later. By 1200 UTC on 27 April, this shortwave trough propagated around the base of the longwave trough into the Great Lakes region, while the third and final shortwave entered the south-central plains. This third shortwave trough is referred to as the "primary" shortwave trough, as it provided synoptic-scale forcing for ascent for the afternoon supercell outbreak on 27 April. It was also accompanied by a deep tropopause fold. As the shortwave trough moved through the base of the longwave trough, it ended the synoptic forcing for pressure falls on the lee side of the Rocky Mountains (CK22a,b).

1.4.2 Surface/Low-level Features

The first shortwave trough aided cyclogenesis in the Central Plains and facilitated the development of an expansive warm sector in the eastern U.S. It also sparked a quasi-linear convective system (QLCS) early on 26 April, whose outflow impacted convection in the following days as an effective warm front in the warm sector (CK22a,b).

Convection that became the second QLCS formed along this effective warm front and ahead of the second shortwave trough around 2100 UTC on 26 April. With strong low-level shear from the low-level jet (LLJ) overnight, it grew upscale into an expansive system that produced almost 100 tornadoes, including many abnormally intense and long-tracking ones for the linear storm mode (Trapp et al. 2005; K14; CK22a,b).

The second shortwave trough also promoted cyclogenesis behind the second QLCS at 1200 UTC on April 27. This new low pressure system followed the second shortwave trough to the northeast as it matured, promoting a large warm sector east of the Mississippi River. The third QLCS began to form in southwest Arkansas around 1300 UTC on 27 April, aided by a destabilizing environment behind the second QLCS, and propagated generally eastward into Kentucky during the day (K14, CK22a,b). Another surface cyclone associated with the third shortwave trough formed in the wake of the previous one, as the cessation of support for pressure falls and lee cyclogenesis did not prevent a former lee trough from deepening in eastern Texas. The lack of returning southerly flow in the Central Plains allowed a Pacific front to propagate eastward behind the new surface low, while a dryline extended from the low to the gulf coast of Texas (CK22a,b). Throughout the day on 27 April, the surface low followed the synoptically-forced region of maximum ascent to the Ohio River Valley (K14), dragging the dryline east and further expanding the warm sector northward. However, the passage of multiple QLCSs created a complex warm sector, with multiple remnant thermal boundaries existing in the region before and during the supercell outbreak (K14; CK22a,b).

QLCSs (and generally MCSs) are known to have large impacts on synoptic flow patterns. PV is destroyed via diabatic processes above the level of maximum heating within convection (Wernli and Davies 1997). Large regions of deep convection such as mesoscale convective systems (MCSs) will induce large areas of PV erosion

on the tropopause. Additionally, such storms advect lower-PV air into high levels in the atmosphere, resulting in further negative PV anomalies aloft (CK22b). This can amplify synoptic waves (Grams and Archambault 2016, CK22b), potentially resulting in a blocking pattern (Pfahl et al. 2015), and strengthen upper-level flow, creating or enhancing jet streaks (Archambault et al. 2013, CK22b). On 27 April, the two QLCSs produced these diabatic effects on the synoptic pattern. They each promoted the development of a new jet streak in the upper-level flow, which in turn intensified the LLJ (CK22b).

These new jet streaks formed in close proximity within the upper-level flow, such that their right-entrance and exit regions were collocated. Following the idealized four-quadrant model for straight jet streaks (Riehl et al. 1952), this would mean regions supporting ascent and descent interfered with each other. As such, there was little support for the surface cyclones to deepen on 27 April, and rapid cyclogenesis was not a feature of this tornado outbreak (CK22a,b).

The lack of a rapidly strengthening surface cyclone and remnant cold pools from the QLCSs did not inhibit rapid destabilization to an incredibly favorable thermodynamic environment in the warm sector ahead of the afternoon supercell outbreak. Low-level southerly flow contributed to surface dew points around 21°C (70°F) throughout the region, with surface temperatures pushing 27°C (80°F; Knupp et al. 2014, hereafter K14). This contributed to low LCL heights and, combined with steep lapse rates aloft, surface-based CAPE values exceeding 2500 J kg^{-1} over much of the Southeast (Figure 1.2e, K14). The region also had extreme values of 0–1-km AGL storm-relative helicity (SRH; Davies-Jones 1984), ranging from 300 m^2 s^{-2} near the Gulf Coast to 900 m^2 s^{-2} further north where low-level shear was likely enhanced by a thermally-direct circulation associated with the remnant thermal boundaries (Figure 1.2f, K14). These

environmental conditions cumulatively produced significant tornado parameter (STP) values exceeding 10 in parts of Mississippi and Alabama (Figure 1.2g, K14).

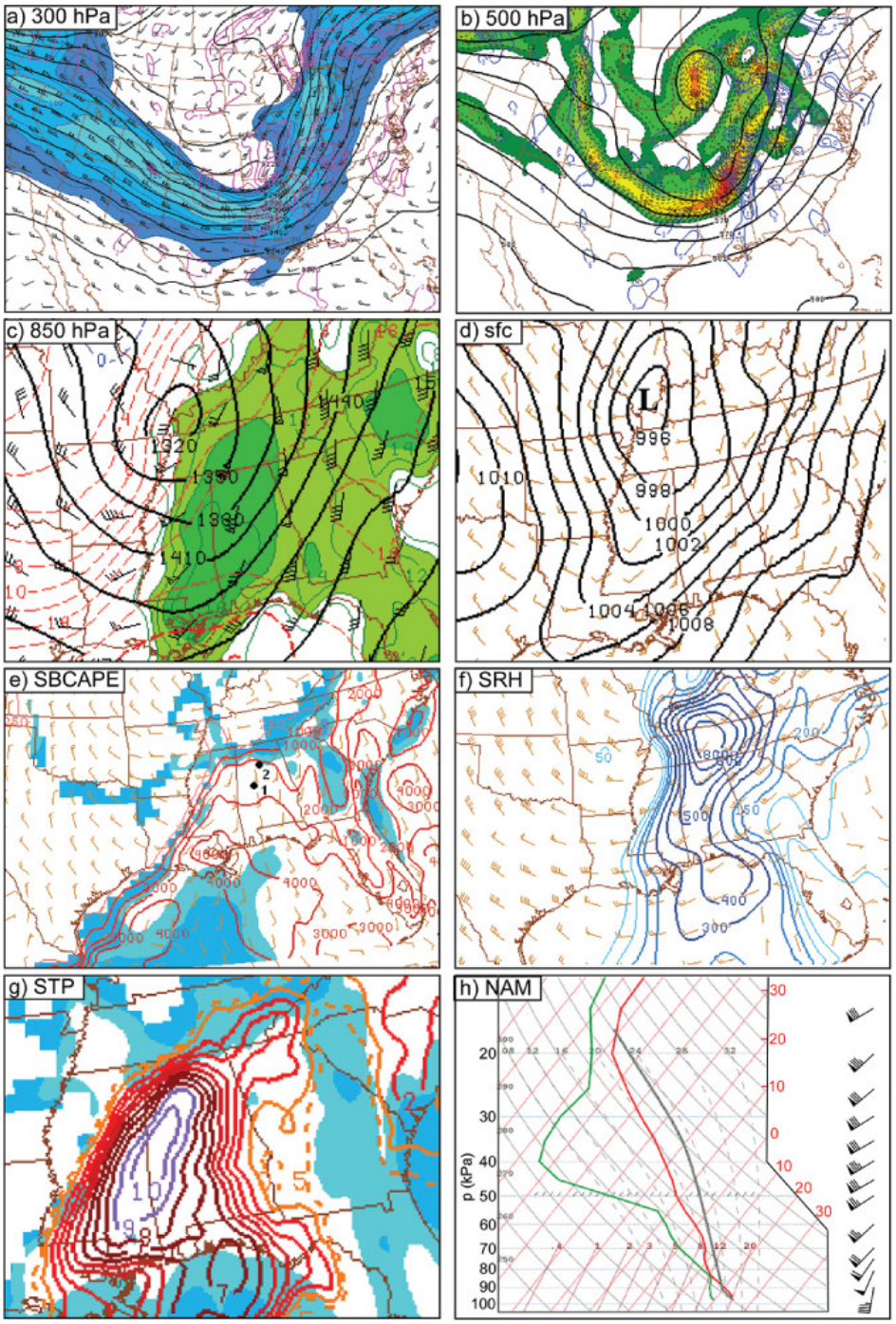

Figure 1.2: Relevant environmental parameters for the afternoon supercell outbreak, from K14.

By 1800 UTC, convection initiation (CI, defined as the time of the first 40-dBZ echo by L22 and herein) of discrete tornadic supercells was ongoing in bands near the dryline and a cold front aloft (K14; CK22a). Lyza et al. (2022) (hereafter L22) identified 29 different tornadic supercells during this event (Figure 1.3) that formed in four quasi-distinct spatiotemporal clusters. The Louisiana Delta, where storms initiated near the dryline and the Pacific front, consisted of supercells A, E, G, I, K, and L. The first of two warm sector zones, extending from south Mississippi to west-central Alabama, comprised of supercells B, H, J, O, R, S, and U. Farther north, the thermal boundary zone included supercells C, D, F, M, N, P, Q, T, V, Y, Z, and AB. These storms all initiated near the residual thermal boundaries from earlier QLCSs, although some supercells forming further south did encounter this environment later in their lifespans. The last cluster was the second warm sector cluster, stretching from south Alabama into west-central Georgia and encompassing the remaining four supercells: W, X, AA, and AC. Supercell names were assigned chronologically based on observed CI time, and alphabetically from northern-most to southern-most CI location if two storms formed at the same time.

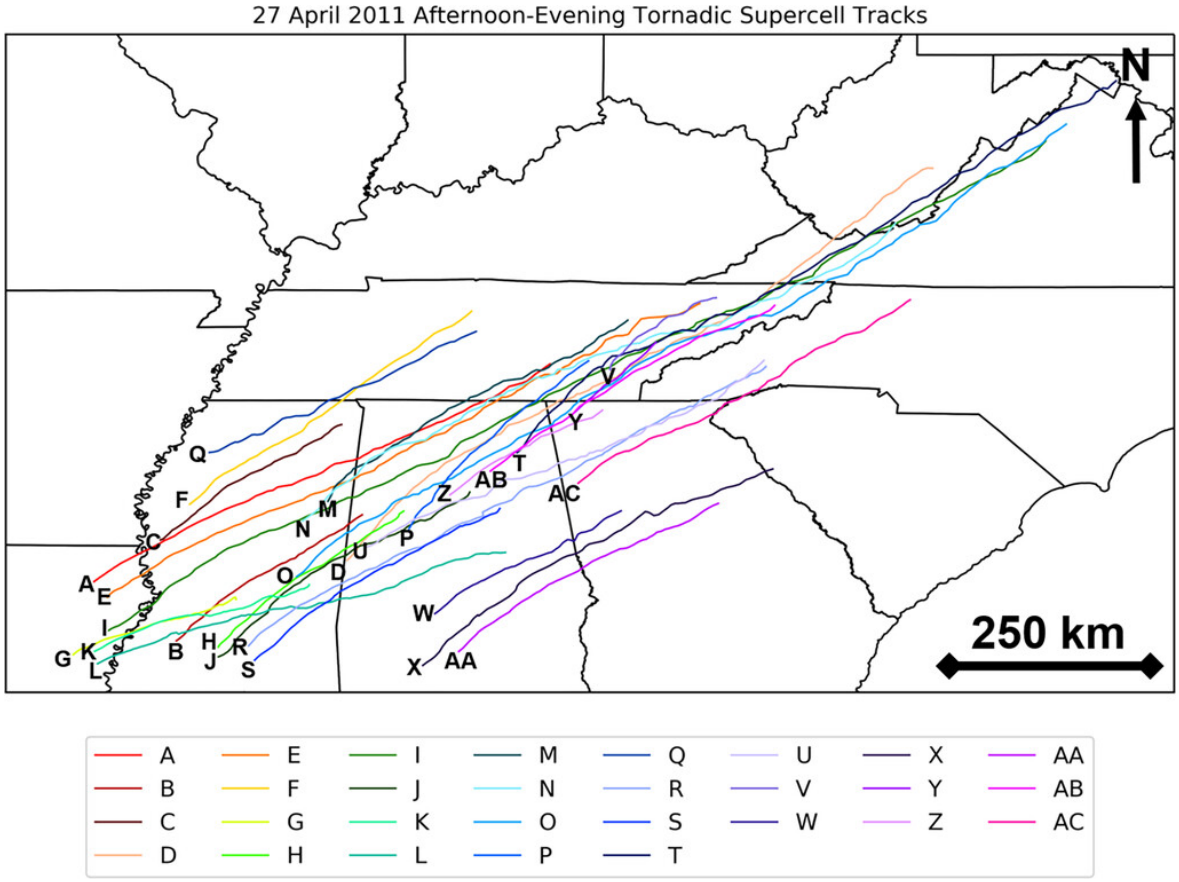

Figure 1.3: Tracks of the 29 tornadic supercells from 27 April 2011, from L22.

When stratifying storm characteristics by these clusters, L22 found regional differences that suggested varying evolutionary paths in each cluster. Supercells in the boundary zone had more intense mesocyclones, but also were relatively shorter-lived than tornadic supercells in the other three regions. L22 also highlighted a wide range in times between CI and initial tornadogenesis for the 29 supercells, spanning from less than 1 h to over 4 h. Additionally, five supercells experienced dormant periods between tornado production that exceeded 2 h, and many others exhibited shorter dormant periods.

These regional and intraregional evolutionary disparities motivate the modeling component of this thesis, which seeks to address the extend to which idealized simulations can mimic tornadic supercell evolution on 27 April based on their ambient environments alone. Given the large variations in time between CI and initial tornadogenesis seen during this outbreak in the overwhelmingly favorable yet regionally nuanced environment present in the Southeast on 27 April, this thesis will investigate any linkages between the evolution of tornadic supercells and their background environments. Specifically, we aim to answer the following question: *How much was tornadic supercell evolution on 27 April 2011 predicated by their background environments, rather than the non-homogeneous influences of terrain, cell interactions, etc?* This will be addressed both within and between the four spatiotemporal regions.

External impacts (topography, mesoscale boundaries, cell mergers/close proximity storms) were prevalent on tornadic supercells during the 27 April 2011 super outbreak. While there is a breadth of literature delving into their advantageous and disadvantageous influences on tornadogenesis, determining the exact time of tornadogenesis for any given supercell remains a major forecasting challenge (Markowski and Richardson 2009). Attempts to differentiate between tornadic and non-tornadic near-storm environments has been a focus of recent research (Thompson et al. 2003; Parker 2014; Klees et al. 2016), as well as determining practical and intrinsic predictability limits for tornadic supercells (Melhauser and Zhang 2012; Cintineo and Stensrud 2013; Zhang et al. 2015; Flora et al. 2018, 2019; Lawson 2019; Markowski 2020). By isolating the role of the background environment on 27 April 2011 Super Outbreak, we can gain insights on the predictability of similar high-impact events in the future. The application of idealized simulations for selected observed supercells on 27 April is explained in Chapter 2. Chapters 3 and 5 include our simulation results and qualitative observational analysis, respectively. The relationship between the simulated and observed evolutions of the

selected supercells is discussed in Chapter 4. Lastly, these results are synthesized and summarized in Chapter 5.

Chapter 2

Data & Methods

2.1 Storm Selection

We selected nine of the 29 tornadic supercells observed on 27 April 2011. This includes two storms from each of the four spatio-temporal clusters defined by Lyza et al. (2022) to encompass the regional evolutionary differences and increase sample size within each region. Two of the supercells, J and U, have been combined into one storm for our purposes since Supercell U formed behind J before quickly overtaking it. These two storms are hereby referred to as one storm, Supercell JU. The selected storms also exhibited varying times from CI to tornadogenesis, ranging from 48 minutes to over 3 hours. This information, including additional information regarding the life cycle and impacts of each supercell, can be found in Table 2.1.

Supercell	CI Time	Storm End	Time to Tor	Strongest Tor
M	1917	0019	48 min	EF5
A	1647	2346	181 min	EF5
R	2005	0526	145 min	EF3
L	1915	0319	207 min	EF4
JU	1823	0409	200 min	EF4
N	1924	0420	89 min	EF1
W	2350	0326	82 min	EF4
X	2355	0638	205 min	EF3

Fastest 25% Middle 50% Slowest 25%

Table 2.1: Relevant information for each of the selected supercells. CI and storm end times are in UTC.

2.2 Model Setup

This project uses version 20.3 of Cloud Model 1 (CM1; Bryan and Fritsch 2002), a nonhydrostatic numerical model, to produce simulations. The initialization soundings are shown in Figure 2.1, which are subsequently varied each hour in an attempt to emulate the evolving background environment (described more below). Important parameters are included in Table 2.2, and additional information about these soundings can be found in the section 2.2.2 below. The temperature profiles of all the soundings are largely consistent, with small variations in surface temperature. In contrast, the moisture and wind profiles display more pronounced differences, with varying degrees

of mid- and upper-level saturation, as well as low-level wind speed and direction. Regardless, they all depict extreme environments capable of producing long-lived, violent tornadoes (Cohen 2010; Thompson et al. 2012). The purpose of this project is to understand the role of the background environments on the evolutions of the selected storms. Therefore, we neglect the effects of topography and any changing surface conditions, and instead employ a constant drag coefficient (Table 2.2). Terrain-induced environmental modifications are possibly included in the base-state SFCOA analyses of some supercells, but direct orographic effects are not present in our simulations. We also neglect storm mergers and other storm interactions, which were prolific during this event.

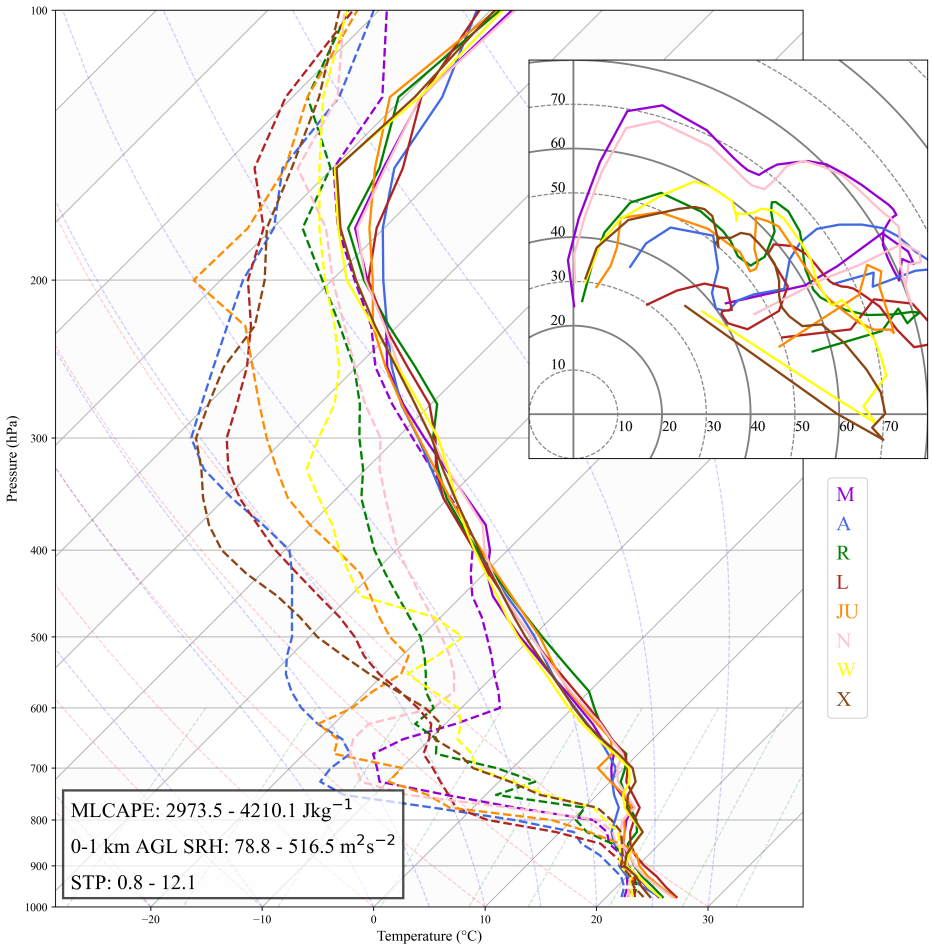

Figure 2.1: Initial base-state soundings for all 8 selected supercells. Ranges of relevant environmental parameters are included.

Parameter	Value
Horizontal Domain	96 × 96 km^2 *, 1000-m grid spacing
Vertical Domain	∼16 km (varies by storm), 500-m grid spacing
Time Step	1.5 s
Lateral Boundary Conditions	open-radiative
Bottom Boundary Condition	semi-slip; C_d=0.001
Microphysics	NSSL 2-moment

Table 2.2: Important CM1 namelist parameters.

**The horizontal domain for JU ensemble members is either 148 km^2 or 192 km^2 in an effort to keep the storms in the domain and away from the boundaries.*

2.2.1 Tendency Nudging

We use tendency nudging (Flournoy and Rasmussen 2023) as the CI mechanism, as it promotes a more gradual development of updrafts and does not create unphysical vortices early in the simulation (as seen in Markowski 2016; Roberts et al. 2016; Coffer and Parker 2017; Fischer and Dahl 2020). The strength of thermal forcing associated with tendency nudging can lead to a variety of storm characteristics and behaviors in the same environment (Flournoy and Rasmussen 2023), so we use an ensemble approach to examine varying CI regimes in these different environments. Each of the eight selected supercells has 25 ensemble members, where ensemble spread is created

by changing the duration and peak magnitude of the thermal forcing (Figure 2.2). The location and size of the thermal forcing is constant, at 2.5 km AGL and with a 5-km radius. Each suite also has an additional control simulation, where there is no tendency nudging and thus no storm.

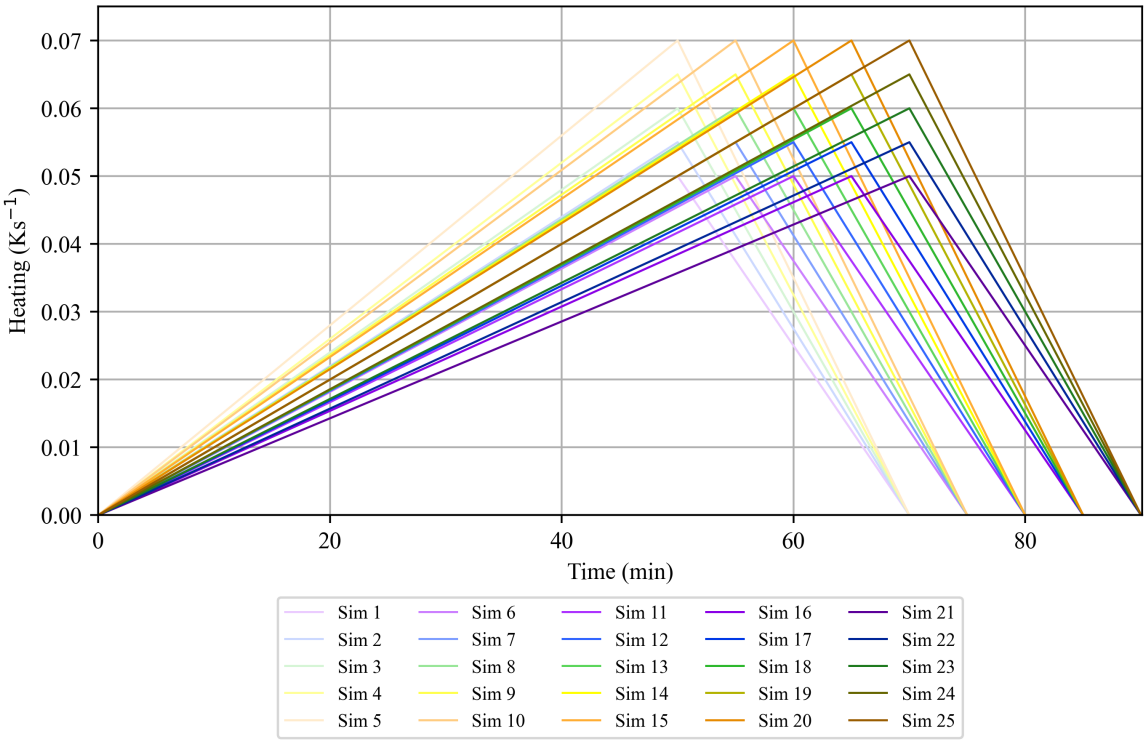

Figure 2.2: Time series of the heating tendencies for each ensemble members. These heating tendencies are identical for all eight ensemble suites.

2.2.2 Base-State Substitution

This project employs base-state substitution (BSS; Letkewicz et al. 2013), a technique that continuously and linearly replaces one horizontally homogeneous base-state environment with another at every time step while preserving the initial storm by extracting storm-induced modifications on the original base-state and applying them to the new one. Several recent studies have leveraged this method to study the effects

of a gradual environmental change, like a changing thermodynamic or kinematic profile, on a mature supercell (rather than a developing storm; Coffer and Parker 2015; Davenport and Parker 2015). Others have induced instant kinematic changes several hours into simulations to model multiple storm modes in the same thermodynamic environment (French and Parker 2014; Wipf and French 2015). This project applies BSS similarly to Davenport et al. (2019), in which the simulated environment is modified with observed soundings in "real model time," meaning the transition time between base states matches the time between the observed soundings. As such, we apply several rounds of gradual BSS in the same "real model time" to capture the near-storm environmental evolution of mature, long-lived supercells for the duration of their life cycles. BSS is applied every hour, in accordance with the availability of the hourly SFCOA analyses. This technique works with both idealized and observed soundings, so we use box-averaged soundings from each selected storms' inflow regions, bounded by the location of maximum observed low-level AzShear and captured at the top of every hour. Specifically, we use SPC mesoscale surface objective analysis (SFCOA) profiles, which are RUC soundings where the 2-m temperature, 2-m humidity, and 10-m wind has been replaced by interpolated observations (Coniglio and Jewell 2022).

Our base-state substitution framework for supercell M is included in Figure 2.3 as an example. The initial base-state environment is the closest SFCOA profile to CI time. To preserve CI characteristics as the sole source of ensemble spread, the BSS framework for each storm's ensemble suite is based on the CI time of the 13th ensemble member, which possesses the median duration and magnitude of tendency nudging. For many of the selected storms (M, R, L, JU, and N), the initial and second (input and R1) base-states are identical. These storms all initiated at least 30 min before the top of the hour allowing the supercell enough time to reach a steady-intensity before BSS begins. The remaining three observed supercells, A, W, and X, initiated less than

15 min before the top of the hour. For their ensemble suites, the second base-state sounding is from the hour following the initial one, and the start time of BSS in the model is delayed. This minor inconsistency in our BSS framework does not have an effect on the resulting simulated supercell, as transitioning to an identical base-state is the same as not transitioning at all, and is done to avoid any unknown and potentially undesirable effects within the model. All subsequent base-state transitions occur in "real model time," at hourly intervals in simulation time that match the time between the SFCOA profiles (i.e., 1 hr). This method continuously returns the modeled environment to observations and ensures our simulated supercells exist in the same near-storm environment as their observed counterparts at the same stages of the life cycles. This allows the opportunity to assess the range of evolutionary paths within each evolving background environment, with the simulated range driven by small differences in CI strength and timing. These simulated evolutionary characteristics are then compared to observed storm evolution to deduce how strongly the evolving background environment, rather than other spatially inhomogeneous factors like terrain, convergence bands, or cell mergers, influenced supercell evolution in each regime.

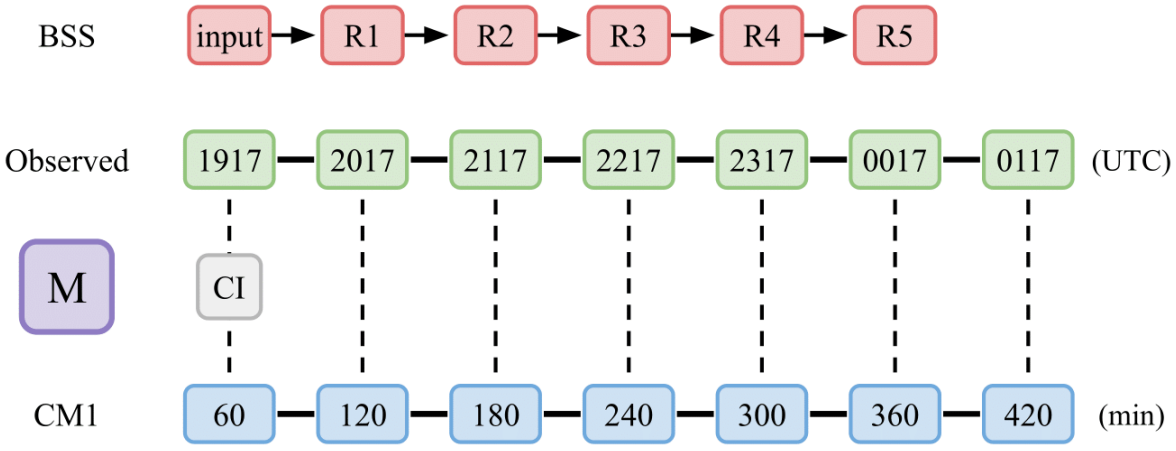

Figure 2.3: Base-state substitution framework for supercell M.

2.3 Multi-Year Reanalysis of Remotely Sensed Storms (MYRORSS) Azimuthal Shear Analyses

There are two methods for calculating azimuthal shear from a radar-derived velocity field. The more traditional, "gate-to-gate" technique (Equation 2.1), is simply the difference between two adjacent velocity signatures divided by the azimuthal distance between them. The second, preferred, linear least squares derivatives (LLSD) method (Equation 2.2) fits the velocity field to a low-order model and incorporates neighboring shear values into the calculation, reducing the effects of noise and individual velocity signatures on the final product (Smith and Elmore 2004; Newman et al. 2013; Mahalik et al. 2019).

$$u_{as} = \frac{V_{max} - V_{min}}{d} \tag{2.1}$$

$$u_s = \frac{\sum s_{ij} u_{ij} w_{ij}}{\sum (\Delta s_{ij})^2 w_{ij}} \tag{2.2}$$

L22 created a dataset of maximum low- and mid-level LLSD azimuthal shear (AzShear) at 5-min increments for the entire duration of each supercell identified from 1200 UTC 27 April 2011 to 1200 UTC 28 April 2011. AzShear maxima were determined in 2-h segments following storm motion with a 20-km buffer, followed by a manual correction of any erroneous values attributed to nearby cells within the 20-km buffer (L22). These AzShear timeseries serve as a simple representation of the strength of rotation in the low- and mid-levels (0–3-km AGL and 3–6-km AGL, respectively) of the observed supercells. They are not a perfect representation of storm-scale rotation,

since velocity fields, and thus AzShear fields, are range-dependent. As such, stronger rotations further from a radar could appear weaker than reality (Smith and Elmore 2004; Newman et al. 2013). Regardless, this project ignores range-related issues and uses simulated vertical vorticity as a proxy for observed AzShear. Specifically, the maximum vertical vorticity in the 10-m to 3-km-AGL layer of our simulations is used as a proxy for observed low-level AzShear, and maximum vertical vorticity in the 3–6-km layer for observed mid-level AzShear.

2.4 Analysis: Early Evolution Focus

Although the simulations were generated for the entire lifespans of the eight selected supercells, which exceeded 10 h for some, most of our analysis will focus on the early evolution periods of the supercells. We defined this as the first 4 h after CI for two main reasons. First, by this point, all observed supercells had produced at least one tornado. One of the main drivers for this project is the large variation in time between observed CI and initial tornadogenesis, despite all of the storms existing in environments extremely favorable for tornadoes. The spatial resolution of our simulations is too coarse to resolve tornado-like vortices, so we cannot fully compare the production of our simulations to observations. However, assuming our simulations follow the same evolutionary trends as their observed counterparts, we can observe evolutionary stages that are resolved with 1-km grid spacing (low- and mid-level mesocyclone characteristics, etc).

Updraft helicity (UH) is one of our primary measures of storm strength, as it is often used as a forecasting tool for mesocyclones (and tornadoes) in both the mid- and low-levels (Kain et al. 2008; Sobash et al. 2016b,a). UH integrated through the 2-5 km AGL is a CM1 output variable, where it is calculated as defined in Kain et

al. 2008 (Equation 2.3). Similarly, we calculated UH through the 0-3-km layer. Our simulations produce discrete data points every 500 m in the vertical, so the equation becomes a summation, as seen in Equation 2.4. Here, Δz is 10 m for the lowest data point, as the lowest grid level in our simulations is at 10 m AGL. Through the rest of the layer, Δz is constant at 500 m.

$$UH = \int_{0km}^{3km} w\zeta dz \tag{2.3}$$

$$UH = \sum_{0km}^{3km} w\zeta \Delta z \tag{2.4}$$

The second reason we focus our analysis on the early evolution period of our simulated supercells is that we start to lose reliable data as we progress further into the simulations due to the formation of linear bands of reflectivity (Figure 2.4). The bands form primarily in the inflow region of the supercells, but in many ensembles behind the supercell as well, and move perpendicular to their N-S or E-W orientations. The occurrence of these bands varies, as they are absent in some ensemble suites, yet appear in all 25 members of others. In individual ensembles, some bands are transient while others become dominant features that engulf the supercell, reducing it to disorganized convection that fills the domain.

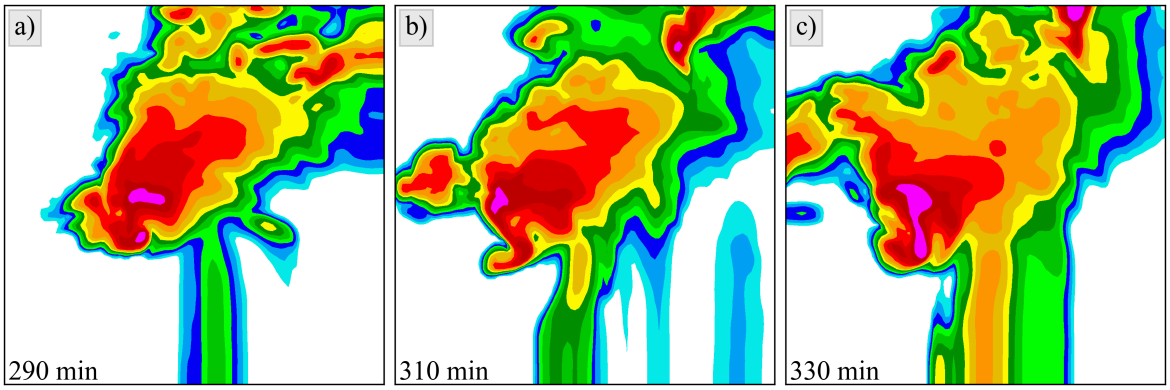

Figure 2.4: Reflectivity at 1 km AGL for Supercell M, ensemble member 4, at 290 min, 310 min, and 330 min into the simulation.

Determining the exact cause of these reflectivity bands is beyond the scope of this project, but we preliminarily concluded that they are the unphysical numerical manifestation of Kelvin-Helmholtz (KH) instabilities, a realistic feature in supercell environments. KH instabilities form when the gradient Richardson number (R_i) drops below its critical value of 0.25 (Lin 2008, p. 253). Since the gradient R_i (Equation (2.5)) is a ratio of static stability to vertical wind shear, near-surface supercell environments characterized by low static stability and strong wind shear will have small R_i that potentially fall below the critical value. To eliminate the effects of these bands on our analysis, we exclude all time steps for an ensemble member after which a band with a 40-dBZ echo has merged with the 10-dBZ echo region of the supercell. The 40-dBZ threshold aligns with our definition of CI, ensuring that only convective and temporally persistent bands are considered. We refrain from excluding time steps at the initial appearance of a reflectivity band, as associated low-level environmental changes are generally minimal and localized. This "banding" issue appears to be a problem in other idealized studies of supercell evolution (C. Davenport, personal communication) and might warrant further investigation, especially as it pertains to HSLC environments.

$$R_i = \frac{g\beta}{(\frac{\partial u}{\partial z})^2} \approx \frac{g\frac{\partial \theta}{\partial z}}{(\frac{\partial u}{\partial z})^2} \tag{2.5}$$

Chapter 3

Simulation Outcomes

3.1 CI timescales

The eight ensemble suites include the same CI characteristics, so differences in storm outcomes between the ensembles are attributed to environmental differences. To evaluate the development speed of storms in these environments across the CI regimes, we compare the median times that each suite reached thresholds representative of storm strength: CI time, updraft strength, and mid-level mesocyclone strength (Figure 3.1).

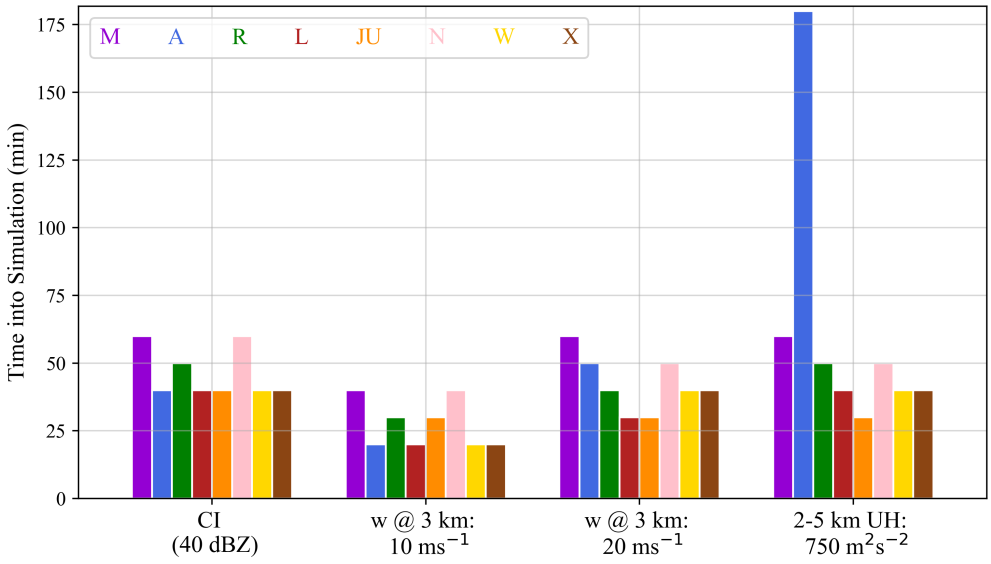

Figure 3.1: Bar plot showing the median time for various thresholds to be met. Bars are color-coded by storm. The thresholds are CI (first 40 dBZ-echo), a 10-ms^{-1} updraft at 3 km AGL, a 20-ms^{-1} updraft at 3 km AGL, and 750 m^2 s^{-2} of 2–5-km AGL updraft helicity (UH). 0–3-km AGL UH is not included as it is the same as 2–5-km AGL UH.

Based on these thresholds, we can separate the storm suites into faster and slower developing groups. Storms L, JU, W, and X generally reached the key thresholds earlier in the simulations and thus populated the faster group, while storms M, N, A, and R fell into the slower group. Supercells R, JU, and N developed mid-level mesocyclones before reaching our definition of CI. Meanwhile, it appears that storm A took significantly longer than any other ensemble suite to develop a mid-level mesocyclone. However, it is important to note that while the median CI time for storm A is 40 min into the simulation, the initial convection across all ensemble members dissipated while CI for the eventual supercell occurred 100–110 min into the simulations. Thus, supercell A

still fell into the slower developing group, but the development time of the supercell itself was not an outlier.

3.2 Mesocyclone Evolution

Despite the overwhelmingly favorable environments for deep, organized convection, the eight ensemble suites yielded a wide range of storm outcomes after CI. Figure 3.2 shows bulk statistics of 2–5-km AGL UH in these suites for their entire lifespans, as well as the number of ensemble members contributing to the plotted quantities. 2–5-km AGL UH will be the primary storm attribute for assessing simulated storm strength, as it accounts for updraft strength and storm structure and organization.

The simulations for supercells M, N, A, R, and W were able to sustain storms with varying degrees of success. Supercells M and N maintained or increased their intensities following the cessation of the heating tendencies, with minimal variation among their ensembles. Storms W and R experienced brief but rapid de-intensification at the immediate end of tendency nudging, before settling at a weaker strength. Supercell W maintained this weaker strength for the duration of its lifespan, whereas storm R eventually re-intensified to the greatest intensity of all the ensemble suites around 4 h after CI. In terms of 2–5-km AGL UH, storm A remained weak from CI to storm dissipation. It featured the most convoluted CI process of the eight selected storms, with spurious convection preceding the eventual supercell and likely affecting the low-level inflow environment. Storm A also included considerable variety in storm outcomes, with some CI regimes failing to sustain convection and others producing secondary cells alongside the main supercell (Figure 3.3). Although supercell A's suite could be considered as an intermediate case, given its diversity in storm outcomes and relatively weak intensity of sustained convection, the presence of persistent convection accompanied by non-zero

values for 2–5-km AGL UH motivates its inclusion as a "successful" suite. The suites for L and X failed to sustain organized convection after the heating tendency stopped. Although storm JU appeared to restrengthen several hours into its simulations, the near-zero values of 2–5-km AGL UH between 150 and 210 min across all ensemble members introduce uncertainty as to whether the re-intensified storms remain linked to the initial heating tendency. Additionally, this discontinuity in intensity occurs at the end of our early evolution period, so the subsequent restrengthening is excluded from further analysis. Thus, the suite of storm JU is treated as another case in which deep, organized convection was not maintained following the cessation of the imposed heating tendencies.

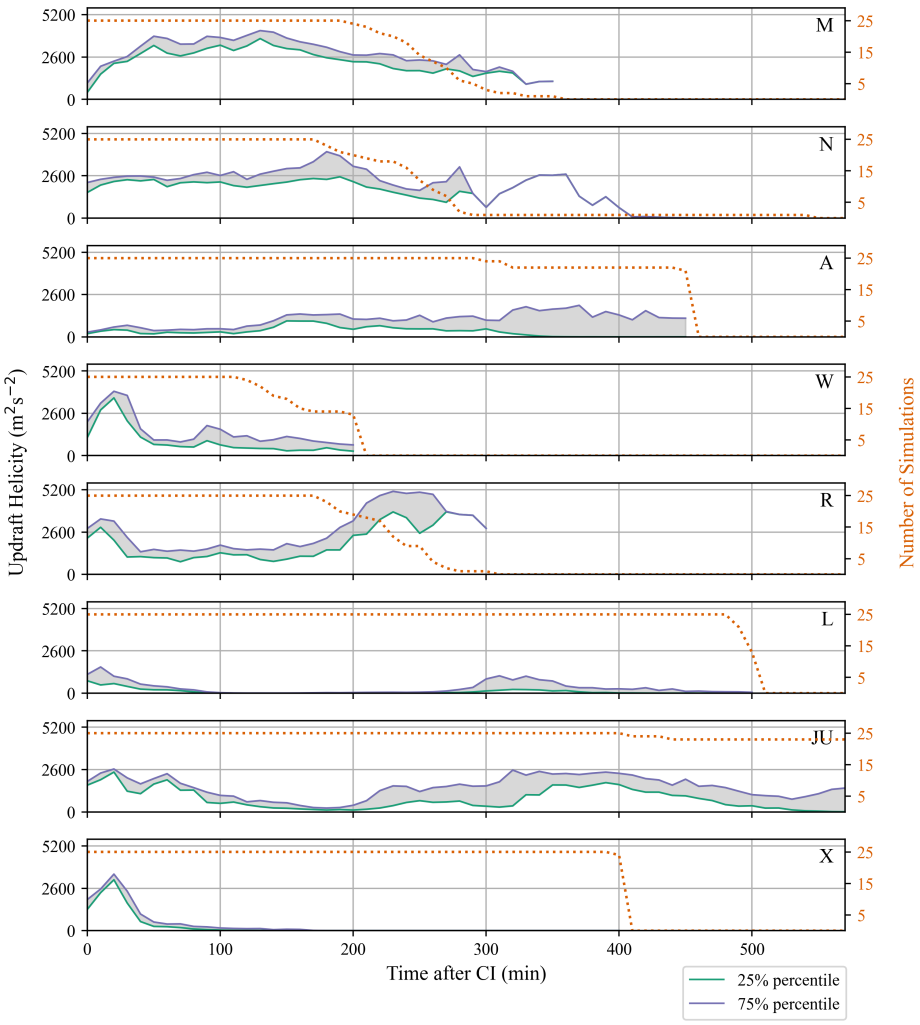

Figure 3.2: Time series for 25th percentile (green line), 75th percentile (purple line), and IQR (gray shading) for maximum 2–5-km-AGL UH after CI for each storm's ensemble suite. Each storm has a panel, and the panels are arranged by latitude of observed CI, so the northern-most initiating supercell is at the top and the southern-most at the bottom. The orange dashed line represents the number of ensemble members that have not experienced an unphysical reflectivity band merging with the main supercell at each time.

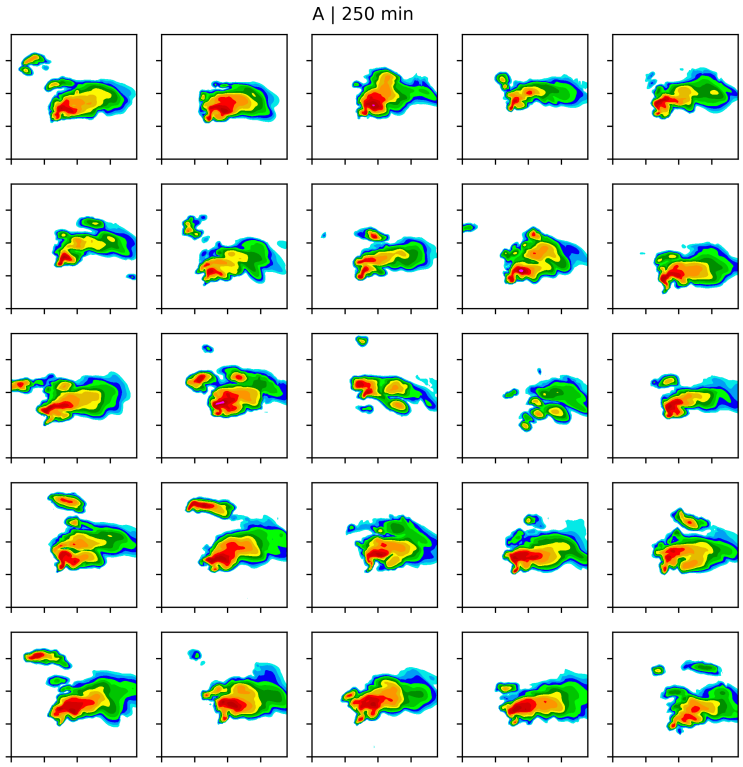

Figure 3.3: Simulated reflectivity fields of at 1 km AGL, 250 min into the simulations, for all 25 CI regimes of storm A.

3.2.1 Time-Height Evolution of Successful-Suite Mesocyclones

As established above, supercells M and N are the only two storms whose ensemble members do not exhibit any artificial intensity peaks just after CI due to the continuation of the heating tendency. This allows us to analyze their mesocyclone evolutions for the entire 4 h after CI. Specifically, we can examine the vertical structure of updraft helicity in time for the early evolution period of our simulated suites. This is especially

interesting given their similar environments and close observed proximity, but varying evolutionary paths that are captured to some degree in our idealized simulations.

Supercell M's mesocyclone maintained a relatively constant vertical location of its maximum strength, around 3 km AGL, for the duration of its lifespan. The mesocyclone intensity appears to pulse before achieving its maximum overall strength a little over 2 h after CI. Meanwhile, supercell N, which formed and existed in close proximity to Supercell M in a nearly-identical observed environment, displayed a more typical mesocyclone evolution (Davies-Jones 2015). Its peak intensity was further aloft, at least 6 km AGL, for the first 2 h of the storm's lifespan. The mesocyclone then reached its peak intensity 3 h after CI, which correlates with a rapid descent of the vertical maxima to around 3 km AGL (Figure 3.4).

Storms A, W, and R all have artificial peaks in mid-level mesocyclone strength followed by a "dormant" period, where updraft helicity is less than 300 $m^2\ s^{-2}$ throughout the 10-m to 6-km AGL layer. All three eventually re-develop a mesocyclone, although for Supercell A it is unclear if these new updrafts are independent of the model domain boundaries or other unphysical features within CM1. Once the ensembles of storm W redevelop their mesocyclones, they maintain a very weak, low-altitude peak intensity before weakening at the end of their lifespans (Figure 3.4).

Supercell R, on the other hand, maintains a similarly weak and low-altitude peak mesocyclone intensity until it rapidly strengthens throughout the entire 10-m to 6-km layer. This rapid intensification occurs during the transition from the third base-state to the fourth. These two environments are very similar, with small changes to already extreme amounts of CAPE and shear (Figure 3.5). The most noticeable change is the dissolution of a warm nose in the temperature profile at 700 hPa and in turn an increase in 850–500-hPa lapse rates. High 700-hPa temperatures in environments with low LCL heights can inhibit deep moist convection, although this can be overcome

with sufficient mesoscale forcing below 700 hPa (Bunkers et al. 2010). It appears that this is the case for Supercell R, where the heating tendency in the first 70–90 min of the simulations provided sufficient lift to overcome environmental CIN. However, the warm nose was still in place after the heating tendency ended, somewhat suppressing the convection until it eroded around 0000 UTC 28 April, 4 h later.

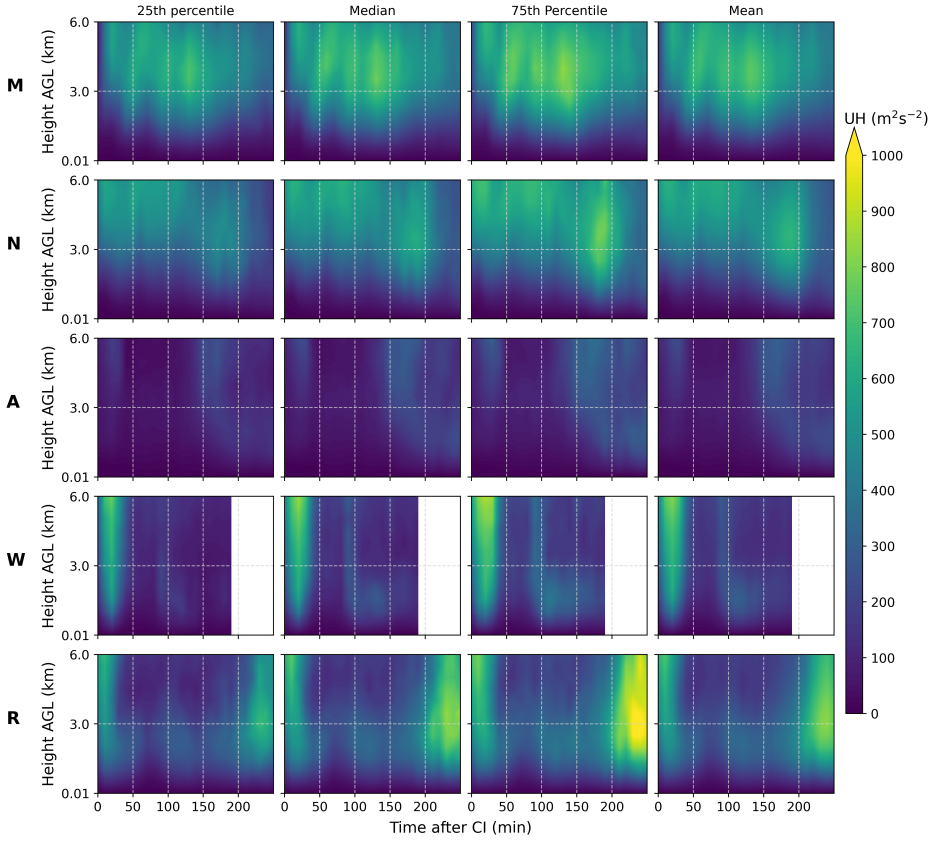

Figure 3.4: Time-height plots of 25th percentile, 75th percentile, median, and maximum UH. UH is calculated in 500-m layers, as that is the vertical resolution of our simulations for the ensemble suites of supercells M, N, and W. Only the early evolution period (first 4 h after CI) is shown for M and N. The entire life span of storm W is shown because it lost supercell characteristics less than 4 h after CI.

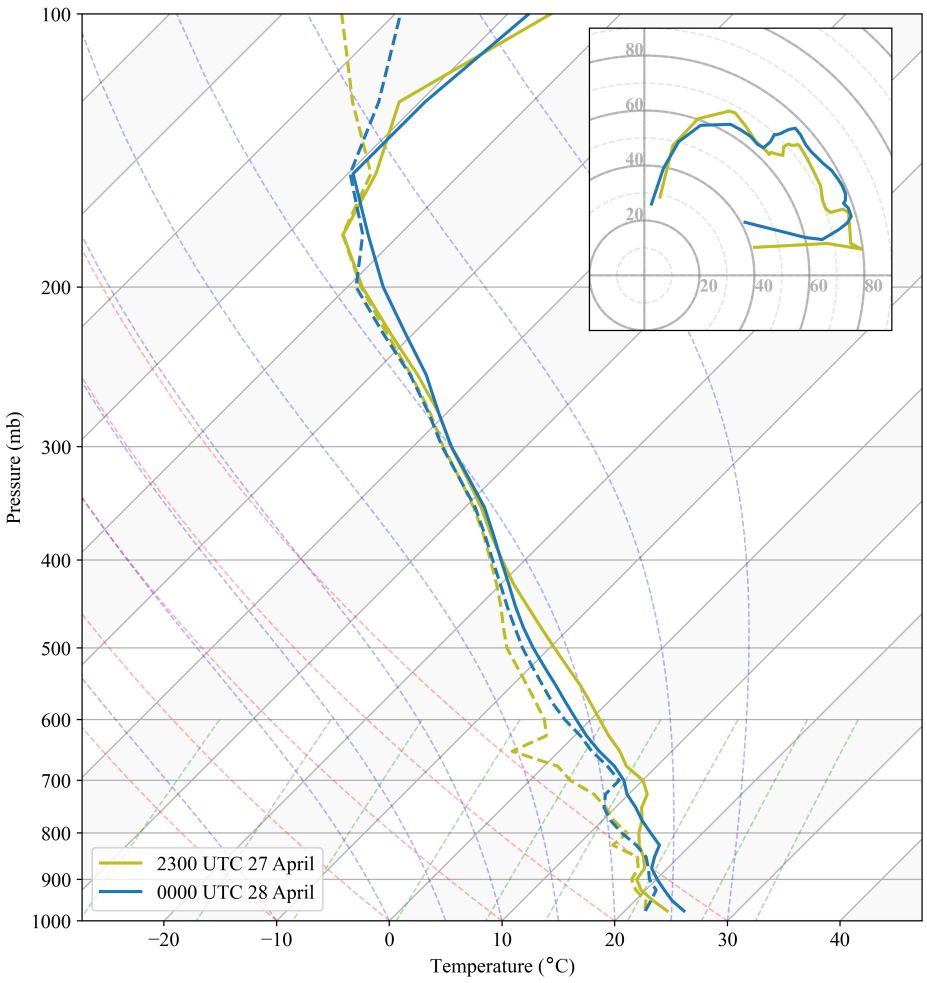

Figure 3.5: SFCOA soundings and hodographs of supercell R's 3rd (olive) and 4th (blue) base-state environments. Solid lines indicate temperature profiles; dashed, moisture profiles.

3.3 Simulated Environmental Characteristics

The environmental evolution within each CM1 domain generally follows the same trends present in the corresponding base-state evolution, although the magnitudes of the thermodynamic and kinematic parameters included in Figure 3.6 are not as

precisely followed. The largest deviation of the simulated environment from the base-state soundings is in the kinematic environment for supercell M, which contains up to 25% more deep-layer shear than the base-state. As BSS only alters the base-state and preserves storm-induced environmental changes, this means the simulated supercell greatly modified its ambient environmental wind field. Our domain is only 96×96 km^2, so a storm roughly centered in the x- and y-directions is no further than 64 km from the lower right corner, in which soundings were captured. Additionally, the presence of the linear reflectivity bands shifted this location in the negative x-direction in many cases, meaning the sounding would be even closer to the supercell. Proximity soundings and idealized simulations have shown strong supercells can induce large increases in low-level shear and the overall length of the hodograph as far as 60 km away (Weisman et al. 1998; Potvin et al. 2010; Nowotarski and Markowski 2016), so it is entirely possible that the simulated storm updraft modified the environment in the whole domain. The same studies established a similar storm-induced decrease in CAPE, which appears to be present in these simulations as simulated MLCAPE is less than or equal to observed MLCAPE for almost every suite at every time.

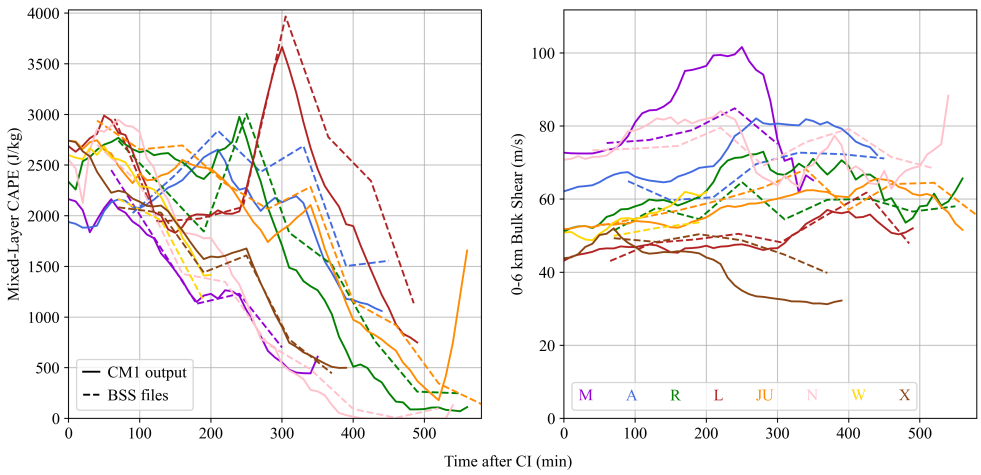

Figure 3.6: Timeseries of select thermodynamic (here, MLCAPE) and kinematic (here, 0-6 km Bulk Shear) parameters in our simulated (solid line) and BSS (dashed line) environments. The simulated timeseries depict ensemble-median values for each storm suite.

The extent of these environmental modifications depends on storm strength. To get a consistent picture of the background environments our simulated storms existed in regardless of their intensities, we can in part focus on relevant characteristics of our BSS environments, as they are what the simulated environment is continuously being returned to, and our control simulation environments, where there is no convection present. Specifically, we can focus on the first two BSS environments for each suite, as any storm demise occurred either during the full implementation of the initial environment or the transition to the second. Of the four spatiotemporal regions from which we selected observed supercells, two had a clear successful and unsuccessful cases (R/JU, W/X). In these environments, the more successful case (R and W) was significantly more moist in the mid- and upper-levels (Figure 3.7). The boundary region, where supercells M and N resided, was initially much more moist for supercell M, before being

roughly the same level of saturation throughout the vertical profile for both an hour later. The suites of both M and N successfully produced strong simulated supercells across all ensemble members, with the only difference being the more rapid development of supercell M, potentially attributable to the relatively more moist environment aloft. The moisture profiles of the last regional pair, Storms A and L, are much more alike than in the other regions. They are also two of the least-saturated simulations in the mid- and upper-levels (Figure 3.8). It is well-known that drier environments aloft are less supportive for sustained deep convection (Gilmore and Wicker 1998; James and Markowski 2010).

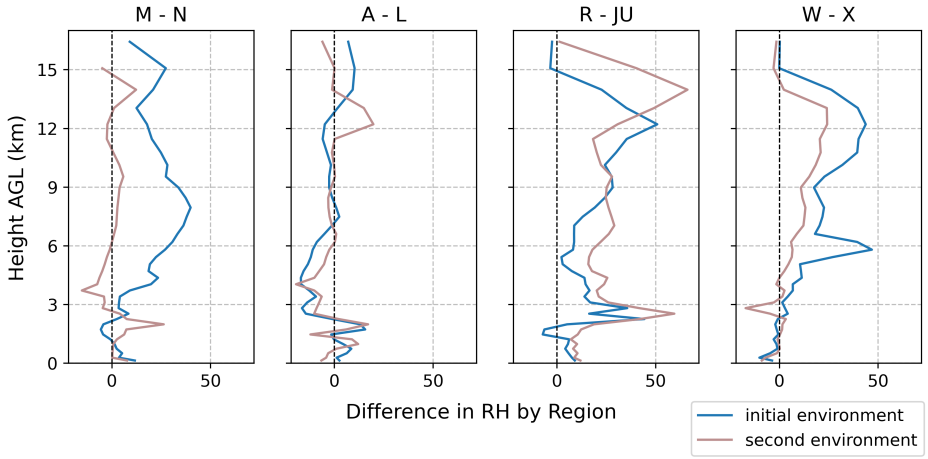

Figure 3.7: Vertical profiles of the difference in relative humidity for each supercell's initial (blue) and second (purple) base-state environments. The storms are grouped by region, and the relative humidity of the less-successfully simulated storm outcome is subtracted from the more successful storm.

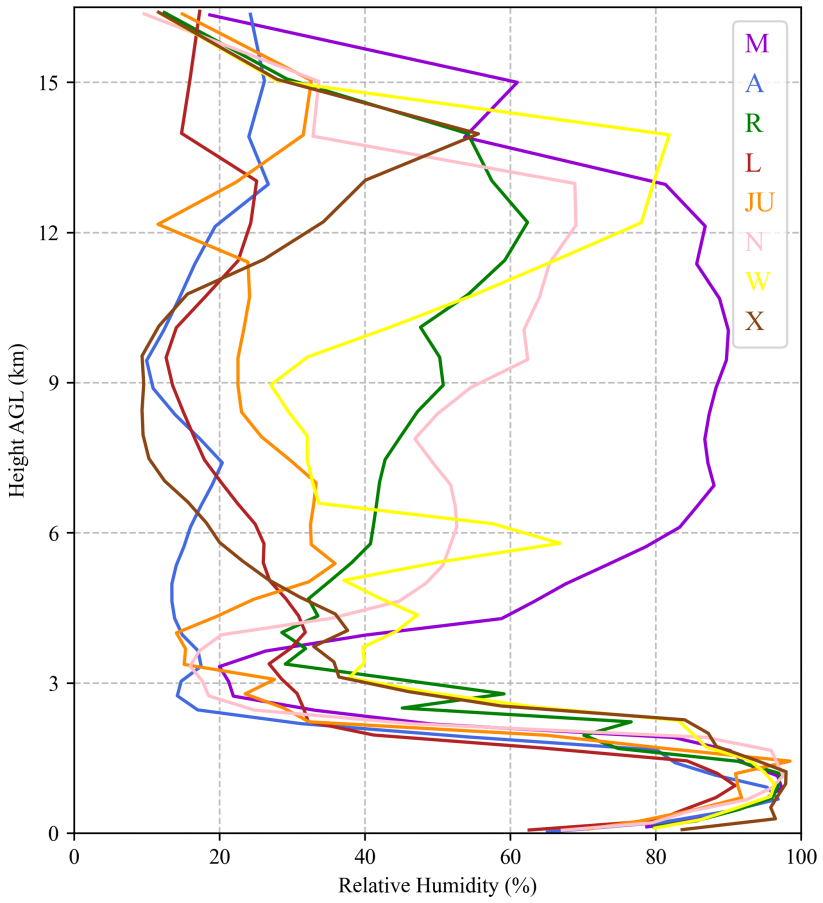

Figure 3.8: Moisture profiles for each storm's initial base-state.

By 100 min into the simulations, tendency nudging had ended across all of the CI regimes and simulated convection is down-trending in ensemble suites that failed to sustain convection. At this time, the control environments of these unsuccessful suites, L, JU, and X, all appear to be dryer in the mid- and upper-levels (Figure 3.9). Additionally, they have local maxima in their vertical shear profiles at the same vertical level as local minima in saturation (2.5 km for L, 3 and 4 km for JU, 3.5 km for X),

indicative of greater potential entrainment for the developing updrafts. Storms A and W also appear to have these features (2.5 km for A, 3.5 for W), but were still able to sustain some convection. Supercell W has a relatively deep, near-fully saturated layer near the surface that likely allowed for the development of a robust updraft more resistant to entrainment. Supercell A, on the other hand, does not have a deep moist layer. It was, however, the weakest of the "successful" suites, and had the greatest amount of variability among ensemble members. The remaining successful suites, M, N, and R, all possess corresponding local minima in shear and saturation in their control environments, implying that they had less entrainment to overcome despite dry layers around 3 km AGL.

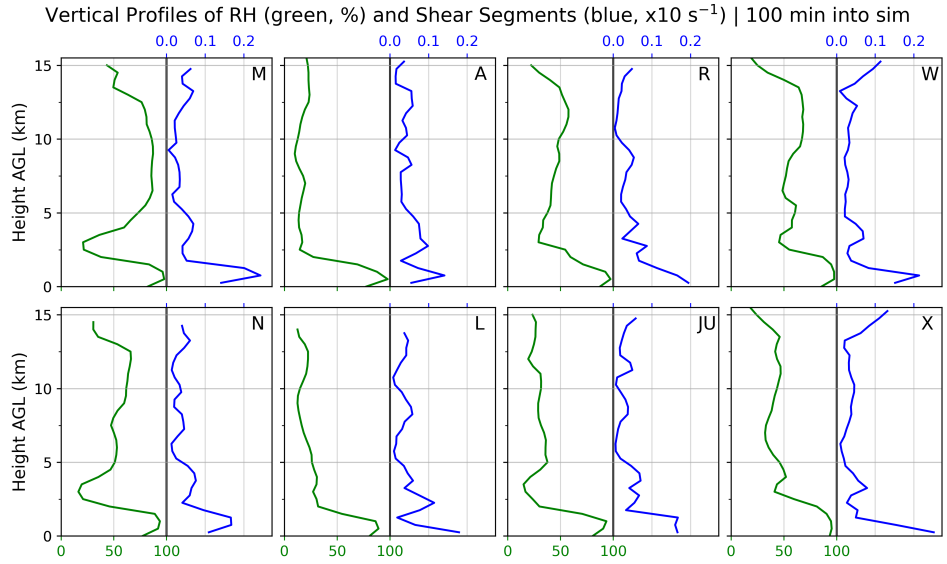

Figure 3.9: Vertical profiles of relative humidity (green) and shear segments (blue) 100 min into the control simulations (no storms initiated) for each supercell. Columns are arranged by the region of the observed storms, and the top row is generally the more successful storm in each region.

3.4 Storm Attributes and Environmental Predictors

The purpose of this project is to understand to role of the background environment on tornadic supercell evolution during the 27 April 2011 tornado outbreak. Our analysis of both observations and our control simulations revealed that the presence of drier air aloft can distinguish between our successful and unsuccessful simulation suites. We can further investigate relevant environmental parameters within our ensemble suites, including local modifications from our simulated storms, to look for any correlations between specific environmental characteristics and storm strength. As this likely depends on CI characteristics, it will be done for each CI regime in both a collective assessment of all storms in each regime and individual storm evaluations.

Mid-level mesocyclone strength exhibits statistically significant, positive correlation with kinematic parameters such as 10-m to 1-km SRH (0–1 SRH) in all 25 CI regimes (Figure 3.10). These correlations are strongest in regimes characterized by weaker and shorter-duration heating tendencies, as shown by larger correlation coefficients in the left- and top-most panels of Figure 3.10. Stronger and longer-duration CI regimes also present statistically significant, positive relationships, but the correlations tend to be weaker. While only 0–1 SRH is included, the same trends are observed when comparing mesocyclone strength to other kinematic parameters across various layer depths.

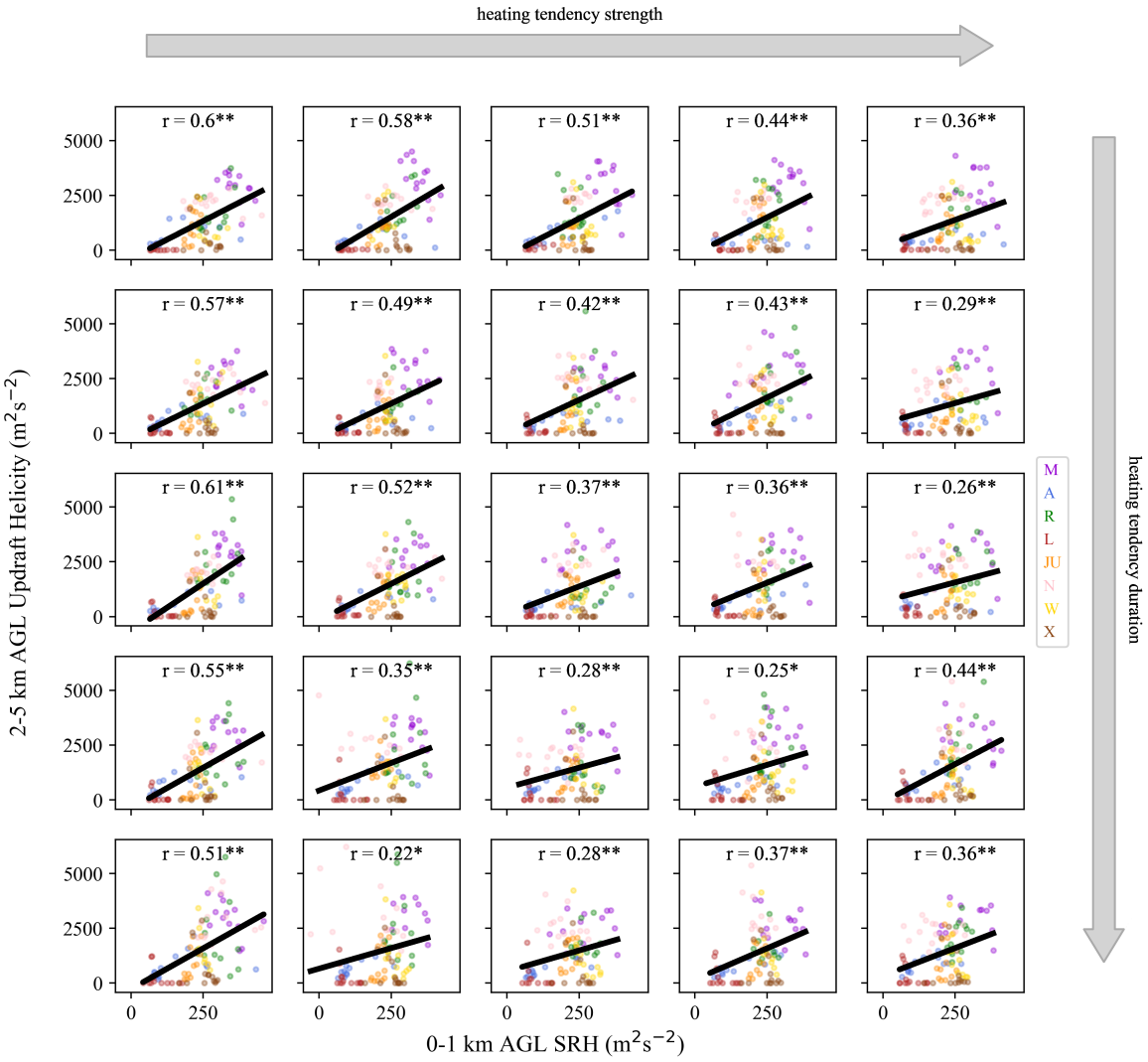

Figure 3.10: Scatter plots of 2–5-km AGL UH vs. 0–1-km AGL SRH during the early evolution period. Each panel is a different CI regime, with increasing magnitude of tendency nudging from left to right and increasing duration from top to bottom. Each dot, color-coded by storm, represents a 20-min average of the simulated quantities that reduce the effects of persistence in consecutive time steps. The black lines denotes the line of best fit across all the storms in each CI regime. Association correlation coefficients are displayed in the same panels. The asterisks denote statistical significance (* $p < .05$, ** $p < .01$).

Mid-level mesocyclone strength shows little dependence on MLCAPE (Figure 3.11) and other thermodynamic parameters (not shown), regardless of the CI regime. Across every regime, the correlation between mesocyclone strength and MLCAPE was negligible, with statistically significant, near-zero correlation coefficients in almost every regime. Therefore, there is no evidence of a linear relationship between MLCAPE and mesocyclone strength when considering all storms collectively.

In our simulations, the strongest supercells existed in greater low-level and bulk shear, particularly after weaker and shorter-duration CI. In contrast, the amount of available CAPE was not an influencing factor. This is not unexpected, as long-lived supercells are known to exist in greater deep bulk shear and stronger storm-relative winds (Bunkers et al. 2006). Long-lived supercells also tend to experience decreasing CAPE throughout their lifespans due to the early-evening transition and loss of insolation (Davenport 2021). While similar statistical analysis cannot be performed on individual ensembles within each storm suite due to limited sample sizes, stemming from the use of 20-min averaging to reduce autocorrelation in the early evolution period, qualitative trends between storm attributes and environmental predictors can still be observed. For simplicity and conciseness, only the two environmental predictors used above are included in this portion of the analysis.

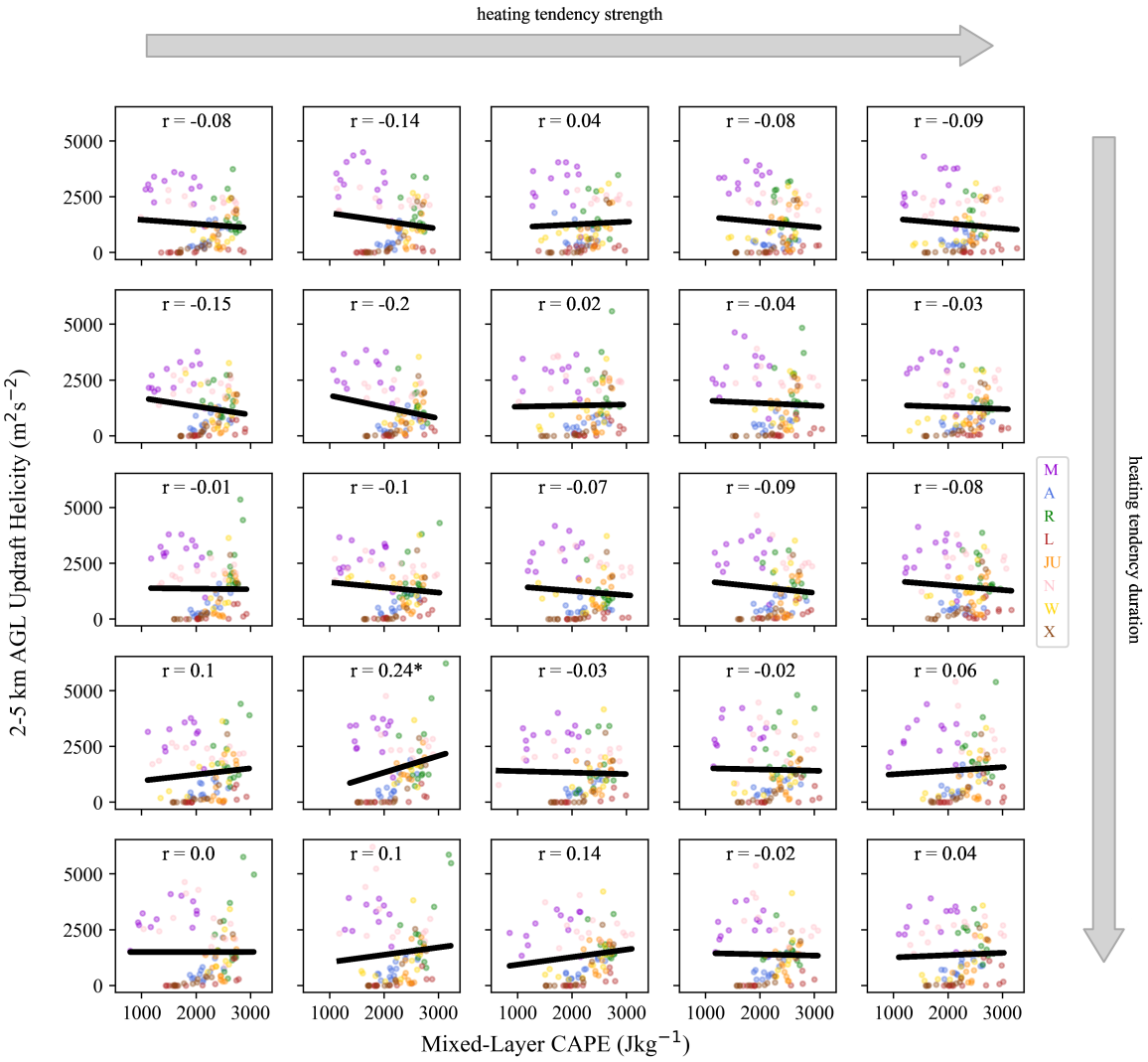

Figure 3.11: As in Figure 3.10, except for 2-5 km AGL UH and MLCAPE.

Three of the successful suites (M, N, W), show negative correlations between mid-level mesocyclone strength and 0–1 SRH. Of these, they are only statistically significant for a majority of ensemble members for storm W, indicating that these negative correlations for storms M and N can likely be attributed to other factors. For storm W, the statistically significant relationships are mainly for stronger and longer-duration heating tendencies. Storm A has a weakly positive correlation between these two

parameters, and statistically-significant relationships are concentrated in the longer-duration CI regimes. When comparing the 0–1 SRH to low-level mesocyclone strength (not shown), almost all of the CI regimes contain significant relationships. The type of relationship between mid-level mesocyclone strength and 0–1 SRH in storm R's ensembles varies, with both positive and negative correlations present. However, like storms M and N, they are mostly statistically insignificant and it is unlikely that trends in mesocyclone strength are due to 0–1 SRH. Of the unsuccessful suites (L, JU, X), storms L and X appear to have weakly negative, yet statistically insignificant, relationships across all of their ensembles. Almost half of the ensembles of storm JU contain statistically significant relationships with 0–1 SRH, and these are all strongly positive correlations concentrated in the longer-duration CI regimes.

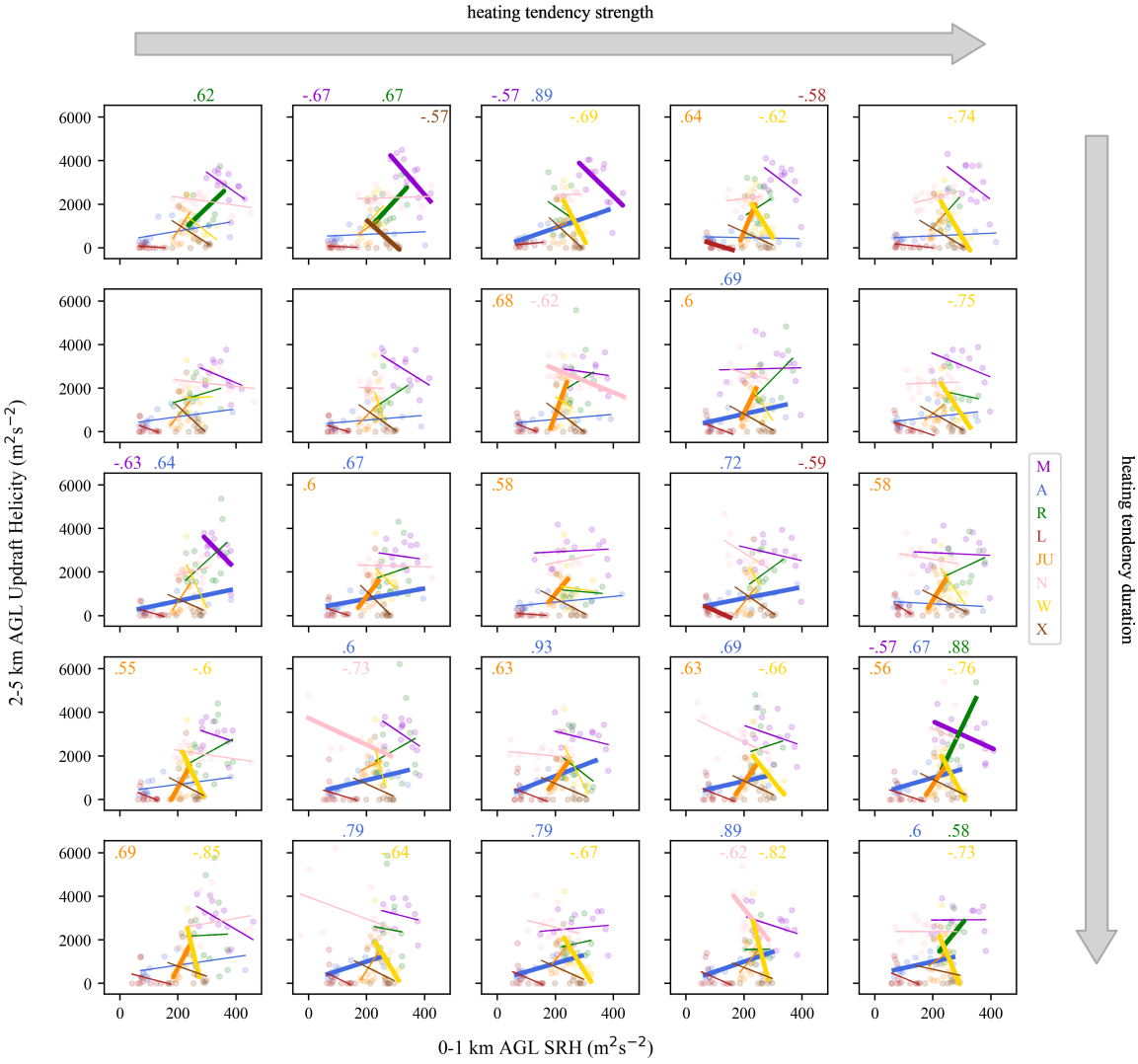

Figure 3.12: As in Figure 3.10, except lines of best fit are shown for each individual storm. Additionally, statistical significance ($p < .05$) is displayed with thicker lines of best fit and corresponding correlation coefficients at the top of each panel.

The unsuccessful suites have more consistent significant, positive relationships between mid-level mesocyclone strength and our representative thermodynamic parameter, MLCAPE. This, again, is unsurprising as all of the environments featured decreasing CAPE over time (Figure 3.6) and the ensembles in these suites were weakening

for most of the early evolution period following the cessation of the heating tendency. The majority of the ensembles for successful suites exhibit insignificant relationships between the two quantities with weakly negative or no correlations. An exception to this is supercell R, that appears to have significant positive relationships in the weaker CI regimes and significant negative relationships in the stronger CI regimes.

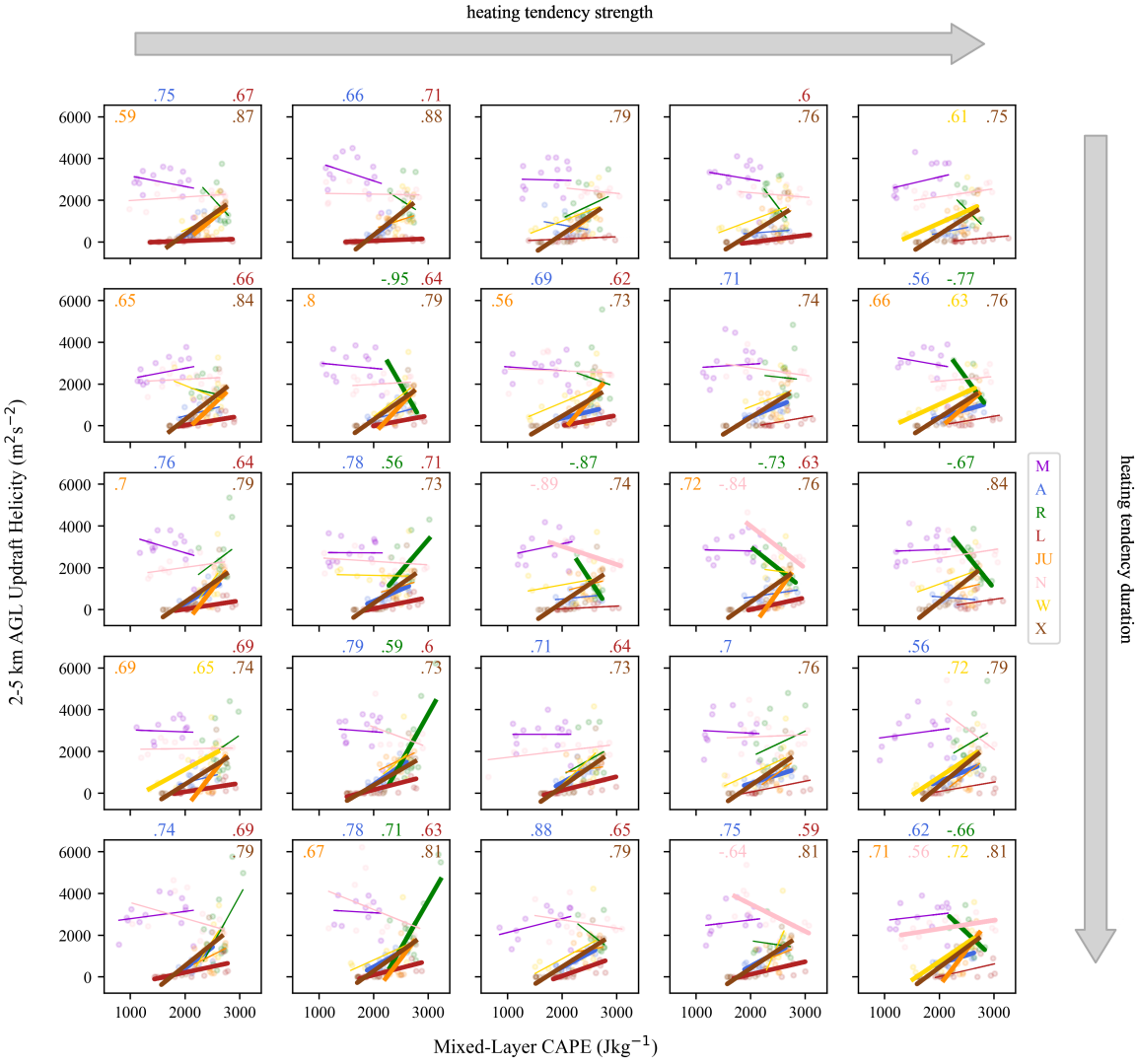

Figure 3.13: As in Figure 3.12, except for 2-5 km AGL UH and MLCAPE.

Chapter 4

Simulated vs. Observed Evolution

So far, a "successful simulation" was defined in terms of developing and sustaining deep convection. We can take this one step further and determine if any of the successful simulations were also realistic by comparing simulated vertical vorticity to observed low and mid-level AzShear. The relationship between simulated vertical vorticity and observed AzShear is not directly 1:1, but instead closer to 2:1 due to resolution differences of our model output and radar-derived observations. Despite this, we can assess if the two quantities (hereby called "rotation") exhibit similar trends by analyzing time series of their differences during the early evolution period.

Ensembles from the three unsuccessful suites, L, JU, and X, all initially possess greater rotation than their observed counterparts (Figure 4.3), likely due to our imposed heating tendency and the immense low-level shear in their environments. However, over time both low- and mid-level simulated rotation either remains weak or diminishes while the observed storms strengthen (Figures 4.1, 4.2).

Supercells M and N have near-constant differences between simulated and observed rotation for the entire early evolution period. This implies that simulated convection generally followed the evolutionary trends of the observed supercells, in terms of both strength and timing, which can qualitatively be observed in Figures 4.1 and 4.2. Storm A follows suit for the first 200 min after CI, although its simulations fail to emulate the sharp increase in observed AzShear that follows. In contrast, supercell W's ensembles

significantly overestimate observed rotation early on, coinciding with the ongoing influence of the heating tendency. This artificially elevated peak quickly subsides, after which the ensembles maintain a constant amount of rotation (Figures 4.1, 4.2) and a near-constant difference from observed rotation (Figure 4.3). Lastly, Supercell R appears to be the least realistic of the successful simulations, with relatively large and variable discrepancies between observed and simulated rotation in both the low- and mid-levels throughout the analyzed period (Figure 4.3).

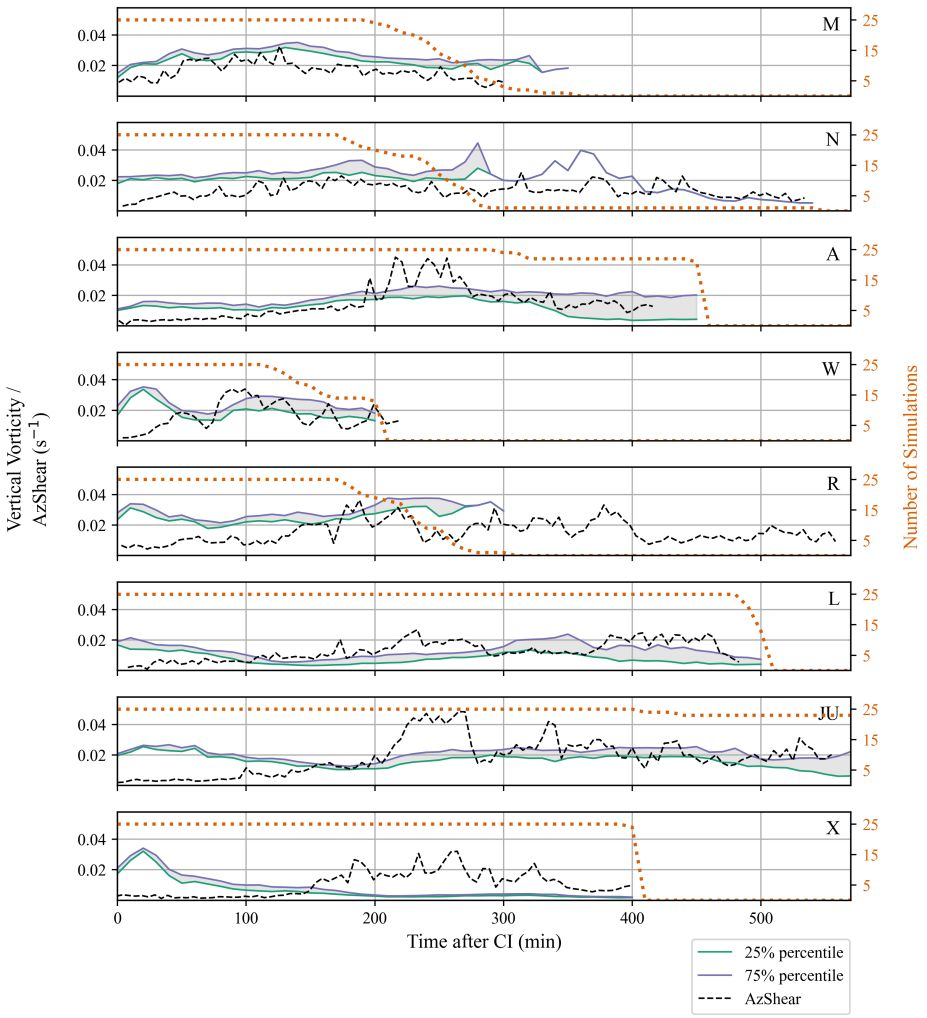

Figure 4.1: Time series of 25th percentile (green line), 75th percentile (purple line), and IQR (gray shading) for maximum vertical vorticity in the 10-m to 3-km AGL layer after CI for each storm's ensemble suite. The black dashed line is maximum observed low-level AzShear after CI. Each storm has a panel, and the panels are arranged by latitude of observed CI, so the northern-most initiating supercell is at the top and the southern-most at the bottom. The orange dashed line represents the number of ensemble members that have not experienced an unphysical reflectivity band merging with the main supercell.

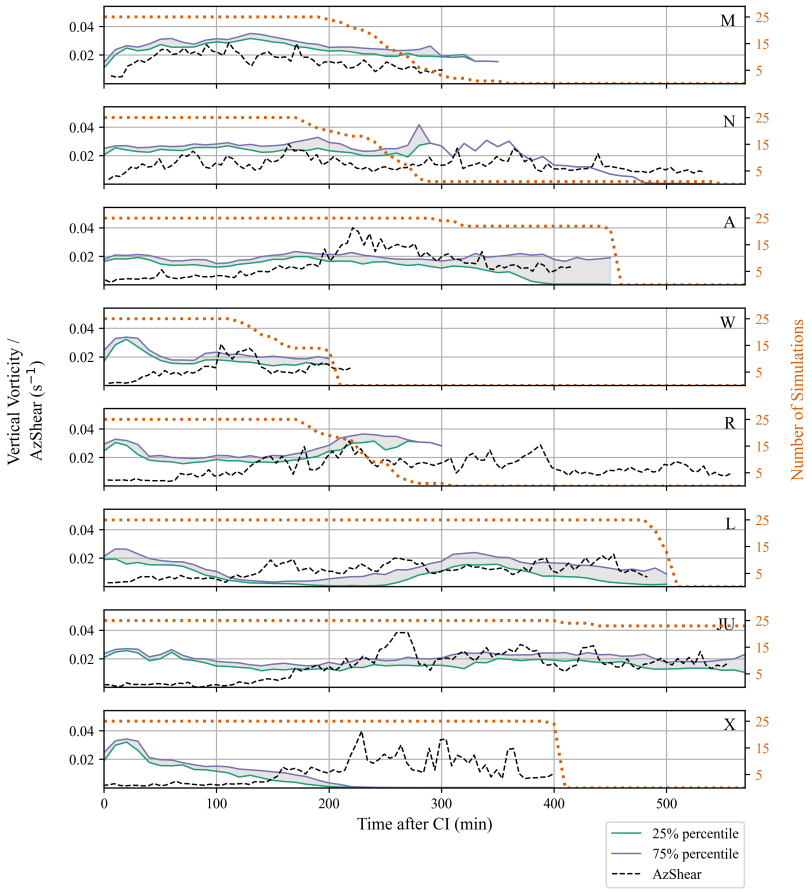

Figure 4.2: As in Figure 4.1, but for maximum vertical vorticity in the 3-km to 6-km AGL layer and mid-level AzShear.

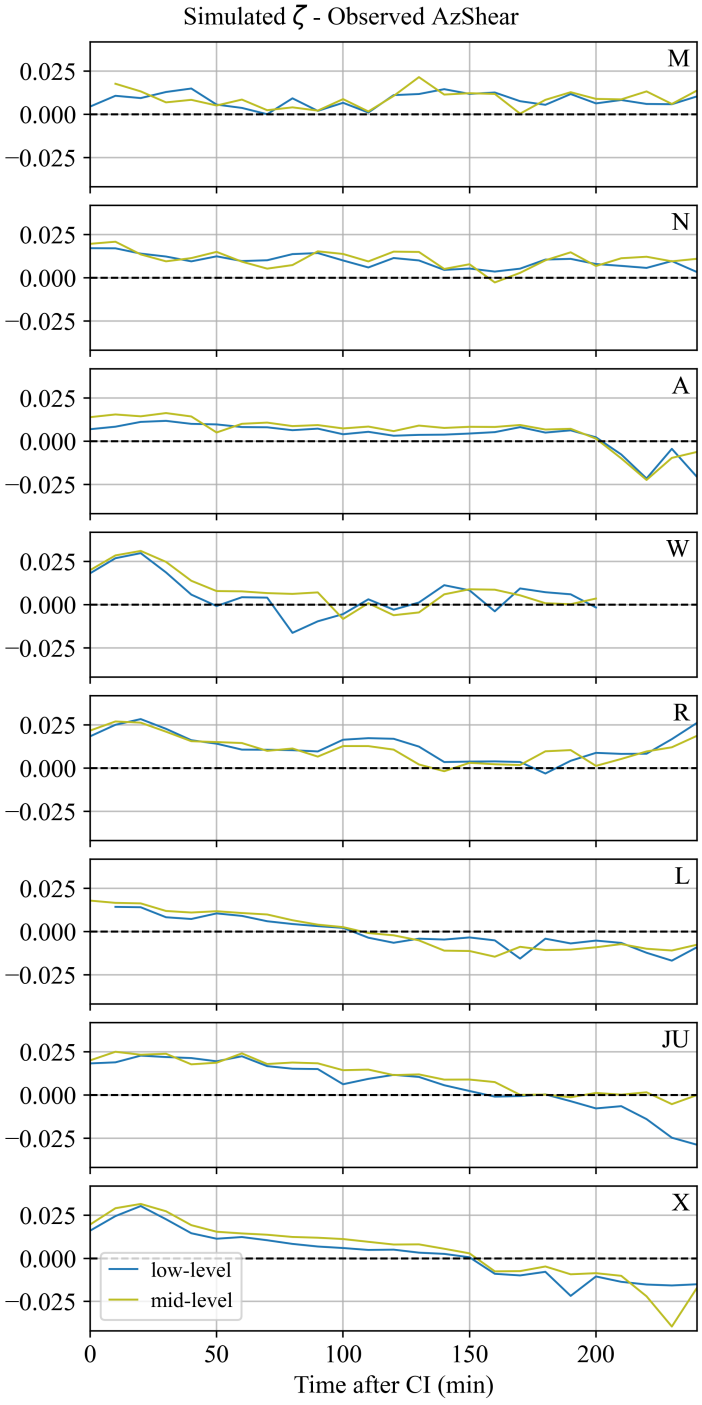

Figure 4.3: Differences between ensemble-median simulated vertical vorticity and observed AzShear values in the corresponding layers. Low-level (0–3-km AGL) ζ and AzShear are blue; mid-level (3–6-km AGL), olive.

The ensembles of supercells M and N are the most realistic of our successful suites in that they appropriately follow evolutionary trends in observed AzShear, but when comparing the magnitudes of simulated vertical vorticity and Azshear, their realism is less clear. As mentioned above, a perfectly realistic simulated storm would contain vertical vorticity around twice that of observed AzShear at every point in time. However, there is no clear linear trend between simulated and observed rotation for either storm suite in both the low- and mid-levels (Figures 4.4, 4.5).

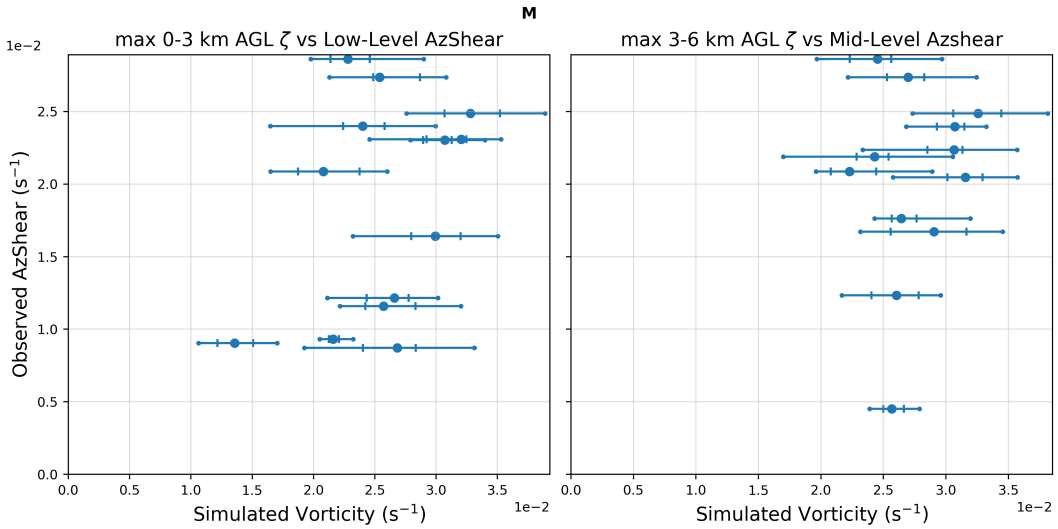

Figure 4.4: Observed maximum AzShear as a function of simulated maximum vertical vorticity in the low- (left) and mid-levels (right) for the ensemble suite of Supercell M. Large dots indicate ensemble median; small dots, ensemble minimum and maximum, connected by a horizontal line. The 25th and 75th percentiles are denoted by short vertical ticks.

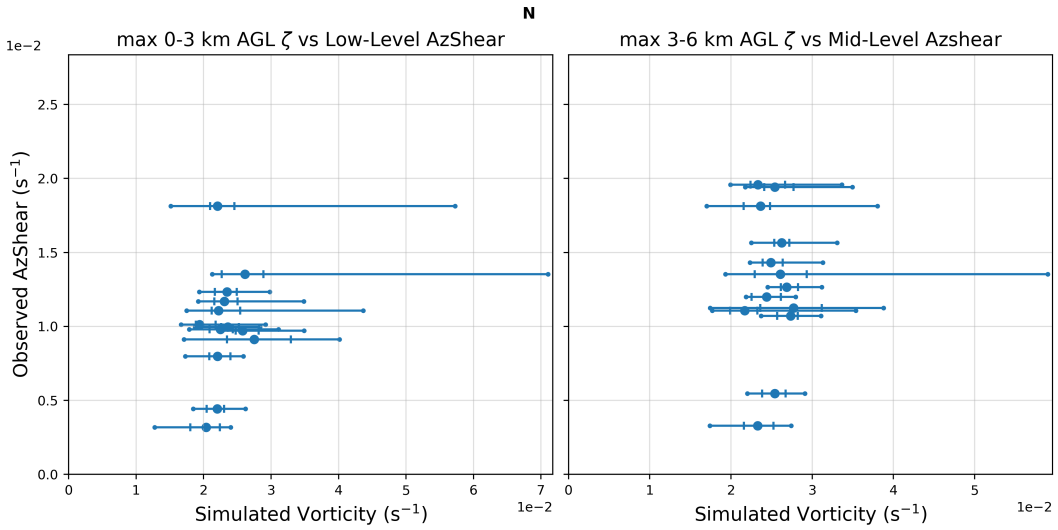

Figure 4.5: As in Figure 4.4, but for supercell N.

It is possible that the absence of a linear relationship between the magnitudes of observed and simulated rotation stems from observational limitations, as discussed in Chapter 6. Instead, we use their temporal derivatives to more definitively quantify patterns or trends shared by the two quantities Figure 4.6. Both supercells M and N exhibit moderately strong, statistically significant positive relationships between simulated and observed low-level rotation. Interestingly, storm X possesses a similar relationship, though this is attributed to a near-constant decrease in simulated rotation coinciding with a constant, unchanging observed rotation. The only other case with a statistically significant relationship in either the low- or mid-level is supercell JU, for which the relationship between observed and simulated low-level rotation is strongly negative. This outcome is expected, as the simulated ensembles consistently weaken towards the end of the early evolution period, while the observed supercell intensifies rapidly.

An important caveat for these statistically significant relationships is the small sample size for each supercell in each layer. After isolating the early evolution period

for each simulation suite and limiting persistence biases by removing every other time step, only 13 data points remain per layer for each suite. As such, we cannot confidently claim that these significant relationships are not artifacts of random variation. The significance and strength of these relationships is further impacted by narrow ranges in either the observed or simulated rotation, like for Supercells A and L.

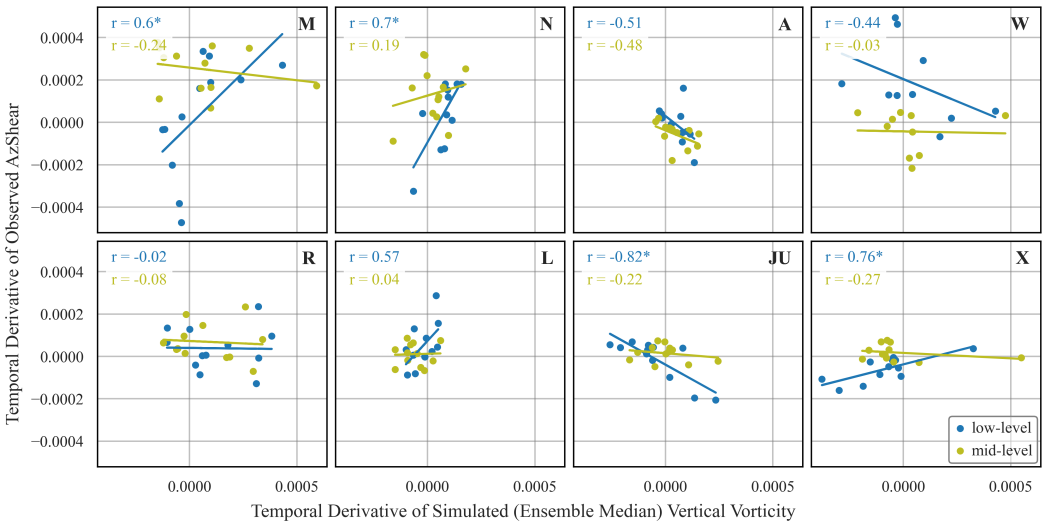

Figure 4.6: Temporal derivatives of observed AzShear plotted as a function of the temporal derivatives of simulated, ensemble-median vertical vorticity in the corresponding layers for each storm. Lines of best fit are also included, as well as correlation coefficients between the parameters and indications of statistical significance ($p < .05$). The quantities were smoothed to reduce noise, and every other data point is used to reduce persistence biases.

Chapter 5

Observed Evolution

The main focus of this project is the eight ensemble suites of simulated supercells in observed background environments. Deep convection was maintained in all of these observed environments, but some of the ensemble suites failed to do the same. A basic, qualitative analysis of the early evolutions of the observed storms can yield some information into mesoscale features and synoptic-scale influences that are responsible for sustained convection in environments that could not maintain simulated storms or produced unrealistic storms.

5.1 Supercell L

Supercell L initiated at 1915 UTC on 27 April in far eastern Louisiana (Figure 5.1a). It gradually strengthened over the next hour while tracking east-northeast, while supercells G and K merged to the northeast. Supercell L then began to weaken around 2028 UTC (Figure 5.1c), and until 2055 UTC, supercell L appeared to be dying. However, at 2100 UTC and outflow boundary visible in the radar reflectivity field from supercells G and K interacted with supercell L (Figure 5.1c,d). A surface station in Copiah County, Mississippi, maintained by the Bureau of Land Management and the Mississippi Forest Commission, observed the passage of this boundary between 2000 UTC and 2100 UTC and an attendant 2°C drop in temperature (Figure 5.2). This weak mesoscale boundary appeared to provide supercell L with the necessary lift to reintensify, as its

reflectivity field rebounded almost immediately. By 2132 UTC, supercell L became severe-warned, and then produced its first tornado at 2242 UTC.

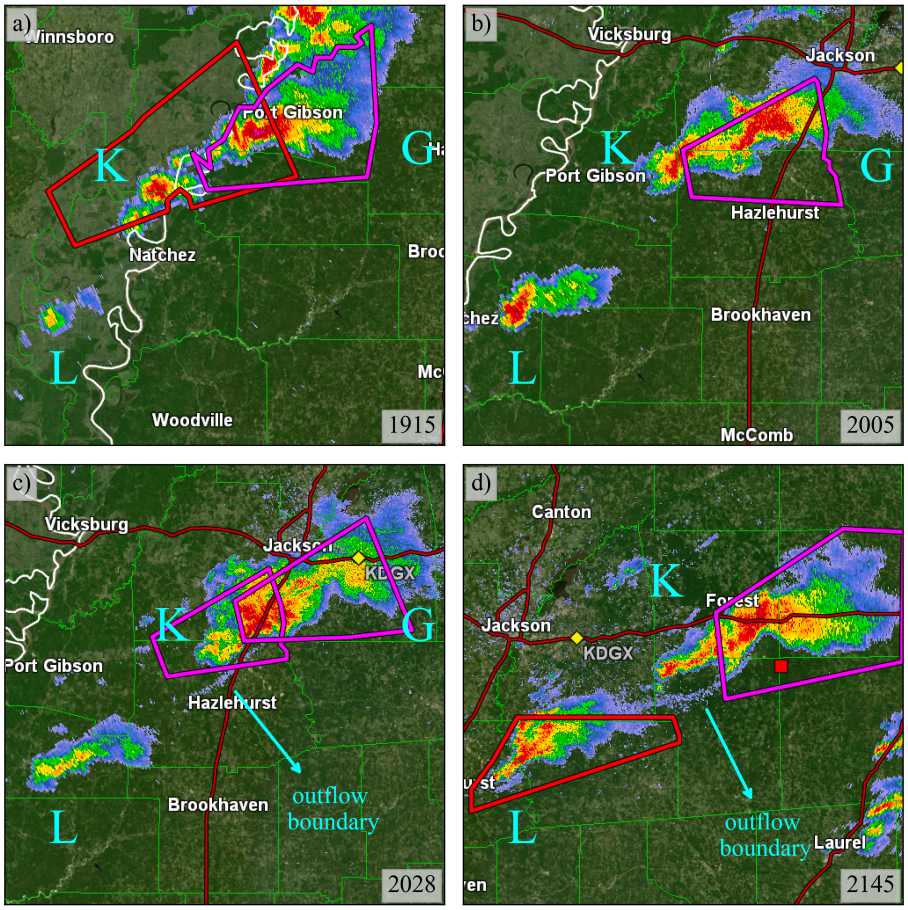

Figure 5.1: Nexrad level 2 reflectivity field at the lowest tilt at 1915, 2005, 2028, and 2145 UTC on 27 April 2011.

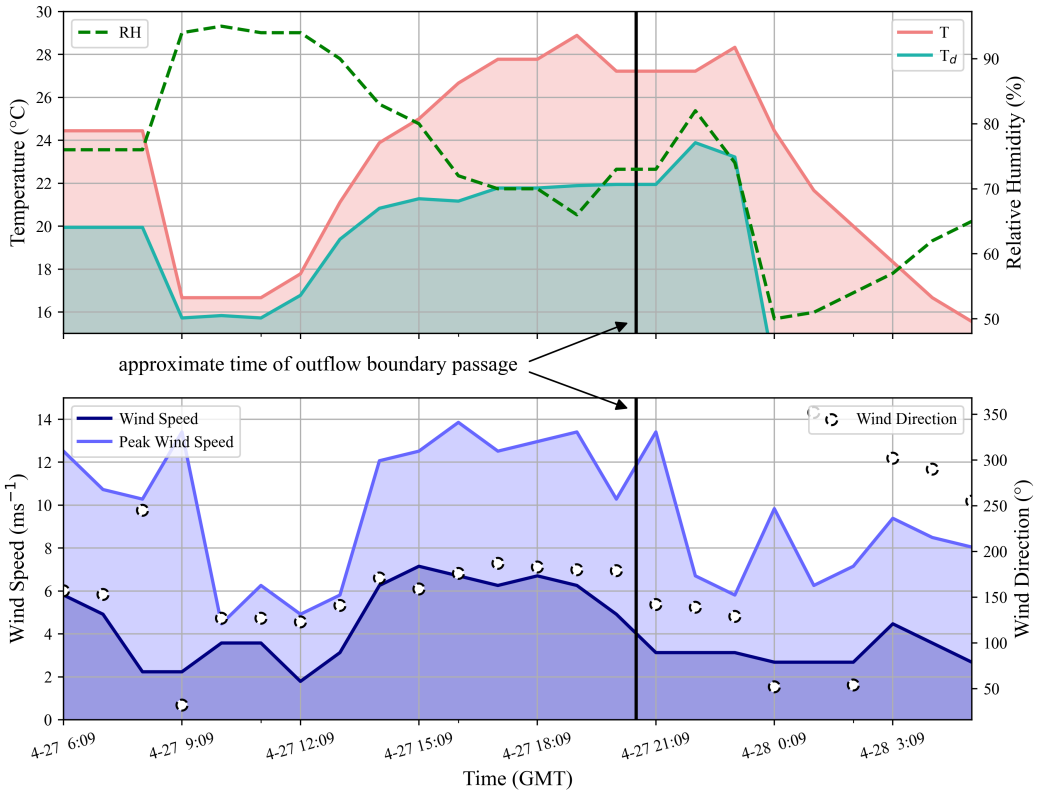

Figure 5.2: Meteogram from the CYSM6 surface station in Copiah County, MS. The top panel contains air temperature (red, °C), dew point temperature (cyan, °C), and relative humidity (%, green dashed line). The bottom panel displays wind speed (m s^{-1}, dark blue), peak wind speed (m s^{-1}, light blue), and wind direction (white and black dots). The approximate time that the outflow boundary passed over the station (2030 UTC) is denoted by the vertical black line in both panels.

Both the observed and simulated supercell L struggled to sustain convection shortly after CI. However, their evolutions began to diverge due to the effects of supercells G and K. It is probable that, without the outflow boundary to provide additional lift, the observed supercell L would have dissipated like its simulated counterpart. Supercells G

and K may have also contributed to the observed supercell L's maintenance by priming the environment with moisture ahead of supercell L. The base-state soundings used in this project are taken in the inflow region of the supercell (as it is depicted by RUC profiles and surface observations), and in this case it can be assumed that they are drier than the environment supercell L encountered.

5.2 Supercells W and X

Supercell X initiated at 2355 UTC on 27 April in the southern portion of a confluence band stretching from northeast to south-central Alabama (Figure 5.3a). The storm took several hours to strengthen and organize in this band, and was accompanied by many other areas of weak convection (Figure 5.3b,c). It was not severe-warned until 0321 UTC on 28 April, over 2 h after CI. Further north, Supercell W initiated in the same confluence band five minutes earlier at 2350 UTC (Figure 5.3a) and developed much more rapidly, producing a violent tornado just over an hour later at 0112 UTC.

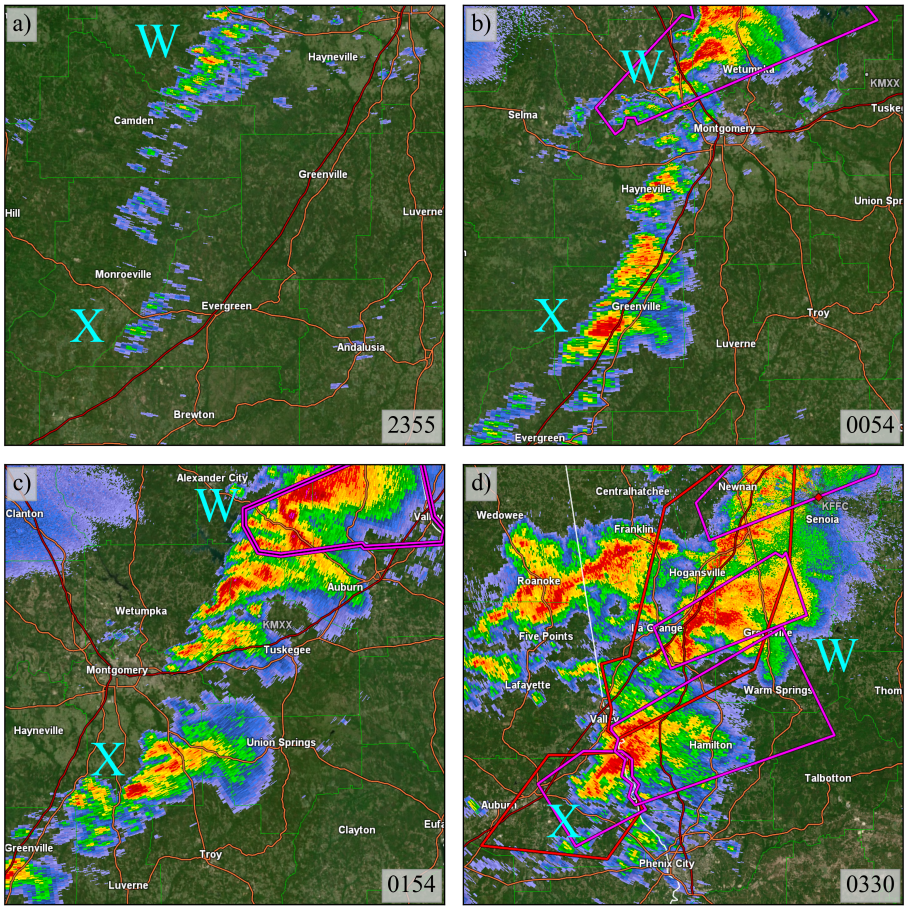

Figure 5.3: Nexrad level 2 reflectivity field at the lowest tilt at 2355, 0054, 0154, and 0330 UTC on 27-28 April 2011.

Our tendency nudging initiation mechanism is designed to gradually induce updrafts, but the slower development of Supercell X in a diffuse area of weak forcing is not well-represented by our heating tendency, which occurs in a single focused area at the center of the model domain. Supercell W was positioned further north, closer to the synoptic-scale low pressure system an thus residing in a region of greater synoptic-scale forcing for ascent. With additional forcing, it was able to develop much faster than Supercell X, despite existing in a otherwise similar background environment.

5.3 Supercell J

Supercell J experienced a combination of the mesoscale influences similar to those that sustained Supercells L and X. Like Supercell X, it developed in a narrow confluence band at 1823 UTC on 27 April (Figure 5.4a). Like supercell L, it was positioned just southwest of another supercell, in this case supercell H (Figure 5.4b,c,d). Although no outflow boundary from supercell H is visible in radar-derived reflectivity fields, both supercells L and H initiated in environments with relative humidity at the surface below 75%. Thus, it can reasonably be assumed that some rain-cooled air emanated from Supercell H and provided additional lift for Supercell J. As time progressed, J continued to strengthen as it followed Supercell H, and ultimately produced its first tornado at 2143 UTC.

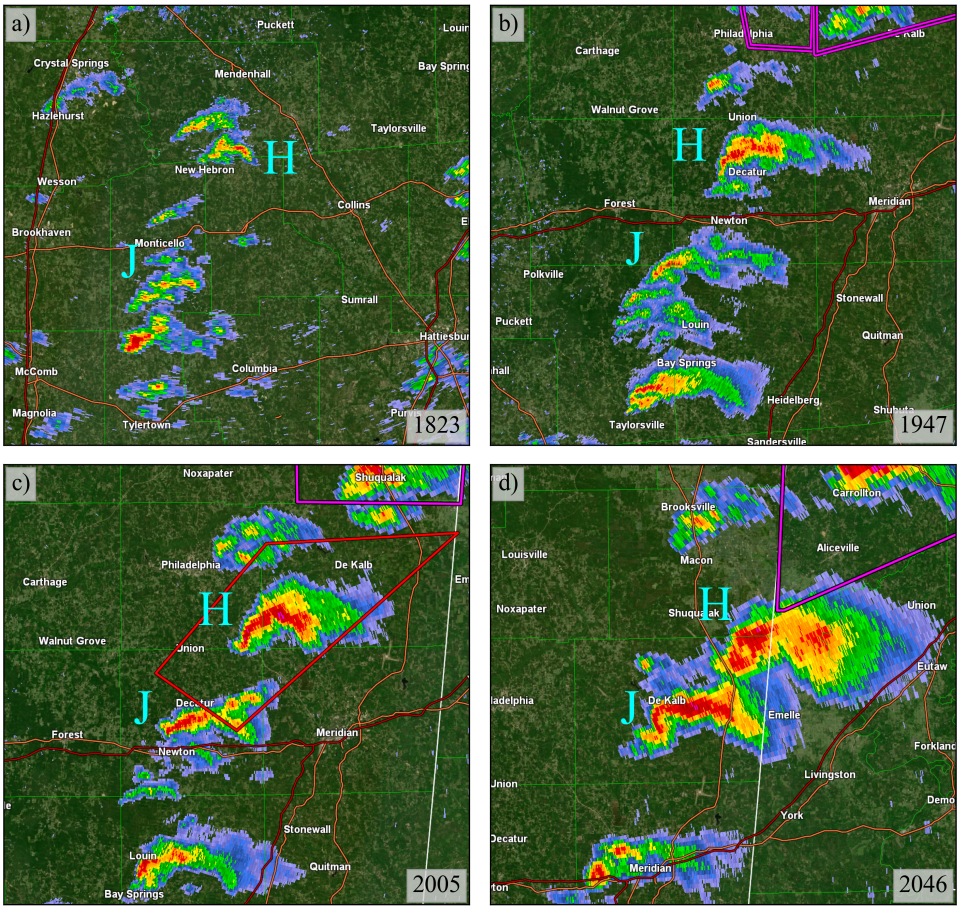

Figure 5.4: Nexrad level 2 reflectivity field at the lowest tilt at 1823, 1947, 2005, and 2046 UTC on 27 April 2011.

5.4 Supercells M and N

Much like supercells W and X, M and N initiated within 10 min of each other at 1917 UTC and 1924 UTC, respectively (Figure 5.5a,b). Supercell M developed very rapidly, displaying a velocity couplet in its "pre-convective" showers (reflectivity below 40 dBZ). Just 48 min after CI, supercell M produced an EF5 tornado. This tornado production was immediately preceded by the envelopment of a non-tornadic supercell

on the supercell's rear flank (Figure 5.5c,d). While rear-flank mergers produce a variety of outcomes, the involvement of a less-mature storm leads to the formation of a more-classic supercell (Hastings and Richardson 2016), as was the case for supercell M. Additionally, stronger mesocyclones and greater baroclinically-generated vertical vorticity tend to follow rear-flank mergers (Rogers and Weiss 2008; Hastings et al. 2014; Hastings and Richardson 2016), which could explain the rapid tornado production follow supercell M's merger. As for the rapid intensification of the parent supercell before the merger, idealized numerical simulations suggest that supercells located southeast of nearby secondary supercell (within 50 km, as was the case for storm M) reside within a region of augmented 0–500-m SRH induced by the neighboring storm, slightly strengthening the parent supercell's circulation and increasing its potential for vertical vorticity stretching (Werkema 2022).

Meanwhile, just to the southwest, supercell N was bombarded with merging cells in its forward flank. Ancillary cells located ahead of a parent cell's updraft in a storm's inflow region can reduce near-surface buoyancy and vorticity stretching, decreasing tornado production (Rogers and Weiss 2008). The prolific and continuous merging of weak, non-supercellular storms in supercell N's forward flank could be a reason why it produced weaker tornadoes (maximum EF1 strength), while just to the northeast supercell M produced a much more violent, long-lived tornado. Another possibility is the mutual interaction between supercells M and N, as they were approximately 50 km apart 1 h after their respective CIs.

These mergers are another mesoscale feature not present in the simulations. The effect of cell mergers on mesocyclone strength is generally thought to be obscured by stochasticity in a storm's environment (Fischer et al. 2023). In these two simulation suites, their absence did not prevent the simulations from sustaining realistic storms.

Instead, they likely impacted the tornado production of the observed supercells (Lyza and Flournoy 2023), which these simulations are too spatially coarse to resolve.

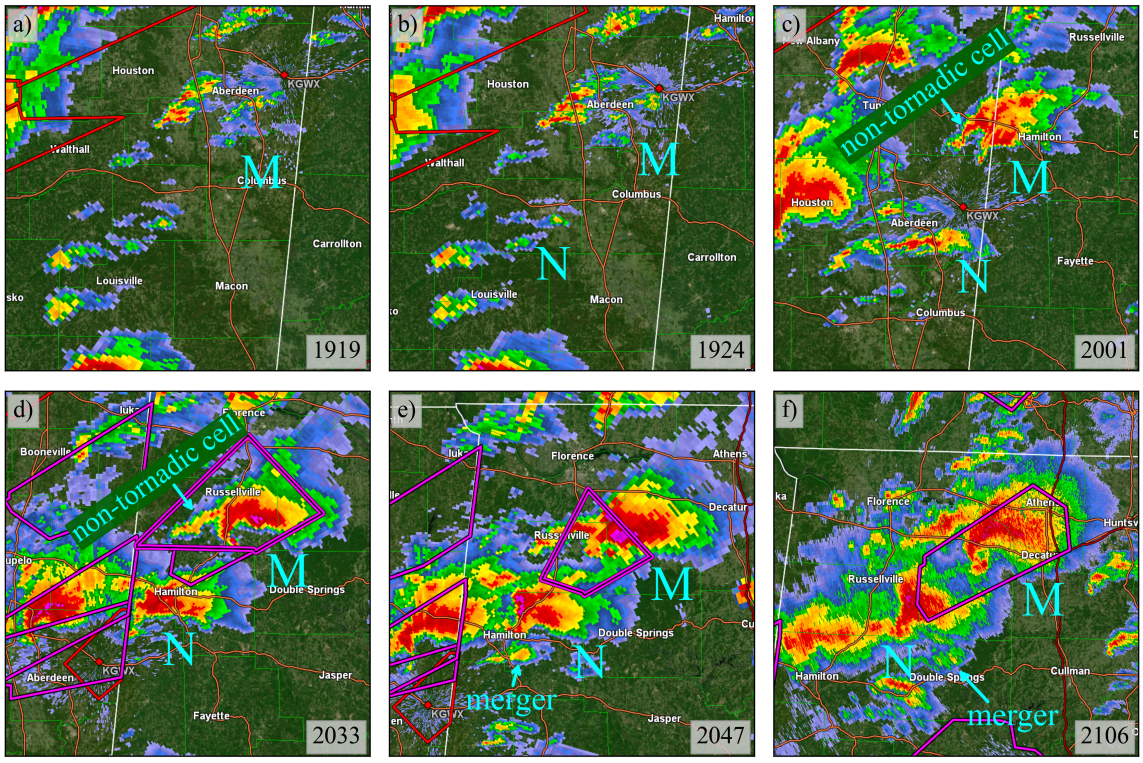

Figure 5.5: Nexrad level 2 reflectivity field at the lowest tilt at 1919, 1924, 2001, 2033, 2047, and 2106 UTC on 27 April 2011.

Chapter 6

Discussion

Bulk statistics from the ensemble suites indicate that the simulations of observed storms initiating at higher latitudes more successfully maintained deep convection, whereas those of more southern-initiating storms struggled or failed to do the same. The higher-latitude storms existed in closer proximity to the residual thermal boundary from earlier QLCS activity. Although the boundary is not explicitly resolved in our simulations, the associated elongated hodographs and enhanced vertical wind shear, especially in the lower levels, are evident in the base-state hodographs. In contrast, the simulations that failed to sustain organized convection featured comparatively less curvature in their low-level wind profiles. The environments of the observed southern-initiating storms eventually obtained greater shear due to the strengthening LLJ and their closer proximity to the remnant thermal boundary, but by this point simulated convection in their ensembles was weak or nonexistent.

The successful suites generally exhibited a more gradual development, taking longer to form strong mesocyclones. In contrast, the unsuccessful suites formed rapidly. As they existed in generally weaker shear, this follows the findings of Lawson (2019) in that lower-shear environments tend to support quicker storm evolutions. However, they could not maintain these intensities after the heating tendency subsided. Early environments of the more successful suites also tended to be more humid though the entire depth of the troposphere, particularly in the mid- and upper levels. They also contained local minima in wind shear coinciding with the driest layers aloft, mitigating

the effects of entrainment on the developing updrafts. Combined with stronger low-level shear and enhanced SRH, this allowed more robust updrafts to form.

Several factors could have contributed to the evolution of rapidly developing but ultimately failing simulation suites. One possibility is decreased moisture content through the depth of their environmental profiles. Initially, our heating tendency forced strong updrafts with downdrafts diluted by their dry mid-level environments and weaker resulting outflow. However, the presence of stronger shear in the driest portions of the ambient troposphere promoted locally increased entrainment that eroded updraft strength. Concurrently, the relatively lower overall vertical shear in their environments favored increased precipitation loading in the downdrafts and stronger outflows that became disconnected with the storm's mesocyclone in time, leading to storm demise as noted by Gilmore and Wicker (1998).

Dry air entrainment aloft has the most detrimental effects on supercell updrafts in environments with less CAPE (James and Markowski 2010). All of the supercells included in this study existed in an extreme parameter space with significant convective instability available, so this would suggest that suites in relatively drier environments should have been able to sustain convection. While the rotating nature of supercell updrafts does not make them immune to environmental or turbulent entrainment, the width of the updraft can make a storm more susceptible to the mixing in of ambient dry air (Peters et al. 2020). Updraft width is not explicitly calculated in this study, but environments with lower LCL heights support wider updrafts due to less entrainment below cloud base. Thus, we can assume that the more humid low-level environments with lower dewpoint depressions at the surface will have these lower LCL heights and wider updrafts. Similarly, the drier low-level environments, a characteristic of our unsuccessful suites, would produce higher cloud bases and narrower updrafts more susceptible to the detrimental effects of entrainment aloft.

Another possibility is the amount of heat introduced to the system through tendency nudging was too great for the unsuccessful suites. Almost all of our suites displayed artificial intensity peaks while the heating tendency was ongoing. The distinguishing factor was whether these suites' ensembles could recover following the associated weakening period, or if convection could not be supported without synthetic forcing. These suites contained greater variability among their ensemble members than the two most successful suites, which did not encounter any artificial peaks in mesocyclone strength around the time of CI. Part of this is to be expected, as different CI regimes will produce different storms that will recover and maintain a weaker intensity at different rates. This also suggests that storm outcomes in these environments were more dependent on CI characteristics, and alternate heating tendency magnitudes, durations, elevations, and sizes could produce different results. This yields an interesting question for the suites of supercells M and N, which displayed the least ensemble spread of the successful simulations. Were their environments supportive of organized, intense convection regardless of CI characteristics, or is the considerably narrow range of heating tendencies included in this study ideal for these environments? The observed supercells formed much quicker than many other storms present in this study, both producing their first tornadoes 48 min and 149 min after CI, respectively. In terms of their simulated success and relative realism, the environments of storms M and N might have benefited from the strong forcing provided by our heating tendencies as it more closely emulated the CI of the observed supercells. This is especially true for the observed supercell M, which displayed a couplet in radar-derived velocity field (Figure 6.1) before accomplishing CI as defined herein.

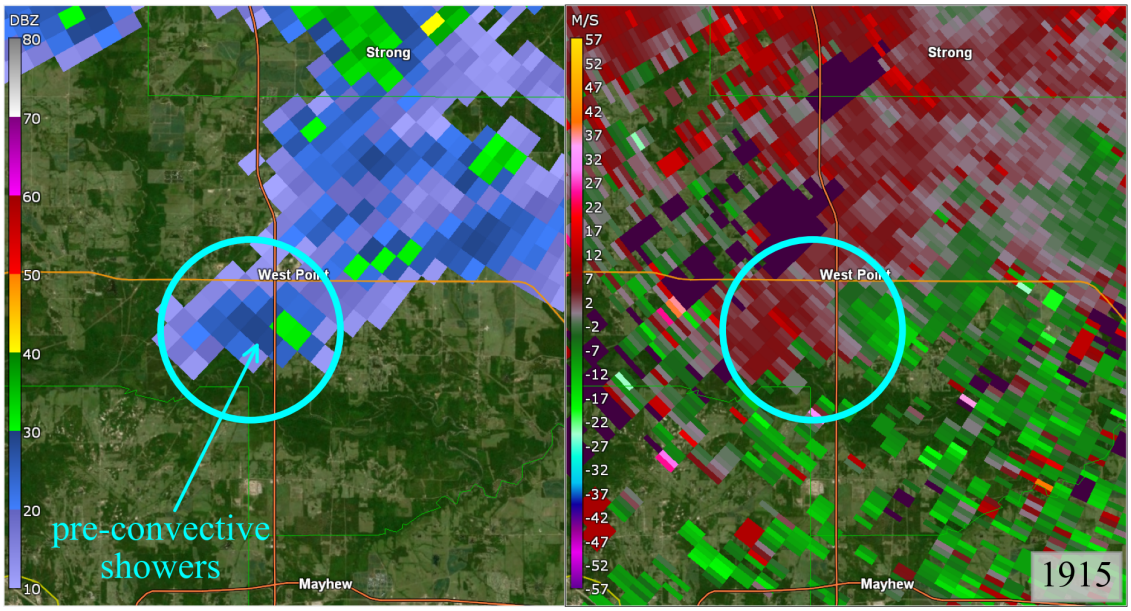

Figure 6.1: Velocity couplet in the pre-convective showers of supercell M, as seen at 1915 UTC by KDGX at the lowest tilt.

When considering all eight ensemble suites, a consistent trend emerges in which ambient kinematic parameters influence simulated mesocyclone strength. Deep-layer bulk shear was used as an example for this, but the same trend persists at varying degrees for all kinematic predictors included in this study. Meanwhile, thermodynamic characteristics of the model environments did appear to exert a direct influence on mesocyclone evolution. These two patterns hold true across all CI regimes and are especially evident for kinematic environmental influences in lower magnitude, shorter duration heating tendency regimes. Given that our simulations emulate tornadic supercells, these findings align with Schneider and Dean (2008) in that tornadic supercells are more modulated by deep-layer shear than CAPE.

When these CI regime-wide trends are decomposed into contributions from each storm's suite, it appears that the successful suites all have small, negative correlations

with 0–1-km SRH and other kinematic parameters (included in Appendix 1). However, these cases generally exist in higher ranges of the parameter, indicating that decreasing SRH values do not reside in an unsupportive SRH regime, and should not be considered unfavorable. In contrast, the unsuccessful suites do not show similar trends between mesocyclone strength and kinematic parameters, although the longer-duration CI regimes of storm JU's suite do contain positive correlations between simulated mesocyclone strength and low-level SRH. The unsuccessful suites also display more positive relationships for thermodynamic parameters like MLCAPE across their CI regimes. However, this is likely due to the combination of weakening convection and environmental CAPE reduction over time and does not depict a causal relationship. The only successful suite that appears to have trends with MLCAPE is that of storm R, where mesocyclone strength increases with environmental MLCAPE in the lower magnitude CI regimes. This reverses for the stronger magnitude CI regimes, with a negative relationship between the two quantities.

When evaluating the realism of our ensemble suites, we treated low- and mid-level AzShear as a true depiction of observed storm strength. However, this ignores the inherent range dependence of the radar-derived quantity. As demonstrated by L22, the ability of AzShear to discriminate between weak and strong tornado intensities diminishes with increasing distance from the nearest radar. This limitation is particularly relevent for the event herein, in which multiple WSR-88D radars malfunctioned. This included a fiber-optic communications failure for KHTX in northeast Alabama (Hayes 2011), meaning many tornadic supercells (including some in this study) were sampled by remote radars and AzShear values were appreciably affected.

As 0–3-km AGL UH is a sufficient proxy for tornado production (Sobash et al. 2016a,b), a similar relationship is likely present for mesocyclone strength, especially in the lower levels. In our simulations, UH can be calculated at every grid point and is not

subject to observation limitations such as radar range. Therefore, a direct comparison of specific magnitudes of UH and AzShear is inherently unreliable and doing so to estimate the accuracy of our simulations is ineffective.

Instead, we can estimate the realistic nature of our simulation suites by comparing if simulated low- and mid- level vertical vorticity follow the same temporal trends as Azshear in the appropriate layers. This was done by evaluating timeseries of the two quantities and comparing their temporal derivatives. While these methods does not completely eliminate the effects of AzShear range-dependence, which remains an unavoidable caveat, they do reduce the impacts of individually inaccurate AzShear values and noise in the observed quantity. This revealed that the ensemble suites of supercells M and N most accurately captured the evolutionary trends of their observed counterparts. Although the suite of storm A struggled to sustain strong, deep convection, it replicated observed evolutionary trends moderately well despite missing a large observed maxima in AzShear. The suites of supercells W and R were less able to follow their observed evolutionary trends, although supercell W seemed to recover later in the early evolution period. These performances appear to be somewhat modulated by environmental shear, as the environments of supercells M and N contained the greatest low-level and deep-layer shear while those of supercells R and W contained the least. Additionally, storm A's environment contained substantially less low-level SRH than the other successful suites, so it is not surprising that the simulated ensembles never experienced a large increase in rotation.

It is important to note that the two most realistic simulation suites, of storms M and N, passed in the closest proximity to the KHTX radar that experienced a communications failure as described above. Fortunately, this did not occur until around 3 hours after observed CI for both supercells, so the majority of our early evolution analysis would be unaffected by the outage.

Qualitative observational analysis of the supercells included in this study found a number of mesoscale interactions not present in our simulations. These features unquestionably impacted the morphology and tornado potential of the observed supercells, but the results of this study suggest there are varying degrees to which they impacted mesocyclone strength and storm outcomes. For example, supercells M and N both experienced cell mergers, but were also the most realistically modeled by our combined tendency nudging and base-state substitution simulation approach. The resulting tornado production of the two supercells is not relevant to the study herein other than presumably stronger low-level mesocyclones, but the dearth of cell mergers in our simulations did not prevent the formation of robust supercells that matched the evolutionary trends of observed low- and mid-level AzShear. Meanwhile, the failure of supercell L's environment to sustain convection regardless of the CI regime and the apparent decay of the observed supercell before interacting with an outflow boundary suggest that the environment itself was not supportive of long-lived supercells and violent tornadoes. Similar conclusions can be drawn for the environments of supercells JU and X, although it is pertinent to consider if CI characteristics that better model the confluence bands in which the observed storms formed would produce different simulated storm outcomes.

6.1 Regional Comparisons

6.1.1 Boundary Zone: M and N

The residual thermal boundary itself is not included in our simulations, as CM1 employs a horizontally homogeneous environment to isolate desired properties and reduce complex spatial variations (Letkewicz et al. 2013). However, variations in cloud cover

on either side of the boundary induced a thermally-direct circulation that produced locally increased deep-layer shear. This is evident in the wind profiles of supercells M and N compared to storms from other regions, as they contain significantly stronger low-level winds and greater overall vertical wind shear. It is possible that this characteristic of their environments perpetuated the continuing intensification of their respective ensemble simulations after the cessation of the heating tendency, as the downdrafts were likely far removed from the updrafts. In combination with such large values of SRH, this allowed for the almost immediate development of robust, rotating updrafts.

Within the boundary zone, M and N existed in close proximity to each other and in very similar observed environments. However, there are large deviations in their simulated kinematic environments early on in their respective simulation suites. As the deviations are maintained through successive base-state substitutions, they are probably attributable to storm-induced environmental changes within the simulated domain. In a median sense, the ensemble supercells of M produced large storm-induced modifications on their kinematic environment, markedly in an almost 10-m s^{-1} (20-kt) increase in deep-layer shear. This likely contributed to the differences in their mesocyclone evolutions, as greater overall and low-level shear allowed the M ensembles to rapidly develop a mesocyclone in the low–mid-levels. Supercell N's ensembles existed in environments with less, albeit sufficient, low-level shear, and displayed a more typical mesocyclone development. These simulated mesocyclone evolutions qualitatively align with their respective observed storms, with supercell M intensifying rapidly while supercell N more gradually developed. When considering low-level mesocyclone strength as a proxy for tornado potential, the same trends emerge. Supercell M produced a violent, EF5 tornado within 1 h of CI, and its simulated ensembles similarly exhibited strong near-surface mesocyclones in that time frame. Supercell N produced weaker

(EF0–EF1) tornadoes more than 2 h after CI, and its simulations similarly required several hours to develop stronger low-level mesocyclones.

It is important to consider the interdependent relationship of low-level shear and updraft/mesocyclone strength in the context of supercell M. Generally, it is understood that environments with elongated hodographs and greater shear in the lower troposphere will support stronger updrafts. However, in close proximity to the storm (and depending on the orientation of the background flow), these updrafts can induce greater curvature on low-level winds and thus increased low-level shear. Without more in-depth analysis, it is not possible to determine whether greater environmental shear led to a stronger mesocyclone, or a stronger mesocyclone induced large kinematic modifications on its simulated environment. Regardless, such analysis is beyond the scope of this project.

6.1.2 Louisiana Delta: A and L

The Louisiana Delta region produced the least successful pair of simulation suites. Supercell A's ensembles sustained weak convection for the duration of the simulation time, while no ensembles of supercell L maintained convection after the cessation of tendency nudging. Both of these storms' environments were dry throughout their vertical profiles, with perhaps the most impactful difference being the greater saturation around 1 km AGL for supercell A. Given the marginally greater MLCAPE present in supercell L's environment early on, it is probable that the supercell A's more humid low-level environment allowed it to sustain simulated convection. This is especially likely when considering the observed supercell L was weakening just like its simulated suite until encountering the outflow boundary produced by supercells K and G. This boundary not only provided greater surface convergence and lift, but also a more humid low-level environment.

6.1.3 Warm Sector Zone 1: R and JU

So far moisture content has been identified as a key differentiator between the successful and unsuccessful ensemble suites. The same argument can be made for the different simulated evolutions of supercells R and JU, as the environment of supercell R was substantially more humid with the exception of similarly dry mid-tropospheric layers. In this layer, supercell R's kinematic profile showed a clear minima in vertical wind shear, signifying the storm was not subject to strong entrainment in any layer, even the driest layer. The importance of ambient environmental moisture is highlighted by the enhanced CAPE in supercell JU's environment, as the presence of greater instability could not overcome dry air mixing into the updraft.

The evolution of supercell R's ensembles is especially interesting in the context of the tornado production of its observed counterpart. L22 provides an in-depth analysis of a long dormant period in tornado production, despite AzShear values indicative of an ongoing, violent tornado. This dormant period began just under 4 h after CI, at which time bulk statistics of supercell R's ensembles show a rapid increase in mesocyclone strength and vertical vorticity (see Appendix 1). This corresponds with a large increase in 5–7-km lapse rates in supercell R's environment, following the findings of Parker (2012). The notable difference in the observed supercell is worthy of future investigation.

6.1.4 Warm Sector Zone 2: W and X

A comparison of common forecasting parameters in the environments of supercells W and X reveals nearly identical conditions favorable for supercellular convection. The early evolutions of the simulated storms were similarly comparable, with supercell W exhibiting rapid development akin to the unsuccessful suites. Despite these initial

similarities, their ensemble suites produced antithetical storm outcomes. Both environments contained collocated relative humidity minima and shear maxima. This feature is especially obvious for supercell W. As previously discussed, this weakens the storms' updrafts through enhanced entrainment in those layers. However, it is unlikely to account for storm demise for supercell X since convection persisted across all ensembles of supercell W. Instead, it might have constrained the maximum strength that the simulated updrafts could achieve.

The consequential difference in these two simulated environments likely lies in their respective moisture profiles. In their first and second base-state environments, supercell X's environment is more saturated below cloud base, yielding LCL heights below 100 m compared to 311 m and 246 m for supercell W. Humidity below cloud base is slightly modified for the simulated environment of supercell W, as it is nearly saturated around 1 km AGL. Supercell X's simulated environment still contains lower LCL heights (179.6 m vs 300.6 m) due to the greater saturation at the lowest grid levels. This would imply that supercell X's ensembles would have wider updrafts that are better able to withstand the effects of entrainment. However, supercell X's environment is substantially less humid from 6–13 km AGL, and the slightly broader updrafts of its simulated storms are not able to endure the mixing of dry air through such a deep layer, leading to storm demise.

Additional consideration must be given to the type of CI used in these environments. Both of these observed supercells formed in a confluence band, and as discussed previously our heating tendency does not accurately model such forcing. However, supercell W former further north along the confluence band, closer to the surface low-pressure system and the region favoring synoptic-scale ascent. As it is a larger-scale feature, this additional forcing is not included in our simulations. However, the amount of forcing provided by our heating tendencies likely better emulate the combined synoptic and

mesoscale forcing that the observed supercell experienced, potentially contributing to the sustained convection in our ensemble suite of supercell W.

Chapter 7

Conclusions

This thesis sought to uncover the role of the background environment on tornadic supercell evolution on 27 April 2011 with quasi-realistic simulations. Eight of the 29 tornadic supercells from this event were selected based on the spatiotemporal region in which they formed and the time it took them to produce their first tornado. Simulations were generated with CM1, ignoring the effects of topography, storm-interactions, and horizontal environmental homogeneity. Temporal heterogeneity is achieved through bases-state substitution, in which the supercells' observed environments, represented by SFCOA profiles from the inflow regions, were continually implemented into the model environment. Convection was initiated with tendency nudging in an attempt to create a gradual, perhaps more realistic mesocyclone development. The magnitude and duration of the heating tendency was varied, creating 25-member ensemble suites for each selected supercell.

The majority of the analysis focused on the 4-h long early evolution period of the simulated convection, as by this point all observed supercells had produced their first tornado. Additionally, doing so reduces the effects of linear bands of reflectivity that formed in some ensembles as an unphysical manifestation of a realistic supercell environment. The eight suites of simulations were separated into successful and unsuccessful groups, based on their ability to sustain deep convection, and the successful group was further compared to low- and mid-level MYRORSS AzShear timeseries of the corresponding observed supercells to evaluate the realism of the simulated storms.

The key findings of this thesis are as follows:

- The ensemble suites fell into two categories: successful suites (M, N, A, R, W) that maintained deep convection at varying intensities, and unsuccessful suites (L, JU, X) that failed to sustain deep convection after the heating tendencies subsided.

- The three observed storms that could not be successfully emulated in simulations were the three most southern-initiating storms included in this study, while the observed storm's with corresponding successful simulation suites initiated further north.

- The successful suites experienced relatively gradual developments in the first hour of the simulations, taking longer to develop robust updrafts and mesocyclones. Alternatively, storms in the unsuccessful suites formed much more rapidly.

- There was less variability in storm intensities between ensembles in the successful suites, especially for supercells M and N. Suites that failed to sustain convection or sustained very weak convection (storm A) had much greater variability between ensemble storm outcomes.

- The successful suites contained more humid vertical profiles and greater overall environmental shear than less successful suites in the same region. All included supercells existed in environments with mid-tropospheric dry air. This was joined by a local minima in vertical wind shear in most of the successful suites and a local maxima in the unsuccessful suites.

- Of the successful suites, supercells M and N best matched the evolutionary trends of their corresponding observed storms are seen by low- and mid-level AzShear.

- The corresponding observed supercells of the unsuccessful ensemble suites were all advantageously influenced by a mesoscale feature in their environments. For supercell L, an outflow boundary from nearby supercells revived the weakening storm in an environment that could not support simulated deep convection. Supercell X formed in a confluence band and took several hours to strengthen in an ambient environment primed by nearby convection. This evolution is much more gradual than our tendency nudging mechanism, and might be the only type of evolution supported in its environment. Supercell JU seems to be a combination of storms X and L, as it formed in another confluence band and was also potentially aided by outflow from a supercell to its northeast.

As these eight supercells were all part of the same event and existed in extremely favorable environments, it is likely that the more successful, more realistic supercell suites represented observed supercells that were more predicated by their background environments. In particular, the observed morphology of supercells M and N appear to be more influenced by their ambient conditions than localized factors such as cell mergers and topography. Horizontal heterogeneity of the residual thermal boundary itself had little direct impact; however, the resulting enhanced shear in the background environment seems to be the determining factor in these two storms' evolutions. As this stronger shear is present in the broader boundary zone, it is plausible that other supercells in the region evolved in response to the larger environment and were less reliant on mesoscale features. Regarding the predictability of the 27 April 2011 Super Outbreak as a whole, the background environment alone does not fully account for the diversity in supercell behavior observed across the entire southeastern U.S. Storm evolutions in regions with comparatively less vertical wind shear relied on external, mesoscale influences to overcome the detrimental effects of dry air aloft.

There are many limitations to this study. The relatively coarse spatial resolution employed in our simulations was necessary to minimize computational expense, but also reduces our ability to study supercell dynamics in detail. While we can resolve necessary features, we lose potentially relevant detail in those features achieved by many other recent, higher-resolution studies. The range-dependence of AzShear is discussed, but no attempts to correct it are made and any impacts on our simulation-to-observations comparison are accepted. Lastly, as this is a case study of a rare, extreme event, the results are specific to the individual supercells and are not generalizable to other events or individual storms.

This thesis provided some insight on the role of the ambient environments on individual supercell evolutions, but a number of questions remain. The storm outcomes produced by a greater variety of CI characteristics in these environments should be studied before definitively concluding that the role of the background environments are as stated herein. This would include further adjusting the magnitudes and durations of the heating tendency, as well as its radius and elevation, potentially to emulate a region of weaker, elongated, long-lasting forcing like that of a confluence band. Higher resolution simulations can also be generated to include tornado-like vortices in the analysis, allowing for the inclusion of the observed dormant periods experienced by some supercells.

Reference List

Anderson-Frey, A. K., Y. P. Richardson, A. R. Dean, R. L. Thompson, and B. T. Smith, 2019: Characteristics of tornado events and warnings in the southeastern united states. *Wea. Forecasting*, **34 (4)**, 1017–1034.

Archambault, H. M., L. F. Bosart, D. Keyser, and J. M. Cordeira, 2013: A climatological analysis of the extratropical flow response to recurving western north pacific tropical cyclones. *Mon. Wea. Rev.*, **141 (7)**, 2325–2346.

Ashley, W. S., 2007: Spatial and temporal analysis of tornado fatalities in the united states: 1880–2005. *Wea. Forecasting*, **22 (6)**, 1214–1228.

Ashley, W. S., A. J. Krmenec, and R. Schwantes, 2008: Vulnerability due to nocturnal tornadoes. *Wea. Forecasting*, **23 (5)**, 795–807.

Banacos, P. C., and H. B. Bluestein, 2004: Hodograph variability within analytically modeled, synoptic-scale, baroclinic systems. *Mon. Wea. Rev.*, **132 (6)**, 1448–1461.

Brooks, H. E., C. A. Doswell III, and M. P. Kay, 2003: Climatological estimates of local daily tornado probability for the united states. *Wea. Forecasting*, **18 (4)**, 626–640.

Bryan, G. H., and J. M. Fritsch, 2002: A benchmark simulation for moist nonhydrostatic numerical models. *Mon. Wea. Rev.*, **130 (12)**, 2917–2928.

Bunkers, M. J., J. S. Johnson, L. J. Czepyha, J. M. Grzywacz, B. A. Klimowski, and M. R. Hjelmfelt, 2006: An observational examination of long-lived supercells. part ii: Environmental conditions and forecasting. *Wea. Forecasting*, **21 (5)**, 689–714.

Bunkers, M. J., J. R. Wetenkamp Jr, J. J. Schild, and A. Fischer, 2010: Observations of the relationship between 700-mb temperatures and severe weather reports across the contiguous united states. *Wea. Forecasting*, **25 (2)**, 799–814.

Chasteen, M. B., and S. E. Koch, 2022a: Multiscale aspects of the 26–27 april 2011 tornado outbreak. part i: Outbreak chronology and environmental evolution. *Mon. Wea. Rev.*, **150 (2)**, 309–335.

Chasteen, M. B., and S. E. Koch, 2022b: Multiscale aspects of the 26–27 april 2011 tornado outbreak. part ii: Environmental modifications and upscale feedbacks arising from latent processes. *Mon. Wea. Rev.*, **150 (2)**, 337–368.

Cintineo, R. M., and D. J. Stensrud, 2013: On the predictability of supercell thunderstorm evolution. *J. Atmos. Sci.*, **70 (7)**, 1993–2011.

Coffer, B. E., and M. D. Parker, 2015: Impacts of increasing low-level shear on supercells during the early evening transition. *Mon. Wea. Rev.*, **143 (5)**, 1945–1969.

Coffer, B. E., and M. D. Parker, 2017: Simulated supercells in nontornadic and tornadic vortex2 environments. *Mon. Wea. Rev.*, **145 (1)**, 149–180.

Cohen, A. E., 2010: Indices of violent tornado environments. *Electron. J. Oper. Meteor*, **11 (6)**.

Coleman, T. A., and P. G. Dixon, 2014: An objective analysis of tornado risk in the united states. *Wea. Forecasting*, **29 (2)**, 366–376.

Coniglio, M. C., and R. E. Jewell, 2022: Spc mesoscale analysis compared to field-project soundings: Implications for supercell environment studies. *Mon. Wea. Rev.*, **150 (3)**, 567–588.

Corfidi, S. F., S. J. Weiss, J. S. Kain, S. J. Corfidi, R. M. Rabin, and J. J. Levit, 2010: Revisiting the 3–4 april 1974 super outbreak of tornadoes. *Wea. Forecasting*, **25 (2)**, 465–510.

Davenport, C. E., 2021: Environmental evolution of long-lived supercell thunderstorms in the great plains. *Wea. Forecasting*, **36 (6)**, 2187–2209.

Davenport, C. E., and M. D. Parker, 2015: Impact of environmental heterogeneity on the dynamics of a dissipating supercell thunderstorm. *Mon. Wea. Rev.*, **143 (10)**, 4244–4277.

Davenport, C. E., C. L. Ziegler, and M. I. Biggerstaff, 2019: Creating a more realistic idealized supercell thunderstorm evolution via incorporation of base-state environmental variability. *Mon. Wea. Rev.*, **147 (11)**, 4177–4198.

Davies-Jones, R., 1984: Streamwise vorticity: The origin of updraft rotation in supercell storms. *J. Atmos. Sci.*, **41 (20)**, 2991–3006.

Davies-Jones, R., 2015: A review of supercell and tornado dynamics. *Atmospheric Research*, **158**, 274–291.

Dean, A. R., and R. S. Schneider, 2012: An examination of tornado environments, events, and impacts from 2003-2012. *Preprints, 26th Conf. on Severe Local Storms*, Amer. Meteor. Soc, Nashville, TN.

Duell, R. S., and M. S. Van Den Broeke, 2016: Climatology, synoptic conditions, and misanalyses of mississippi river valley drylines. *Mon. Wea. Rev.*, **144 (3)**, 927–943.

Fischer, J., and J. M. Dahl, 2020: The relative importance of updraft and cold pool characteristics in supercell tornadogenesis using highly idealized simulations. *J. Atmos. Sci.*, **77 (12)**, 4089–4107.

Fischer, J., and J. M. Dahl, 2022: Transition of near-ground vorticity dynamics during tornadogenesis. *J. Atmos. Sci.*, **79 (2)**, 467–483.

Fischer, J., M. D. Flournoy, and A. W. Lyza, 2023: Comments on "a climatology of cell mergers with supercells and their association with mesocyclone evolution" and "the influence of cell mergers on supercell characteristics and tornado evolution on 27–28 april 2011". *Mon. Wea. Rev.*, **151 (9)**, 2541–2545.

Flora, M. L., C. K. Potvin, and L. J. Wicker, 2018: Practical predictability of supercells: Exploring ensemble forecast sensitivity to initial condition spread. *Mon. Wea. Rev.*, **146 (8)**, 2361–2379.

Flora, M. L., P. S. Skinner, C. K. Potvin, A. E. Reinhart, T. A. Jones, N. Yussouf, and K. H. Knopfmeier, 2019: Object-based verification of short-term, storm-scale probabilistic mesocyclone guidance from an experimental warn-on-forecast system. *Wea. Forecasting*, **34 (6)**, 1721–1739.

Flournoy, M. D., and E. N. Rasmussen, 2023: The influence of convection initiation strength on subsequent simulated supercell evolution. *Mon. Wea. Rev.*, **151 (9)**, 2179–2203.

French, A. J., and M. D. Parker, 2014: Numerical simulations of bow echo formation following a squall line–supercell merger. *Mon. Wea. Rev.*, **142 (12)**, 4791–4822.

Gaffin, D. M., 2012: The influence of terrain during the 27 april 2011 super tornado outbreak and 5 july 2012 derecho around the great smoky mountains national park. *Preprints, 26th Conf. on Severe Local Storms*.

Gilmore, M. S., and L. J. Wicker, 1998: The influence of midtropospheric dryness on supercell morphology and evolution. *Mon. Wea. Rev.*, **126 (4)**, 943–958.

Grams, C. M., and H. M. Archambault, 2016: The key role of diabatic outflow in amplifying the midlatitude flow: A representative case study of weather systems surrounding western north pacific extratropical transition. *Mon. Wea. Rev.*, **144 (10)**, 3847–3869.

Grams, J. S., R. L. Thompson, D. V. Snively, J. A. Prentice, G. M. Hodges, and L. J. Reames, 2012: A climatology and comparison of parameters for significant tornado events in the united states. *Wea. Forecasting*, **27 (1)**, 106–123.

Guyer, J. L., and A. R. Dean, 2010: Tornadoes within weak cape environments across the continental united states. *25th Conf. on Severel Local Storms*, 1.5.

Hamill, T. M., R. S. Schneider, H. E. Brooks, G. S. Forbes, H. B. Bluestein, M. Steinberg, D. Meléndez, and R. M. Dole, 2005: The may 2003 extended tornado outbreak. *Bull. Amer. Meteo. Soc.*, **86 (4)**, 531–542.

Hastings, R., and Y. Richardson, 2016: Long-term morphological changes in simulated supercells following mergers with nascent supercells in directionally varying shear. *Mon. Wea. Rev.*, **144 (2)**, 471–499.

Hastings, R. M., Y. P. Richardson, P. M. Markowski, J. Wurman, and C. Weiss, 2014: Simulation of near-surface mesocyclogenesis during mergers between mature and nascent supercells. *Preprints, 27th Conf. on Severe Local Storms*, Amer. Meteor. Soc.

Hayes, J., 2011: Service assessment: The historic tornadoes of april 2011. US National Weather Service.

Hoch, J., and P. Markowski, 2005: A climatology of springtime dryline position in the us great plains region. *J. Climate*, **18 (12)**, 2132–2137.

James, R. P., and P. M. Markowski, 2010: A numerical investigation of the effects of dry air aloft on deep convection. *Mon. Wea. Rev.*, **138 (1)**, 140–161.

Kain, J. S., and Coauthors, 2008: Some practical considerations regarding horizontal resolution in the first generation of operational convection-allowing nwp. *Wea. Forecasting*, **23 (5)**, 931–952.

Katona, B., and P. Markowski, 2021: Assessing the influence of complex terrain on severe convective environments in northeastern alabama. *Wea. Forecasting*, **36 (3)**, 1003–1029.

Klees, A. M., Y. P. Richardson, P. M. Markowski, C. Weiss, J. M. Wurman, and K. K. Kosiba, 2016: Comparison of the tornadic and nontornadic supercells intercepted by vortex2 on 10 june 2010. *Mon. Wea. Rev.*, **144 (9)**, 3201–3231.

Knupp, K. R., and Coauthors, 2014: Meteorological overview of the devastating 27 april 2011 tornado outbreak. *Bull. Amer. Meteo. Soc.*, **95 (7)**, 1041–1062.

Krocak, M. J., and H. E. Brooks, 2018: Climatological estimates of hourly tornado probability for the united states. *Wea. Forecasting*, **33 (1)**, 59–69.

Lawson, J. R., 2019: Predictability of idealized thunderstorms in buoyancy–shear space. *J. Atmos. Sci.*, **76 (9)**, 2653–2672.

Letkewicz, C. E., A. J. French, and M. D. Parker, 2013: Base-state substitution: An idealized modeling technique for approximating environmental variability. *Mon. Wea. Rev.*, **141 (9)**, 3062–3086.

Lin, Y.-L., 2008: *Mesoscale dynamics*, Vol. 10. Cambridge University Press.

Lyza, A. W., and M. D. Flournoy, 2023: The influence of cell mergers on supercell characteristics and tornado evolution on 27–28 april 2011. *Mon. Wea. Rev.*, **151 (6)**, 1551–1569.

Lyza, A. W., M. D. Flournoy, and E. N. Rasmussen, 2022: Observed characteristics of the tornadic supercells of 27–28 april 2011 in the southeast united states. *Mon. Wea. Rev.*, **150 (11)**, 2883–2910.

Lyza, A. W., and K. R. Knupp, 2018: A background investigation of tornado activity across the southern cumberland plateau terrain system of northeastern alabama. *Mon. Wea. Rev.*, **146 (12)**, 4261–4278.

Lyza, A. W., T. A. Murphy, B. T. Goudeau, P. T. Pangle, K. R. Knupp, and R. A. Wade, 2020: Observed near-storm environment variations across the southern cumberland plateau system in northeastern alabama. *Mon. Wea. Rev.*, **148 (4)**, 1465–1482.

Maddox, R. A., M. S. Gilmore, C. A. Doswell III, R. H. Johns, C. A. Crisp, D. W. Burgess, J. A. Hart, and S. F. Piltz, 2013: Meteorological analyses of the tri-state tornado event of march 1925. *Electron. J. Severe Storms Meteor.*, **8 (1)**, 1–27.

Maddox, R. A., L. R. Hoxit, and C. F. Chappell, 1980: A study of tornadic thunderstorm interactions with thermal boundaries. *Mon. Wea. Rev.*, **108 (3)**, 322–336.

Mahalik, M. C., B. R. Smith, K. L. Elmore, D. M. Kingfield, K. L. Ortega, and T. M. Smith, 2019: Estimates of gradients in radar moments using a linear least squares derivative technique. *Wea. Forecasting*, **34 (2)**, 415–434.

Markowski, P. M., 2016: An idealized numerical simulation investigation of the effects of surface drag on the development of near-surface vertical vorticity in supercell thunderstorms. *J. Atmos. Sci.*, **73 (11)**, 4349–4385.

Markowski, P. M., 2020: What is the intrinsic predictability of tornadic supercell thunderstorms? *Mon. Wea. Rev.*, **148 (8)**, 3157–3180.

Markowski, P. M., and N. Dotzek, 2011: A numerical study of the effects of orography on supercells. *Atmos. Res.*, **100 (4)**, 457–478.

Markowski, P. M., E. N. Rasmussen, and J. M. Straka, 1998: The occurrence of tornadoes in supercells interacting with boundaries during vortex-95. *Wea. Forecasting*, **13 (3)**, 852–859.

Markowski, P. M., and Y. P. Richardson, 2009: Tornadogenesis: Our current understanding, forecasting considerations, and questions to guide future research. *Atmos. Res.*, **93 (1-3)**, 3–10.

Melhauser, C., and F. Zhang, 2012: Practical and intrinsic predictability of severe and convective weather at the mesoscales. *J. Atmos. Sci.*, **69 (11)**, 3350–3371.

Newman, J. F., V. Lakshmanan, P. L. Heinselman, M. B. Richman, and T. M. Smith, 2013: Range-correcting azimuthal shear in doppler radar data. *Wea. Forecasting*, **28 (1)**, 194–211.

NOAA, 2011: Service assessment: The historic tornadoes of april 2011. *National Weather Service*, 1–76.

Noda, A. T., and H. Niino, 2010: A numerical investigation of a supercell tornado: Genesis and vorticity budget. *J. of the Meteor. Soc. of Japan. Ser. II*, **88 (2)**, 135–159.

Nowotarski, C. J., and P. M. Markowski, 2016: Modifications to the near-storm environment induced by simulated supercell thunderstorms. *Mon. Wea. Rev.*, **144 (1)**, 273–293.

Parker, M. D., 2012: Impacts of lapse rates on low-level rotation in idealized storms. *J. Atmos. Sci.*, **69 (2)**, 538–559.

Parker, M. D., 2014: Composite vortex2 supercell environments from near-storm soundings. *Mon. Wea. Rev.*, **142 (2)**, 508–529.

Peters, J. M., C. J. Nowotarski, and G. L. Mullendore, 2020: Are supercells resistant to entrainment because of their rotation? *J. Atmos. Sci.*, **77 (4)**, 1475–1495.

Pfahl, S., C. Schwierz, M. Croci-Maspoli, C. M. Grams, and H. Wernli, 2015: Importance of latent heat release in ascending air streams for atmospheric blocking. *Nat. Geosci.*, **8 (8)**, 610–614.

Potvin, C. K., K. L. Elmore, and S. J. Weiss, 2010: Assessing the impacts of proximity sounding criteria on the climatology of significant tornado environments. *Wea. Forecasting*, **25 (3)**, 921–930.

Rasmussen, E. N., S. Richardson, J. M. Straka, P. M. Markowski, and D. O. Blanchard, 2000: The association of significant tornadoes with a baroclinic boundary on 2 june 1995. *Mon. Wea. Rev.*, **128 (1)**, 174–191.

Riehl, H., N. LaSeur, and Coauthors, 1952: Forecasting in middle latitudes. *Monographs, Amer. Meteor. Soc.*, **1**.

Roberts, B., M. Xue, A. D. Schenkman, and D. T. Dawson, 2016: The role of surface drag in tornadogenesis within an idealized supercell simulation. *J. Atmos. Sci.*, **73 (9)**, 3371–3395.

Rogers, J., 2012: Significant tornado events associated with cell mergers. *Preprints, 26th Conf. on Severe Local Storms*, Amer. Meteor. Soc, Nashville, TN.

Rogers, J. W., and C. Weiss, 2008: The association of cell mergers with tornado occurrence. *Preprints, 24th Conf. on Severe Local Storms*, Amer. Meteor. Soc.

Sanders, F., 1988: Life history of mobile troughs in the upper westerlies. *Mon. Wea. Rev.*, **116 (12)**, 2629–2648.

Schneider, R. S., A. Dean, S. Weiss, and P. D. Bothwell, 2006: Analysis of estimated environments for 2004 and 2005 severe convective storm reports. *Preprints, 23rd Conf. on Severe Local Storms*, St. Louis, MO, Vol. 3.

Schneider, R. S., and A. R. Dean, 2008: A comprehensive 5-year severe storm environment climatology for the continental united states. *Preprints, 24th Conf. on Severe Local Storms*, Amer. Meteor. Soc., Vol. 16.

Sherburn, K. D., and M. D. Parker, 2014: Climatology and ingredients of significant severe convection in high-shear, low-cape environments. *Wea. Forecasting*, **29 (4)**, 854–877.

Simmons, K., D. Sutter, and R. Pielke, 2012: Blown away: monetary and human impacts of the 2011 us tornadoes. *The Geneva Reports*, **107 (5)**, 107–120.

Smith, T. M., and K. L. Elmore, 2004: The use of radial velocity derivatives to diagnose rotation and divergence. *Preprints, 11th Conf. on Aviation, Range, and Aerospace*, Amer. Meteor. Soc, Hyannis, MA, Vol. 5.

Sobash, R. A., G. S. Romine, C. S. Schwartz, D. J. Gagne, and M. L. Weisman, 2016a: Explicit forecasts of low-level rotation from convection-allowing models for next-day tornado prediction. *Wea. Forecasting*, **31 (5)**, 1591–1614.

Sobash, R. A., C. S. Schwartz, G. S. Romine, K. R. Fossell, and M. L. Weisman, 2016b: Severe weather prediction using storm surrogates from an ensemble forecasting system. *Wea. Forecasting*, **31 (1)**, 255–271.

Thompson, R. L., R. Edwards, J. A. Hart, K. L. Elmore, and P. Markowski, 2003: Close proximity soundings within supercell environments obtained from the rapid update cycle. *Wea. Forecasting*, **18 (6)**, 1243–1261.

Thompson, R. L., B. T. Smith, J. S. Grams, A. R. Dean, and C. Broyles, 2012: Convective modes for significant severe thunderstorms in the contiguous united states. part ii: Supercell and qlcs tornado environments. *Wea. Forecasting*, **27 (5)**, 1136–1154.

Thorncroft, C., B. Hoskins, and M. McIntyre, 1993: Two paradigms of baroclinic-wave life-cycle behaviour. *Quart. J. Roy. Meteor. Soc.*, **119 (509)**, 17–55.

Trapp, R. J., 2014: On the significance of multiple consecutive days of tornado activity. *Mon. Wea. Rev.*, **142 (4)**, 1452–1459.

Trapp, R. J., S. A. Tessendorf, E. S. Godfrey, and H. E. Brooks, 2005: Tornadoes from squall lines and bow echoes. part i: Climatological distribution. *Wea. Forecasting*, **20 (1)**, 23–34.

Weisman, M. L., M. Gilmore, and L. Wicker, 1998: The impact of convective storms on their local environment: what is an appropriate ambient sounding? *Preprints, 19th Conf. on Severe Local Storms*, Amer. Meteor. Soc.

Werkema, A. D., 2022: Mutual influences of adjacent supercells in multistorm simulations. Ph.D. thesis, North Carolina State University, 114 pp.

Wernli, H., and H. C. Davies, 1997: A lagrangian-based analysis of extratropical cyclones. i: The method and some applications. *Quart. J. Roy. Meteor. Soc.*, **123 (538)**, 467–489.

Wicker, L. J., and R. B. Wilhelmson, 1995: Simulation and analysis of tornado development and decay within a three-dimensional supercell thunderstorm. *J. Atmos. Sci.*, **52 (15)**, 2675–2703.

Wipf, J. N., and A. French, 2015: Simulated effects of an isolated supercell on the evolution of a nearby squall line. Ph.D. thesis, South Dakota School of Mines and Technology, Rapid City.

Zhang, Y., F. Zhang, D. J. Stensrud, and Z. Meng, 2015: Practical predictability of the 20 may 2013 tornadic thunderstorm event in oklahoma: Sensitivity to synoptic timing and topographical influence. *Mon. Wea. Rev.*, **143 (8)**, 2973–2997.

1 Appendix A

1.1 Approximation of Tornado Potential in Successful Suites

Vertical vorticity stretching by the low-level updraft is a well-known mechanism for the intensification of a vortex patch, potentially leading to tornadogenesis (Wicker and Wilhelmson 1995; Noda and Niino 2010; Fischer and Dahl 2022, among many others). Although we cannot resolve tornado-like vortices (TLVs) due to our relatively coarse horizontal grid spacing (dx=dy=1000 m), we can get an idea of tornado potential in our successful simulation suites (M, N, A, W, R) by looking for persistent, strong low-level updrafts with sufficient low-level vertical vorticity, assuming the maxima in vertical velocity and vorticity are collocated in space. For our purposes, we will use an updraft threshold of 20 m s^{-1} in the lowest 1 km of our simulations, and will look for vertical vorticity exceeding 0.01 s^{-1}, 0.015 s^{-1}, and 0.02 s^{-1} at the lowest model level (10 m AGL).

When ignoring the artificial intensity peaks associated with our synthetic heating tendencies, only the suites of M, N, and R meet this updraft constraint for an extended period of time in their early analysis period, indicating the potential to stretch any surface vertical vorticity. Of these three suites, only the 75th percentile of supercell N's ensembles contain vertical vorticity greater than 0.02 s^{-1} at the lowest model level, which occurs nearly 4 h after CI. The 0.015 s^{-1} vertical vorticity threshold is more readily met by the stronger ensembles in the suites of M, N, and R, extending to the lowest model level around 70 min after CI for storm M, 200 min after CI for storm N, and 140 min after CI for storm R. Given the strength of the low-level updrafts at each of these times for each suite, it appears that the greatest tornado potential would also occur at these times. One important consideration is the resolution of our simulations also do not allow for any significant intensification of vertical vorticity via strengthening, so it's possible that the tornado potential could extend beyond these times if we could resolve more.

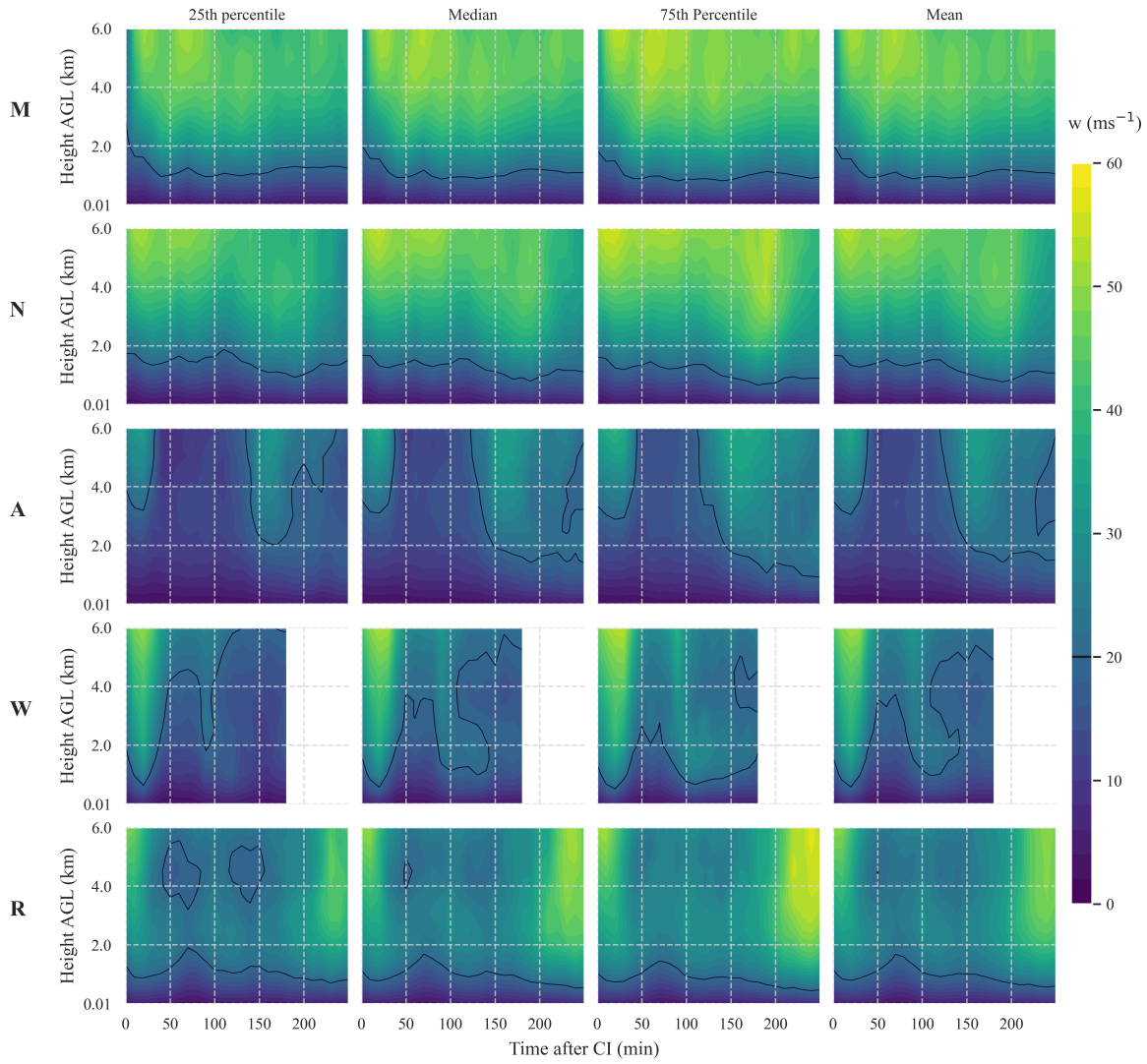

Figure A.1: As in Figure 3.4, but for updraft speed. The black contour denotes vertical velocities of 20 m s^{-1}.

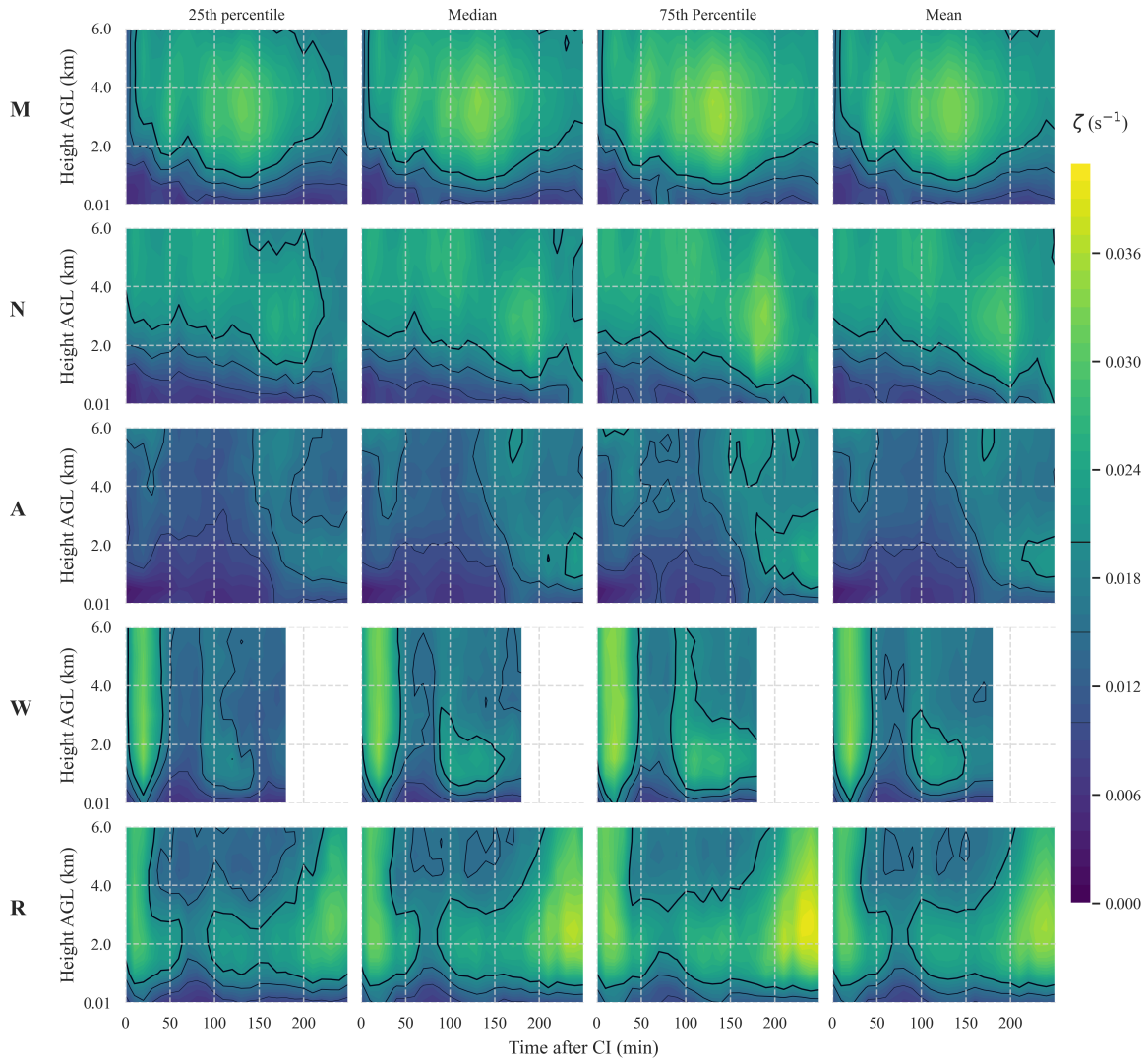

Figure A.2: As in Figure 3.4, but for vertical vorticity. The black contours denote values of 0.01 s^{-1}, 0.015 s^{-1}, and 0.02 s^{-1}, where thickness increases with magnitude.

2 Appendix B

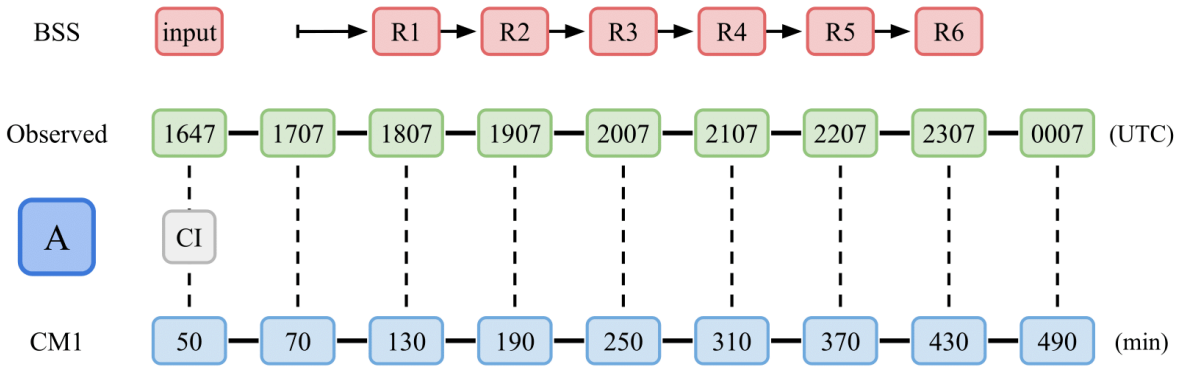

Figure A.3: Base-state substitution framework for supercell A.

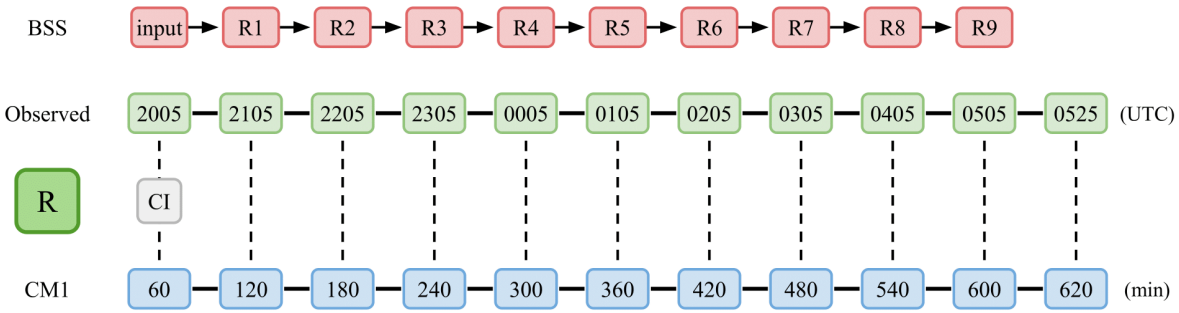

Figure A.4: Base-state substitution framework for supercell R.

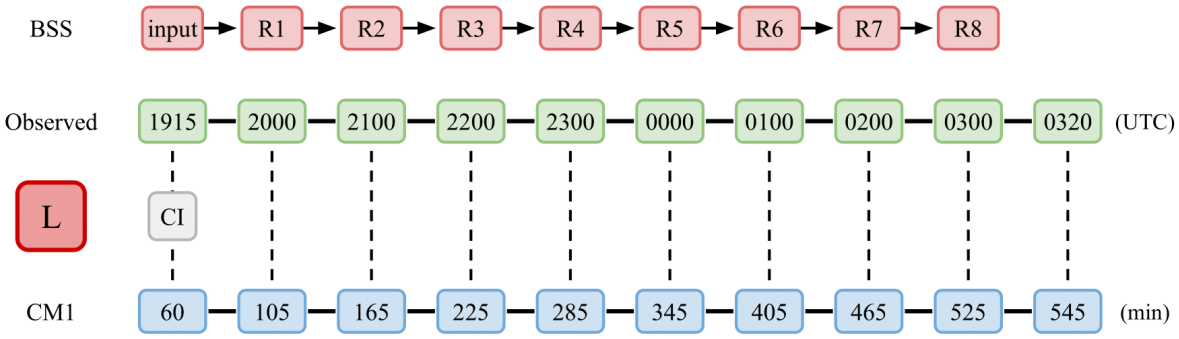

Figure A.5: Base-state substitution framework for supercell L.

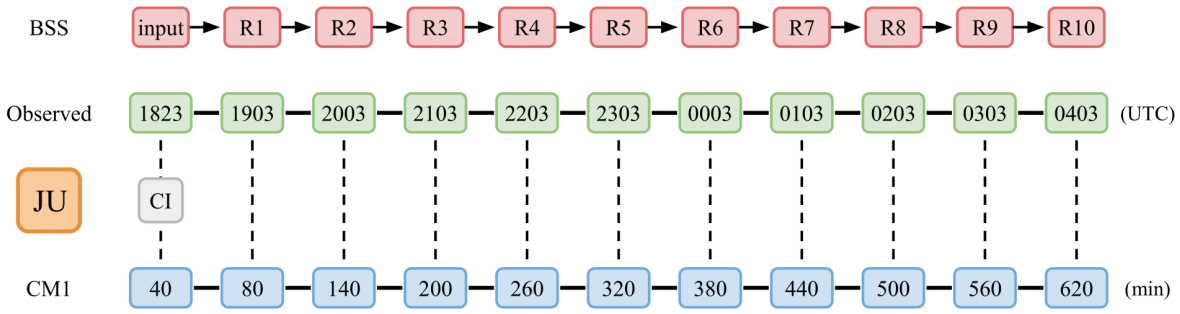

Figure A.6: Base-state substitution framework for supercell JU.

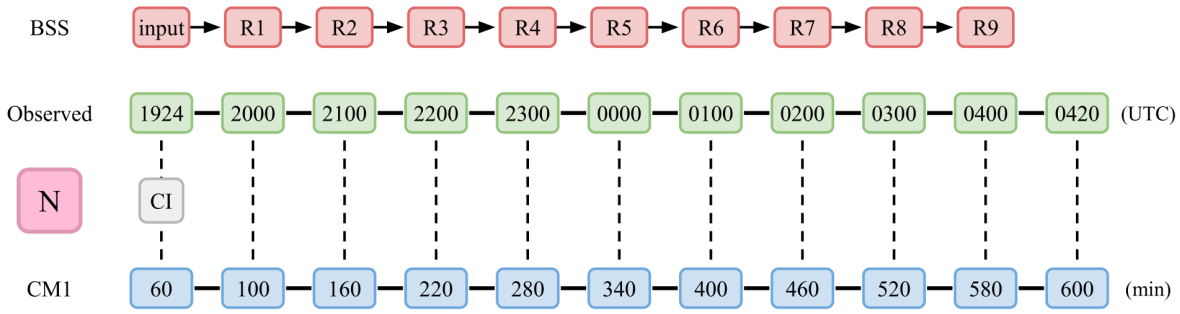

Figure A.7: Base-state substitution framework for supercell N.

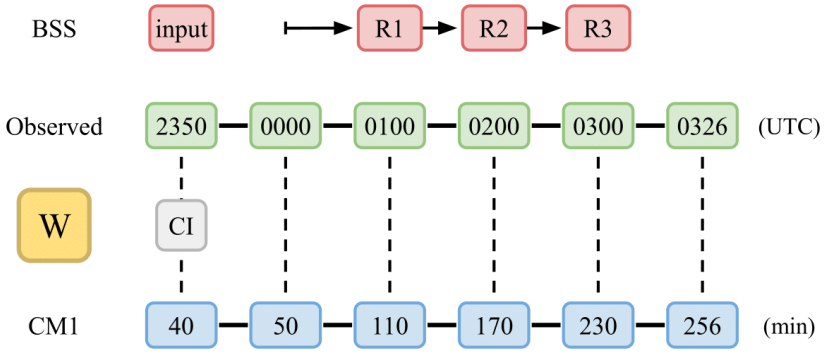

Figure A.8: Base-state substitution framework for supercell W.

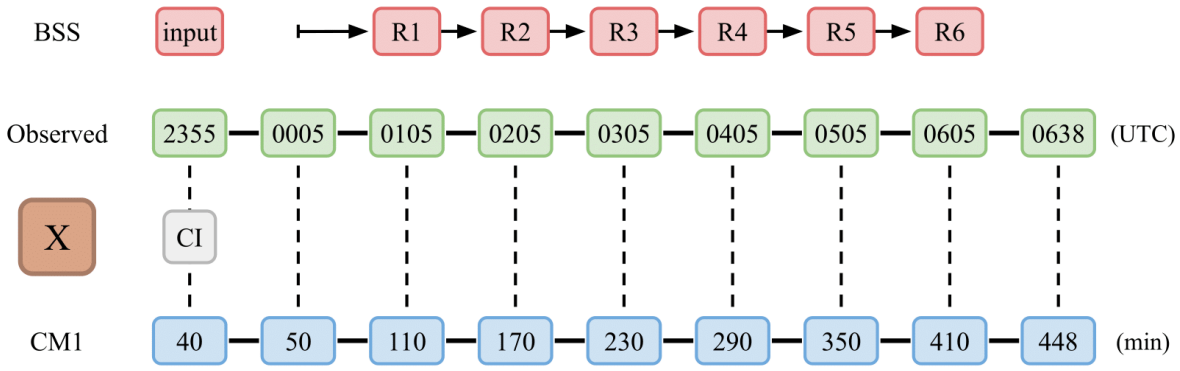

Figure A.9: Base-state substitution framework for supercell X.

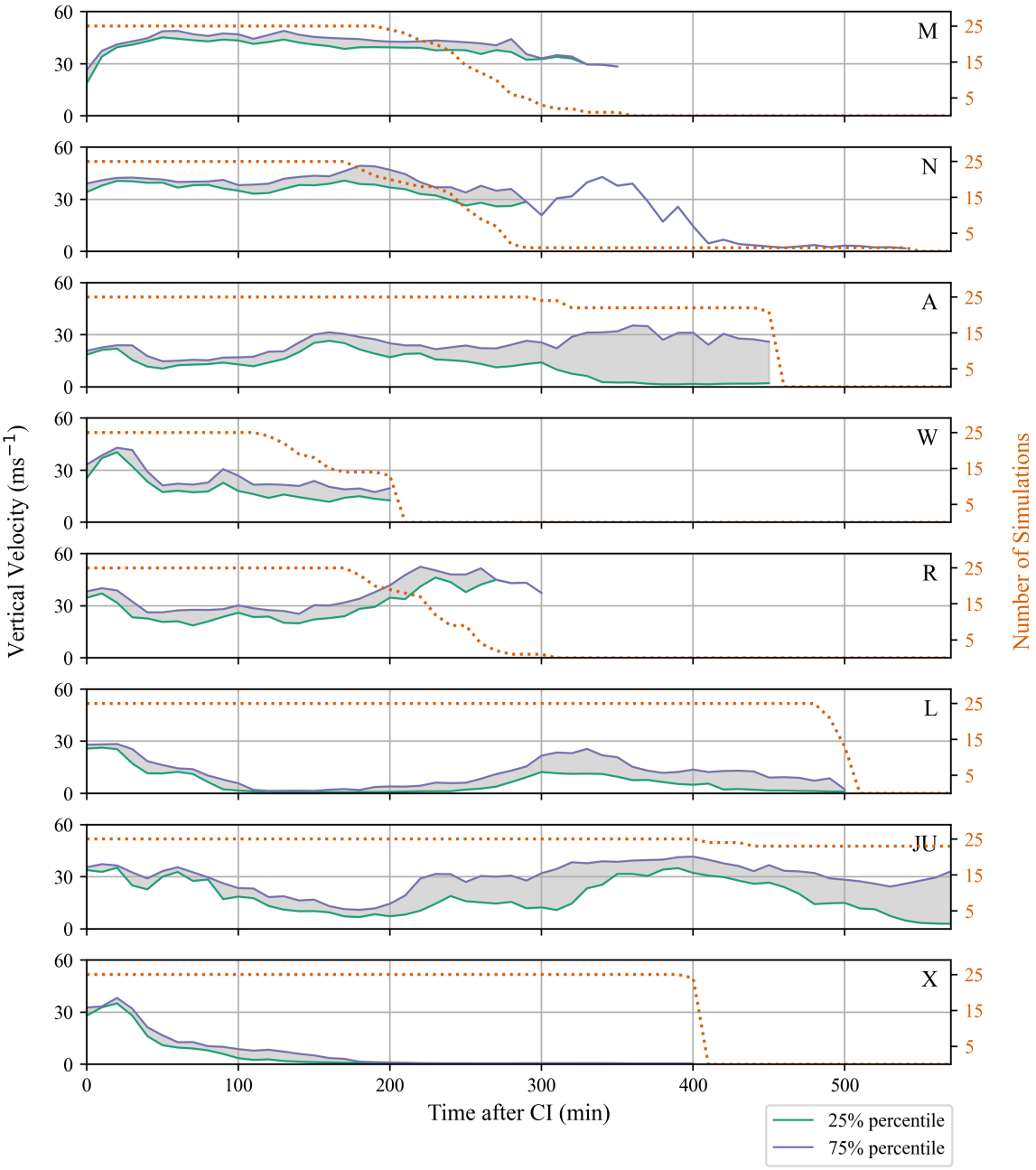

Figure A.10: Time series for 25th percentile (green line), 75th percentile (purple line), and IQR (gray shading) for maximum updraft speed at 3 km AGL after CI for each storm's ensemble suite. Each storm has a panel, and the panels are arranged by latitude of observed CI, so the northern-most initiating supercell is at the top and the southern-most at the bottom. The orange dashed line represents the number of ensemble members that have not experienced an unphysical reflectivity band merging with the main supercell.

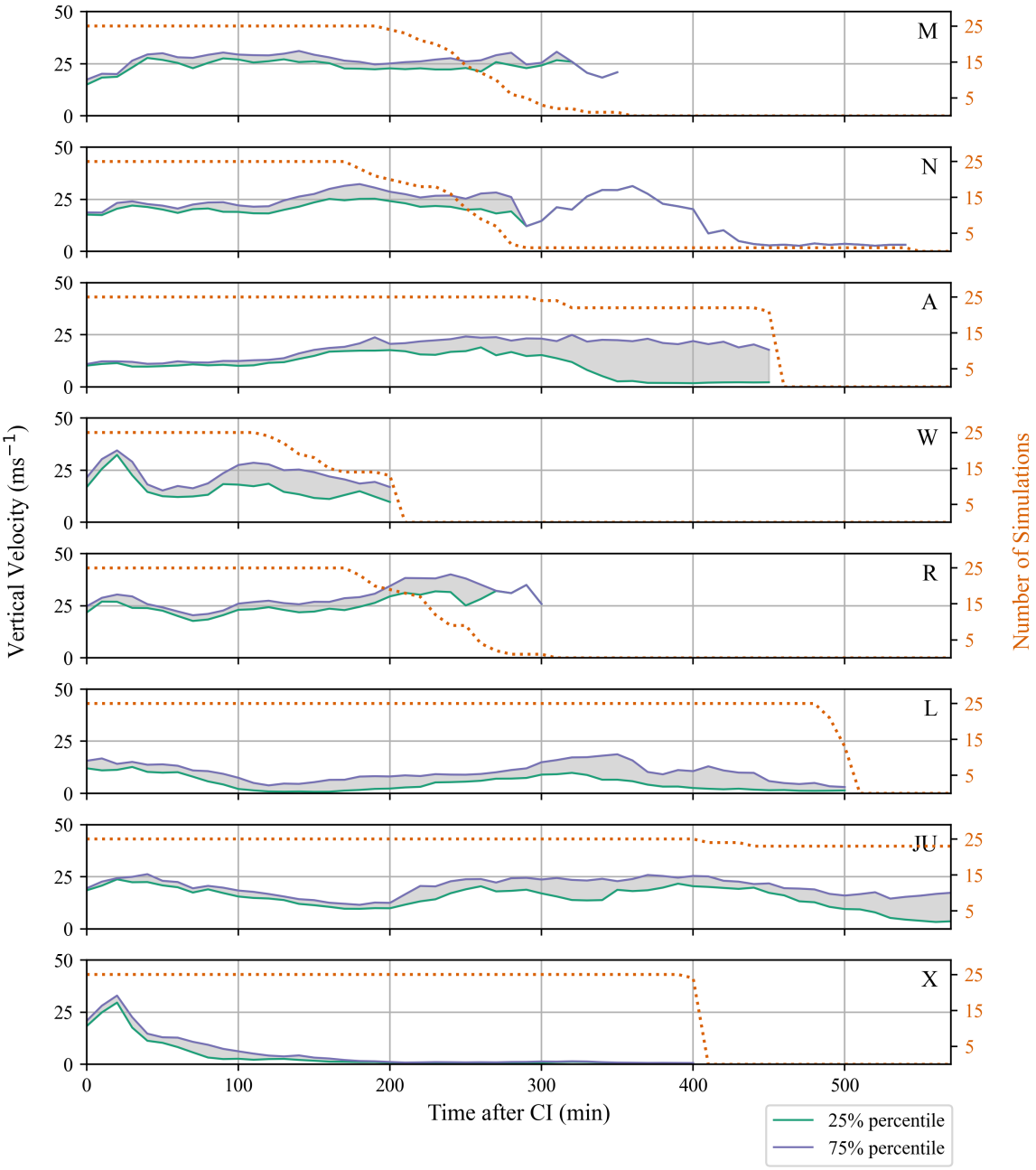

Figure A.11: As in Figure A.10, but for updraft speed at 1 km AGL.

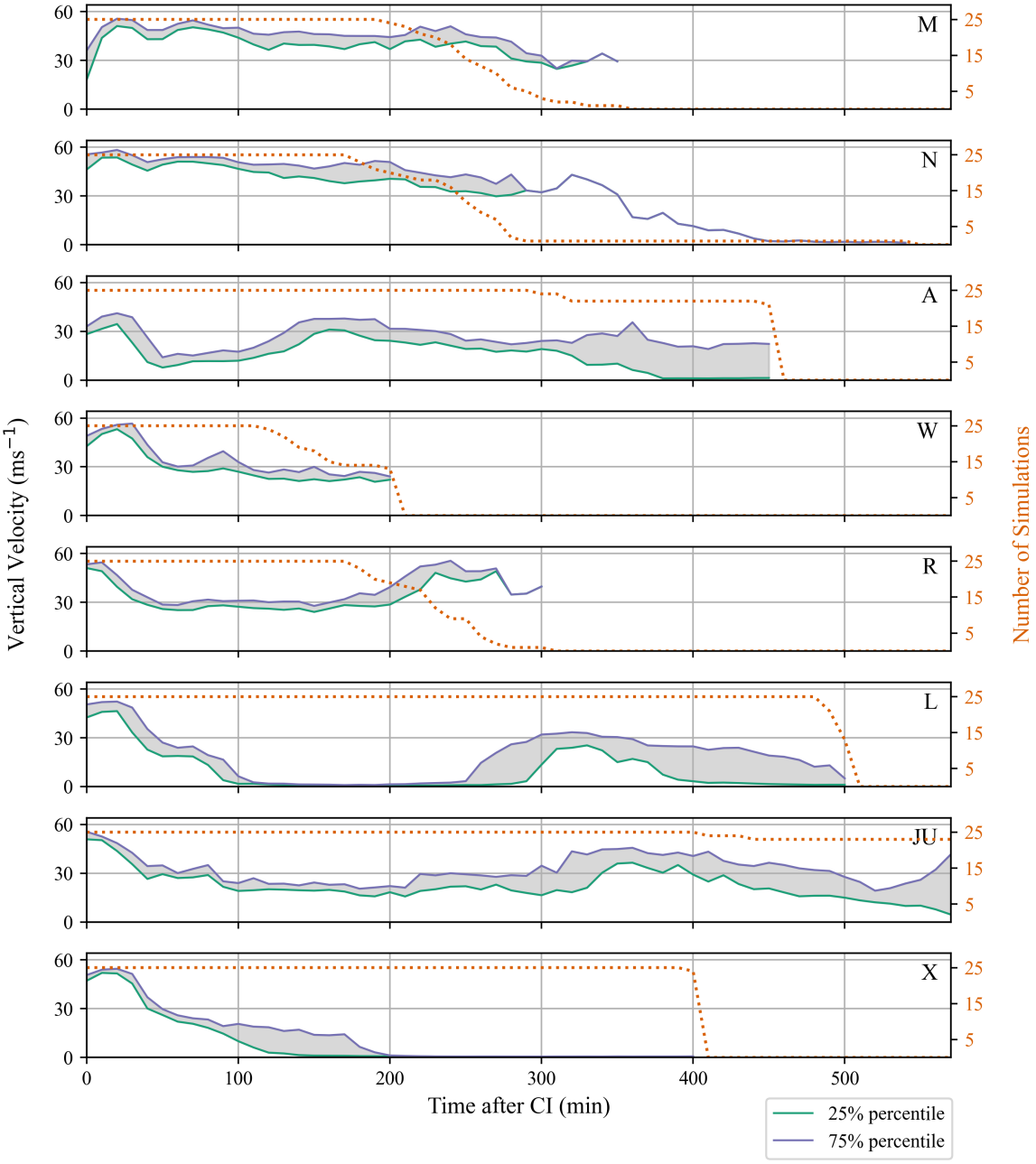

Figure A.12: As in Figure A.10, but for updraft speed at 6 km AGL.

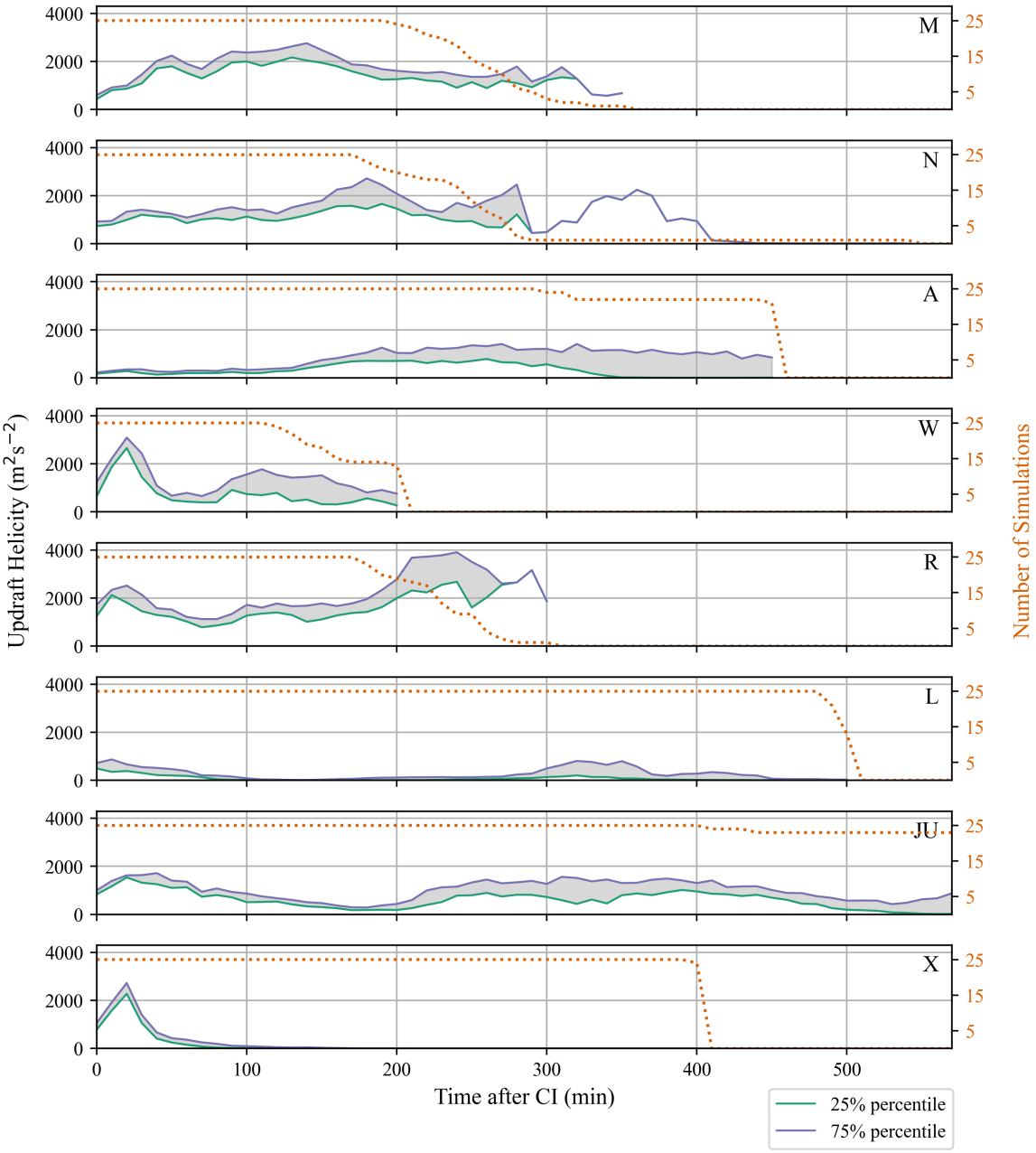

Figure A.13: As in Figure A.10, except for maximum 10-m to 3-km AGL updraft helicity.

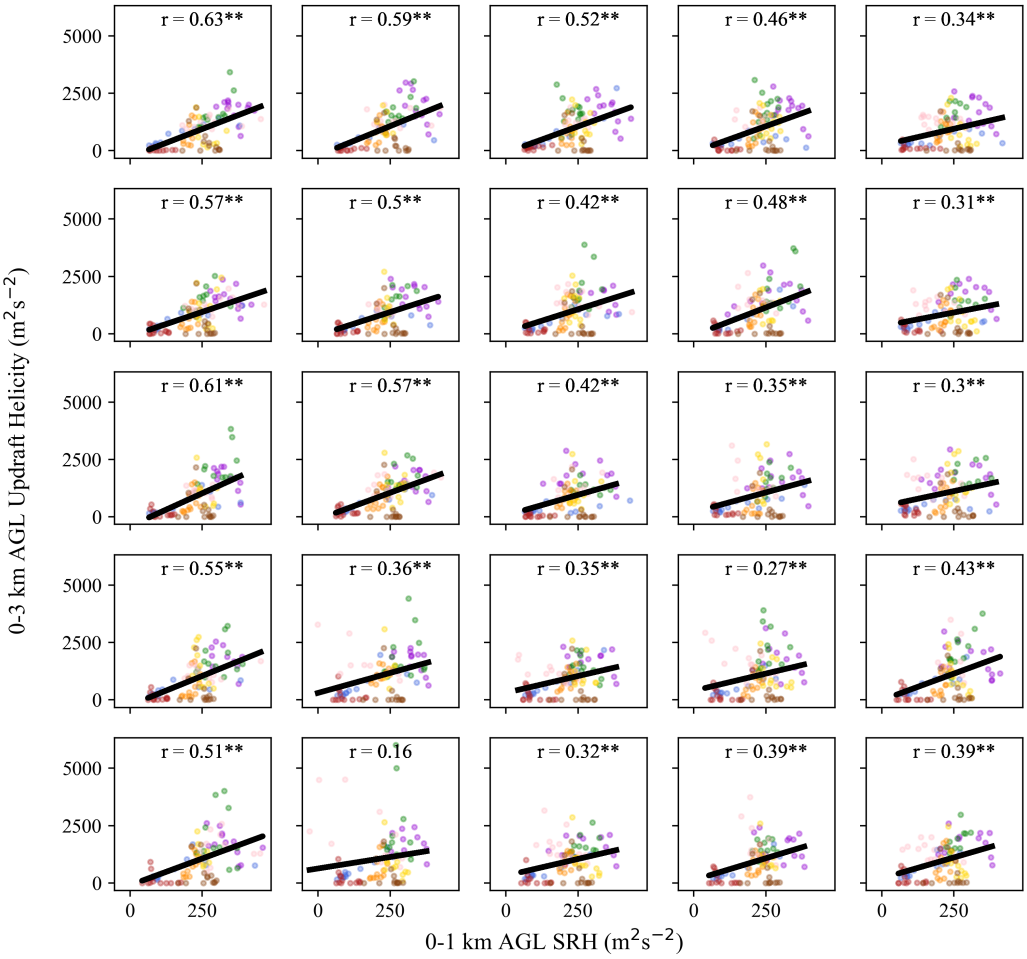

Figure A.14: As in Figure 3.10, except for 0–3-km AGL UH and 0–1-km AGL SRH.

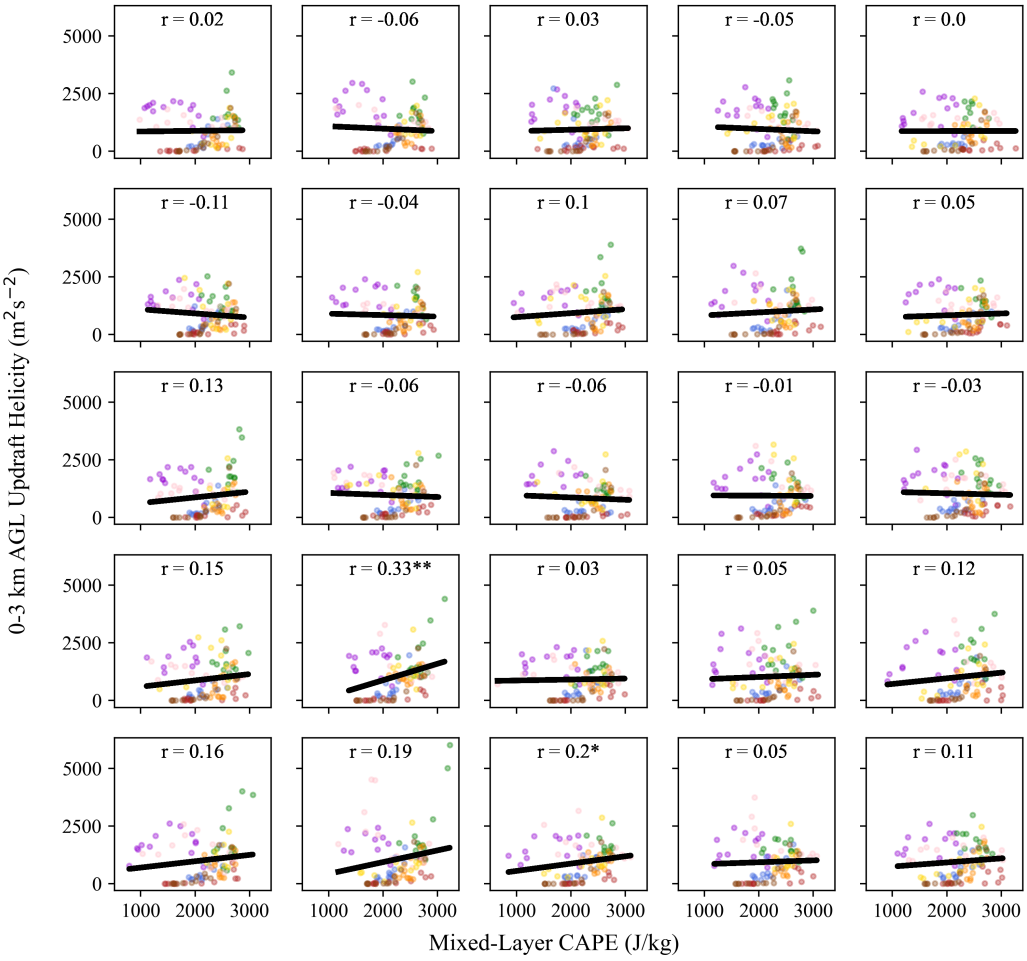

Figure A.15: As in Figure 3.10, except for 0–3-km AGL UH and MLCAPE.

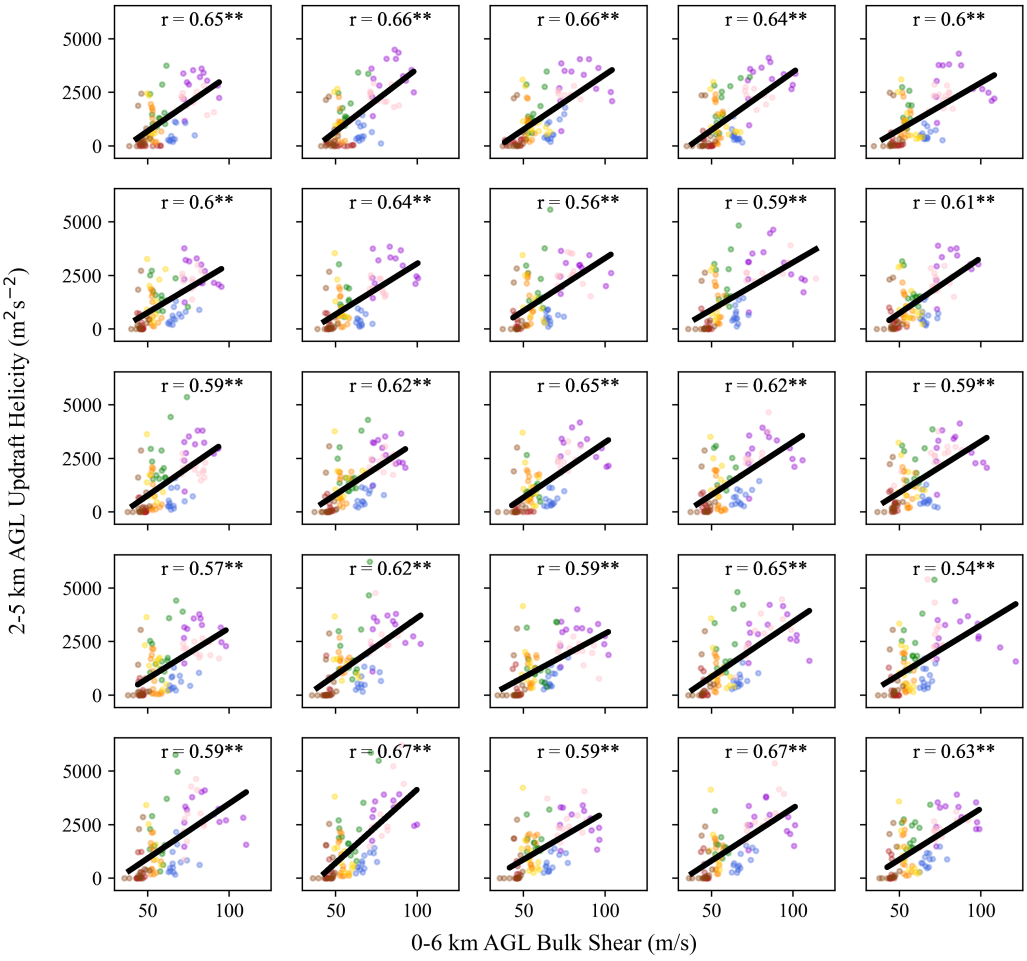

Figure A.16: As in Figure 3.10, except for 2–5-km AGL UH and 0–6-km bulk shear.

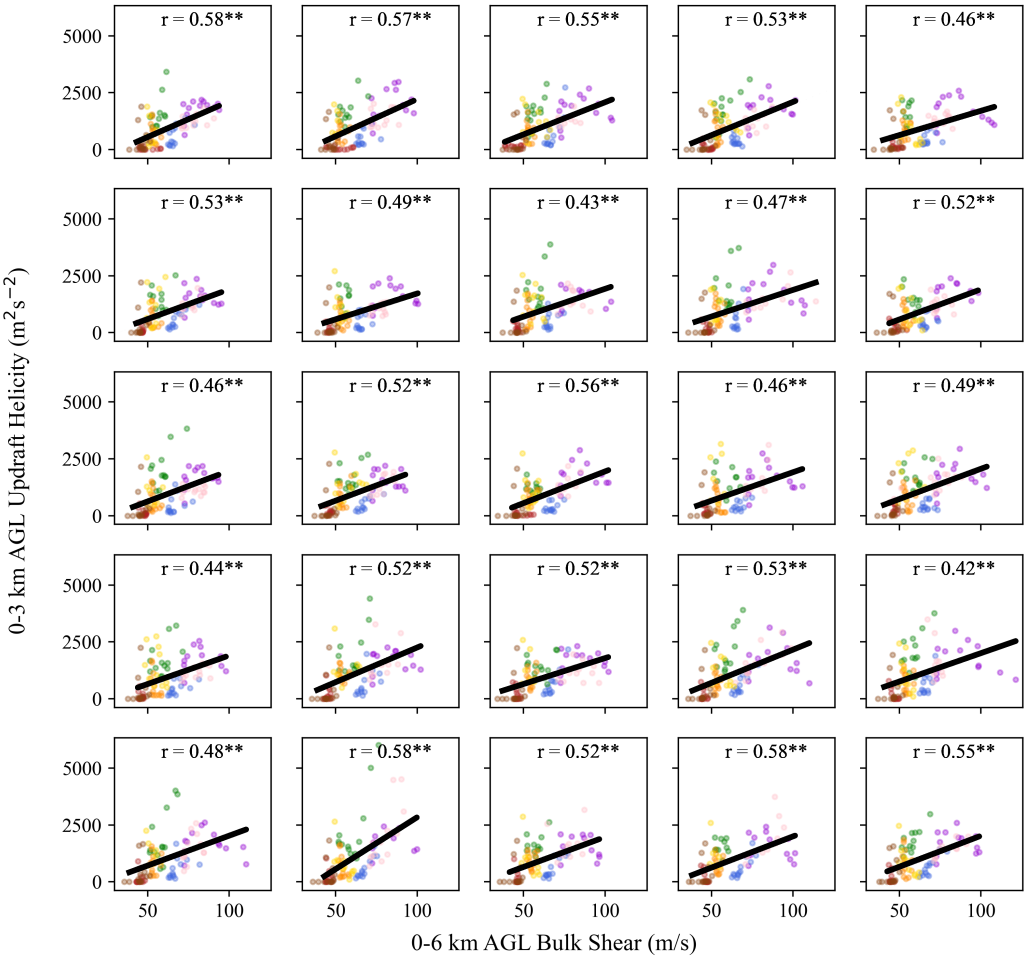

Figure A.17: As in Figure 3.10, except for 0–3-km AGL UH and 0–6-km bulk shear.

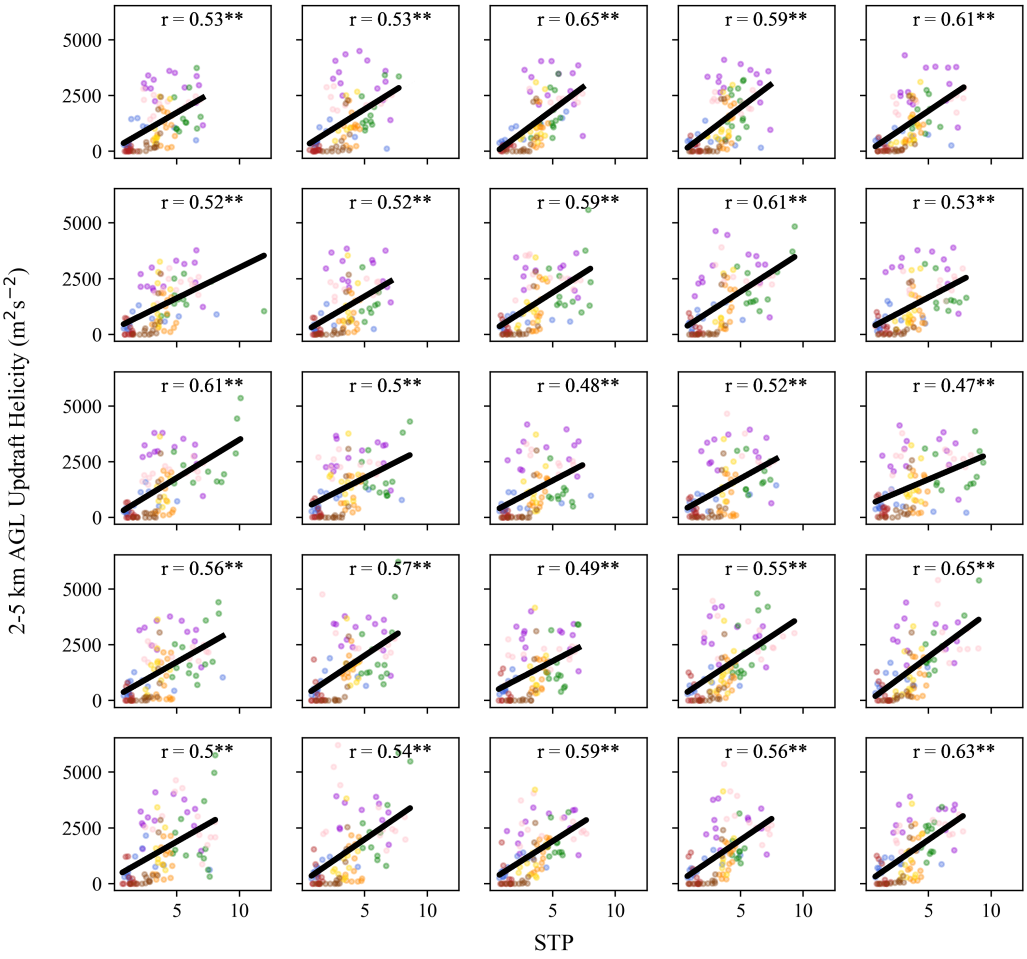

Figure A.18: As in Figure 3.10, except for 2–5-km AGL UH and STP.

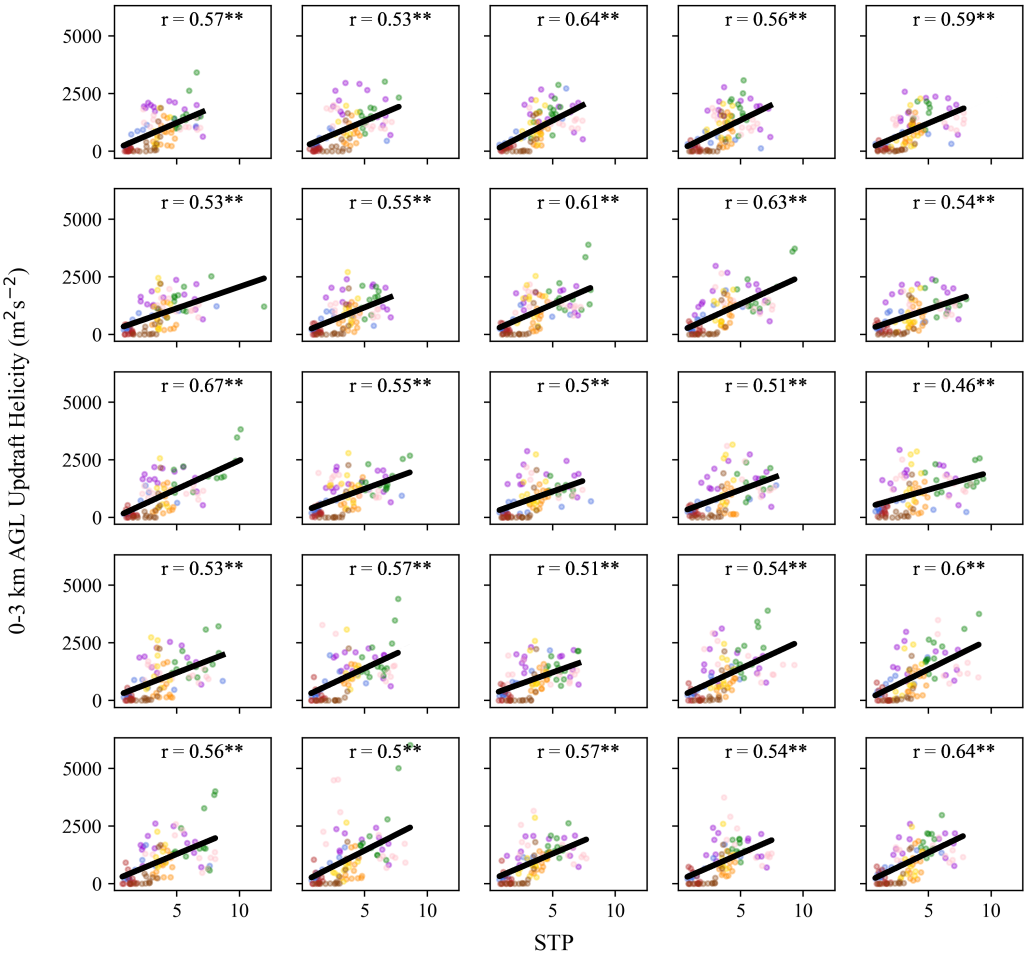

Figure A.19: As in Figure 3.10, except for 0–3-km AGL UH and STP.

replace	M	A	R	L	JU	N	W	X
1	60	140	60	45	40	40	70	70
2	120	200	120	105	100	100	130	130
3	180	260	180	165	160	160	190	190
4	240	320	240	225	220	200		250
5	300	380	300	285	280	280		310
6		440	360	345	340	340		370
7			420	405	400	400		
8			480	465	460	460		
9			540		520	520		
10					580			

Table A.1: Time (minutes) of the full implementation of replace files for each supercell, adjusted by the CI time of each suite's 13th ensemble member.